Institute for Materials Research
SCHOOL OF CHEMICAL AND PROCESS
ENGINEERING

UNIVERSITY OF LEEDS

Magnetoelectric Coupling in Single-Phase Multiferroics at Room Temperature via Scanning Probe Microscopy

Leonard Frederic Henrichs

Submitted in accordance with the requirements for the degree of
Doctor of Philosophy

The University of Leeds
Institute for Materials Research
School of Chemical and Process Engineering

September, 2015

The candidate confirms that the work submitted is his/her own, except where work which has formed part of jointly-authored publications has been included. The contribution of the candidate and the other authors to this work has been explicitly indicated below. The candidate confirms that appropriate credit has been given within the thesis where reference has been made to the work of others.

This research has been carried out by a team which has included Oscar Cespedes, James Bennett, Joachim Landers, Soma Salamon, Thomas Hansen, Tim Helbig, Christian Heuser, Philippa M. Shepley, Li Chen, Wolfgang Kleemann and Andrew J. Bell. My own contributions, fully and explicitly indicated in the thesis, have been: "sample preparation (synthesis, sintering, polishing), experiments on: magnetoelectric coupling especially those using piezoresponse force microscopy (PFM) (under magnetic field) and magnetic force microscopy (MFM), scanning electron microscopy with energy dispersive X-ray spectroscopy (SEM-EDX), X-ray diffraction, neutron diffraction, electrical and magnetic characterisation, most of the data analysis, interpretation of results." The other members of the group and their contributions have been as follows: "O.C. and S.S. performed many magnetometry experiments. J.B. prepared many samples and powders and carried out electrical and structural characterisation. J.L. and S.S. conducted Mössbauer spectroscopy experiments. Neutron diffraction experiments were carried out by T. Hansen. Additional MFM measurements were carried out by T. Helbig. C.H. carried out TOF-SIMS experiments. MOKE measurements were conducted by P.M.S. Deposition of thin-films was done by L.C. Research was supervised by A.J.B while W.K. and A.J.B were involved in interpretation of results."

Acknowledgements

First of all, I need to thank my supervisor Prof. Andrew Bell. His great knowledge and expertise were extremely important for the project's success. The fact that he did not dictate my research but rather guided me, enabled me to pursue the research that seemed the most interesting and promising to me and eventually led to the discovery of the MFC and the strong ME coupling. It also led to the discovery for my passion for research! He is a lovely person and I am very grateful to him, because I always felt supported by him and treated fairly. I never felt under pressure, which was not only important for me in terms of my research, but also for me personally, especially during the hard times that me and my family had to endure. It all turned out well. For all of this I want to tell you: "Thank you very, very much Andy!"

Furthermore, I want to express my deep gratitude to Prof. Wolfgang Kleemann, who has been an invaluable support and mentor to me. My work benefited greatly from his immense knowledge and commitment while I learned so much through our numerous discussions. Thank you ever so much Wolfgang!

A big thank you also goes to the Leeds group: Jim, Laura, Faye, Rob, Anton and Diane! You were lovely colleagues and made me enjoy my time in Leeds. I very much appreciate all your help (especially Jim's who helped me in the lab so many times!) Special thanks go to Oscar Cespedes, from Physics department, who ran so many magnetic measurements.

Prof. Doru Lupascu welcomed me to his group during my long secondment at University of Duisburg-Essen which I very much appreciate! I also want to thank Danka, Kevin, Shahab, Lacki, Vladimir, Morat, Herr Keck and everyone else from the group for being so welcoming and made me feel at home. My discussions with Vladimir were particularly interesting and useful. I appreciate the help of Prof. Heiko Wende and his group members Joachim and Soma for valuable measurements and fruitful discussions in matters of magnetism. Other contributions to the project as listed above are also very

Last but not least, I want to thank my family and friends for supporting us and for visiting us in England. My deepest gratitude is due to my mother, who has been such an important source of support through all my life! Many kisses and thank you Mama!

Finally, words cannot express the deep gratitude that I feel for my beloved wife Jule and my sweet little ones Jesper and Oscar! Jule: "Thank you for coming with me into this great adventure and for making all of this possible!"

Abstract

In ceramic samples of the material, $(BiFe_{1-x}Co_xO_3)_{0.4}$-$(Bi_{1/2}K_{1/2}TiO_3)_{0.6}$ (BFC-BKT), a new kind of nano-sized region, so called *multiferroic clusters* (MFC) were found at room-temperature. These exhibit the largest reported magnetoelectric (ME) coupling coefficient, $\alpha \approx 1.0$ x 10^{-5} s/m (corresponding to a Voltage coefficient dE/dH $\approx$ 1300 V/(cm Oe)) for a single phase multiferroic so far, to the best of the author's knowledge. Furthermore, they are ferroelectric and ferrimagnetic at the same time, which has not yet been observed directly in one material. Using a broad range of experimental techniques, formation of the MFC has been understood in terms of the non-ergodic relaxor properties and ferrimagnetism in inherent $Bi(Fe,Co)O_3$ rich regions. Furthermore, the presence of magnetic nanoregions (MNR) was confirmed and their formation and role in ME coupling are discussed.

Solid solutions of the system $(PbZr_{0.52}Ti_{0.48}O_3)_{1-x}$-$(PbFe_{2/3}W_{1/3}O_3)_x$ (PZT-PFW) were prepared which, however, did not show ME effects. Nevertheless, analogies to BFC-BKT concerning occurrence of characteristic magnetic phases were established.

Since piezoresponse force microscopy (PFM) played an important role in this study, the method was subject to detailed investigations concerning e.g. the signal stability. Among others, it was found that it is highly beneficial to use diamond coated tips in PFM.

In addition, a useful and easily applicable technique for distinguishable marking of micro-sized areas has been developed.

It is expected that especially the findings on BFC-BKT will have wider implications, as they enable an entirely new perspective for such relaxor-type ferrimagnetic multiferroics, which were barely considered in research so far. The relaxor properties are expected to play an important role in the strong ME coupling. Since the MFC are well-separated and offer large ME coupling, they are suitable to serve as bits in an electrically controlled magnetic nanodot storage device (MERAM). Various possibilities, the for realization of such a device are discussed.

Table of Contents

List of Tables

List of Figures

Abbreviations

AFM – Atomic force microscope

BF-BKT – $(BiFeO_3)_{0.4}$-$(Bi_{1/2}K_{1/2}TiO_3)_{0.6}$

BFC-BKT – $(BiFe_{0.9}Co_{0.1}O_3)_{0.4}$-$(Bi_{1/2}K_{1/2}TiO_3)_{0.6}$

EDX – Energy dispersive *X*-ray spectroscopy

FC – field cooling

FE – Ferroelectric

M-H – Magnetization-magnetic field

ME – Magnetoelectric

MFC – Multiferroic clusters

MFM – Magnet force microscopy

MNR – Magnetic nanoregions

MOKE – Magneto-optical kerr effect

MPB – Morphotropic phase boundary

P-E – Polarization-electric field

PFM – Piezoresponse force microscopy

PFW – $PbFe_{2/3}W_{1/3}O_3$

PNR – Polar nanoregions

PPLN – Periodically poled

PUND – Positive up negative down

PZT – $PbZr_{0.52}Ti_{0.48}O3$

SEM – Scanning electron microscopy

TEM – Transmission electron microscopy

TOF-SIMS – Time-of-flight secondary ion mass spectrometry

XRD – *X*-ray diffraction

ZFC – Zero field cooling

1 Introduction

1.1 **Motivation**

Single-phase magnetoelectric (ME) multiferroics are materials which display both ferroelectricity and magnetism in the same phase and exhibit coupling between the respective order-parameters. Since their 'birth' in the late 19th century, ME multiferroics have attracted scientists' attention because of their multiple order parameters and their ability for coupling between them. However, these materials are not only attractive because of their rich and complex physics but also for their prospects in sensor and memory technology. Anticipated applications are e.g. the creation of a four-state bit for data storage [1], magnetic sensors [2], [3], magnetoelectric memory [4], [5] and voltage-driven magnetic tunnel-junctions [6]. After a climax in research on multiferroics and magnetoelectrics in the 1970s followed by a decline in the subsequent two decades, there has been a steep rise in the number of publications in this area since 1998. It is an important area of research with the number of publications in this field having increased almost constantly over the past 25 years with 1496 articles published in 2014 (see Figure 1).
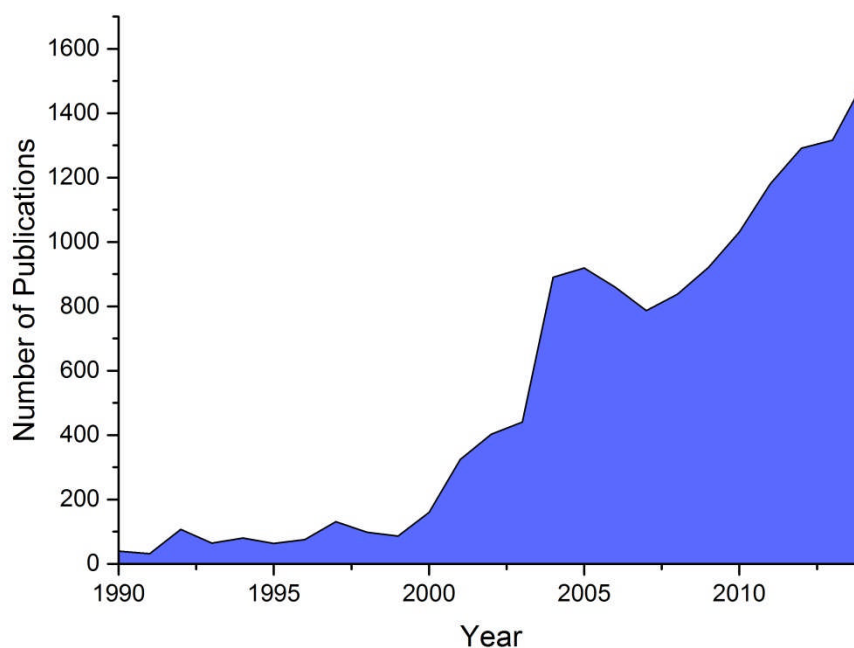
Figure 1 Number of publications from 1990 until 2014 as returned for the topic words "multiferroic" or "magnetoelectric" or equivalent words (source: www.scopus.com).

However, despite the fact that extensive research has been carried out, no single-phase multiferroic with both ferroelectric order and strong magnetism at room-temperature has been reported to date. In addition single-phase multiferroics usually only display weak ferromagnetic (WFM) behaviour at room-temperature, which arises from antiferromagnetic order with spin-canting that causes low magnetic susceptibility and in turn limits ME coupling [7]. It is the aim of this thesis, to show pathways to new single-phase multiferroics that display strong ME coupling but also to make a contribution towards understanding of the complex underlying physics of ME coupling mechanisms and occurrence of ferroelectricity and magnetic order at higher temperatures.

1.2 Scope and outline of this thesis

Perovskite based single-phase multiferroics displaying ME coupling at room-temperature are the main scope of this thesis. $BiFeO_3$ based solid solutions have been investigated in the author's research group for many years and

had previously been combined in solid solutions with other ferroelectric perovskites such as $PbTiO_3$ or $Bi_{1/2}K_{1/2}TiO_3$ to influence their properties. Thus these and related materials are the main focus of research for this project with the ultimate goals to find compositions with enhanced properties and to investigate mechanisms for ME coupling on a microscopic level.

To this extent, particular emphasis lies on investigation of ME properties on the micro- and nano-scale, using microscopy techniques such as piezoresponse force microscopy (PFM) and magnetic force microscopy (MFM), which are both based on atomic force microscopy (AFM). PFM and MFM are capable of investigating a material's dipolar electric and magnetic structure, respectively, with high spatial resolution. When they are combined with applied magnetic and electric fields respectively, they can be used to study ME effects locally. It is hoped that using these local techniques, coupling mechanisms in single-phase multiferroics, which are complex and not well understood yet, can be elucidated. Here, PFM under in-situ magnetic field is of particular importance, because in-situ experiments are expected to be particularly valuable for this purpose. In this context, the reproducibility of PFM signals is carefully investigated with the prospect of quantification of the ME coupling coefficients on a local scale.

Of course, local measurements need to be correlated with macroscopic properties to yield a complete picture of a material. Thus extensive studies of the macroscopic properties such as magnetic and dielectric behaviour, crystal structure and magnetic structure will be presented.

This thesis is organized in following chapters:

  Chapter 1 outlines motivation and scope of this thesis, which is followed by an introduction into the fields of ferroelectrics, magnetism and multiferroics. Finally, background information regarding crystal structure and properties of materials investigated in this thesis, are given.

  Chapter 2 aims at giving a concise but complete overview to all relevant methods and analytical techniques which are grouped into three categories: structural or chemical, electrical and magnetic characterisation techniques. Special emphasis lies on the technique PFM, the underlying contrast mechanism and signal representation.

Chapter 3 deals with statistical experiments on signal stability as well as practical aspects and common artifacts in PFM.

Chapter 4 describes a simple and inexpensive method which was developed in the course of this project, for marking of many individual micro-sized areas on a sample for investigation via microscopy.

Chapter 5 presents investigations of the multiferroic properties of the system $(PbZr_{0.52}Ti_{0.48}O_3)_x$-$(PbFe_{2/3}W_{1/3}O_3)_{1-x}$ (PZT-PFW). Special emphasis lies on the complex magnetic structure which is studied in detail.

Chapter 6 is the most important and extensive chapter. It presents results of detailed multiferroic investigations of the composition $(BiFe_{1-x}Co_xO_3)_{0.4}$-$(Bi_{1/2}K_{1/2}TiO_3)_{0.6}$ BFC-BKT. Local investigations of ME coupling are among the most important experiments in this chapter.

Chapter 7 gives general conclusions and summarizes most important findings of the whole project. Furthermore, plans for the future work are outlined.

1.3 Perovskite crystal structure

Many binary transition metal-oxides exhibit similar crystal-structures as the mineral perovskite $CaTiO_3$ named after Russian mineralogist Lev Perovski and are usually referred to as 'perovskites'. This class of materials is by far the most important class of ferroelectric and piezoelectric materials. They have a general composition of ABX_3 where A is usually a large cation bearing a 2+ charge such as Ba^{2+} and Pb^{2+}, B is a smaller 4+ charged ion such as Ti^{4+} and X is O^{2-} for the vast majority of perovskites. However, differently charged cations such as in $BiFeO_3$ with both A and B atoms having a 3+ charge are also common. Recently, perovskites with $A^+B^{2+}X^-_3$ where X is a halide ion (F^-, Cl^-, Br^-, I^-) and A being an organic alkyl ammonium cation have attracted significant attention in solar cell research [8]. It is also possible that one lattice site is occupied by different ions where the average charge needs to be appropriate so that charges are balanced. This is for example the case for $PbMg_{1/3}Nb_{2/3}O_3$ where 1/3 of all the B-sites is occupied by Mg^{2+}-ions while 2/3 are occupied by Nb^{5+}-ions which yields

an average charge of 4+ for the B-site. In such a case where the stoichiometry is fixed to certain proportion of ions defined by their charge, the material is referred to as complex perovskite. Cations can be distributed statistically i.e. disordered on a lattice site which often leads to so-called relaxor properties (see Section 1.4.3)). However, they can also occupy one lattice site in an ordered manner which leads to superstructures.

The ideal cubic perovskite unit cell can be described as follows: A-atoms occupy the corners of a cube which are surrounded by 12 X-atoms in the form of a cuboctahedron. In the centre of the cube, there is a B-atom which is coordinated octahedrally by 6 X-atoms which occupy the face centres of the cube. Alternatively, this unit cell might be described by a face centreed cubic (fcc or cubic close packing) lattice consisting of A- and X-atoms with B-atoms occupying one quarter of the octahedral interstices.

The unit cell might also be chosen that B-atoms occupy the corners while A-atoms occupy the centre of the cube. These two different unit cells are displayed in Figure 2 with coordination spheres illustrated by red bars.
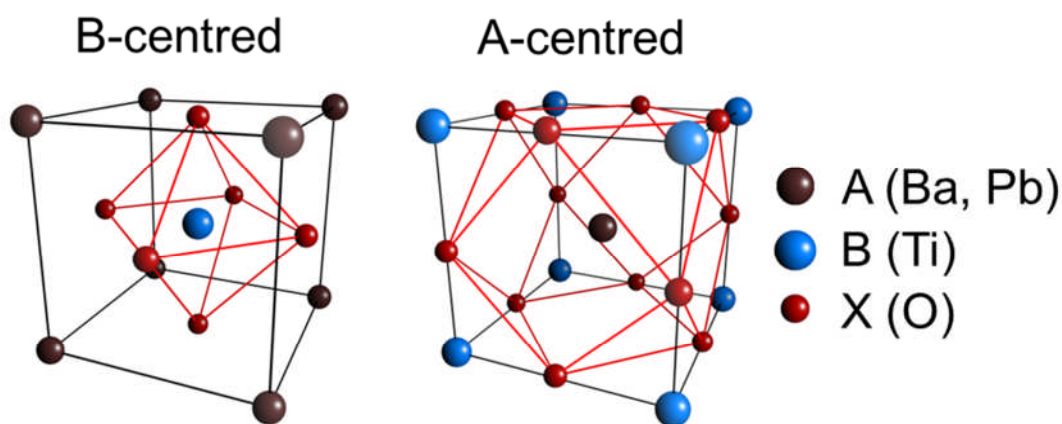
Figure 2 Schematic perosvkite unit cells with A-site, B-site and oxygen atoms in brown, blue and red respectively. The labels give examples for common atoms A-,B- and X-site atoms.

Often different perovskite compounds form a solid-solution which form a homogenous compound across the whole compositional range. These are called mixed perovskites where two different end member perovskites are 'mixed' which is illustrated by a hyphen between the chemical formulas of the corresponding perosvkites. An example of such a mixed perovskite is the

system $(BiFeO_3)_x$-$(PbTiO_3)_{1-x}$ where the proportion of the two components is given by x. Another prominent example is $(PbZrO_3)_{0.52}$-$(PbTiO_3)_{0.48}$ (lead zirconate titanate, PZT) which is usually written as $PbZr_{0.52}Ti_{0.48}O_3$. It is the most important ferroelectric and piezoelectric material from an application point of view and will be used as an exemplary material later (see Section 1.4.2).

1.4 **Ferroelectrics**

Generally, ferroelectrics belong to the family of dielectric materials which are insulating and can be polarized by an electric field due to spatial separation of positive and negative charges.

Ferroelectric materials however, exhibit a spontaneous polarization without application of an electric field below the Curie temperature T_C. This polarization is furthermore reversible by an electric field. Above T_C, ferroelectric materials lose their microscopic spontaneous polarization and become paraelectric. Usually, ferrroelectrics also display a characteristic hysteretic polarization *vs.* electric field (P-E) behaviour which is illustrated in Figure 3.
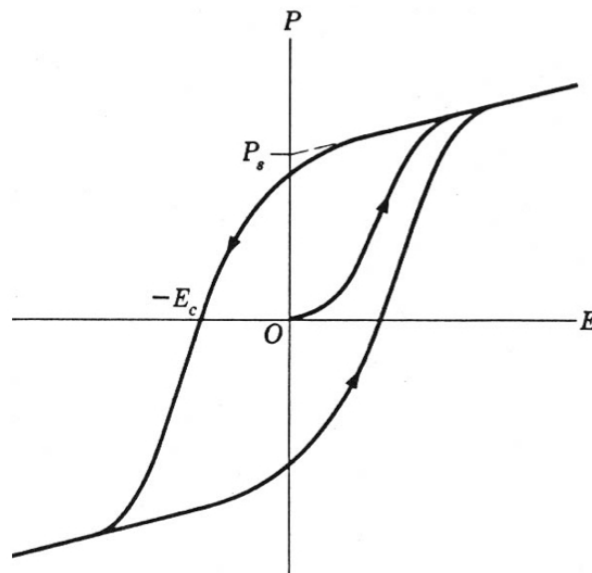
Figure 3 Characteristic polarization *vs.* electric field (P-E) hysteresis-loop [9].

To reduce the overall electric field which also reduces the systems energy, ferroelectrics form ferroelectric domains that are micro- or nanometre-sized

regions with uniform direction of polarization. These domains are randomly oriented if the material has not been subject to an electric field, which leaves the material without a macroscopic net-polarization. When a sufficiently large electric field is applied to the ferroelectric, its domains align in the direction of the electric field which gives rise to a net-polarization until a saturation-polarization P_S is reached. Even without an external electric field, the so-called remanent-polarization P_r remains. This polarization can be brought back to 0 by application of an inverse field with the strength E_c which is the coercive field. When the electric field is inverted, polarization in the opposite direction starts to occur until negative saturation is reached. The hysteresis loop is completed when the electric field direction is inverted once again until positive saturation is reached (Figure 3).

Another parameter that is characteristic for a ferroelectric is permittivity which describes a material's ability to transmit an electric field and how much electric field or flux is generated per unit charge in that medium. The more a material is polarizable, the higher is the electric displacement field generated per unit charge and the higher is the permittivity. The electric flux is however inversely proportional to permittivity. The relative permittivity ε_r is related to the electric susceptibility χ_e which is the constant of proportionality between an electric field E and induced dielectric polarization P:

$$P = \varepsilon_o \chi_e E$$

Equation 1-1

where

$$\varepsilon_r = \chi_e + 1$$

Equation 1-2

with the vacuum permittivity $\varepsilon_0 \approx 8.854 \cdot 10^{-12}$ F/m.

Since many ferroelectrics have a permittivity far above 100, ε_r can often be assumed to be χ_e in good approximation.

The permittivity is an essential parameter, which is frequently used to characterise phase transitions the ferroelectric to the paraeletric phase at the Curie temperature T_C (or Curie point), which is shown with $\varepsilon_r = \varepsilon$ in Figure 4.

First order
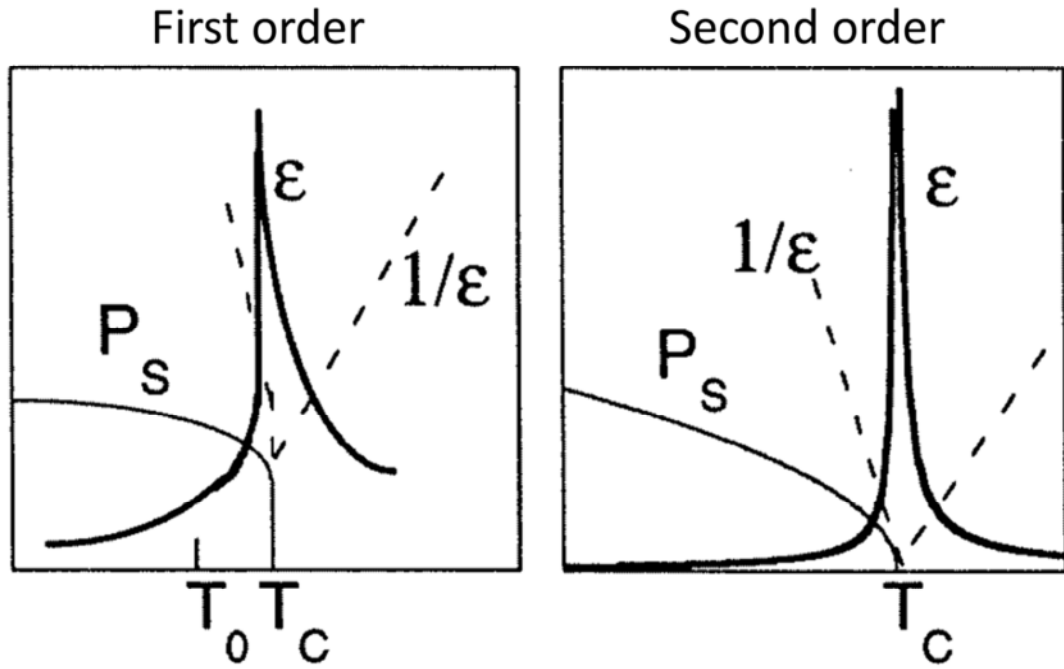
Second order

Figure 4 Characteristic development of permittivity ε and saturation polarization P_S *vs.* temperature for a first and second order phase transition [10].

At the phase transition, ε becomes very large, exhibits a sharp maximum and falls off above T_C according to the Curie-Weiss law:

$$\varepsilon = \varepsilon_0 + \frac{C}{T - T_0} \approx \frac{C}{T - T_0}$$

Equation 1-3

where C is the Curie constant and T_0 is the Curie-Weiss temperature which is smaller or equal to T_C.

Generally, two kinds of phase transitions, first order and second order, are usually distinguished. In a first order transition the order parameter which is the polarization in this case, exhibits a discontinuity at the phase transition while for a second order transition, the polarization changes continuously, but its first derivative is discontinuous at the transition temperature. Examples of ferroelectrics that display first and second order phase transitions are $BaTiO_3$ and $LiNbO_3$ respectively [10].

1.4.1 Ferroelectric phase transitions in $BaTiO_3$

$BaTiO_3$ is certainly the standard model ferroelectric, since it exhibits a number of structural phase transitions into various crystal systems typical of

perovskite ferroelectrics, and has been intensively studied. These phase transitions are illustrated in Figure 5.
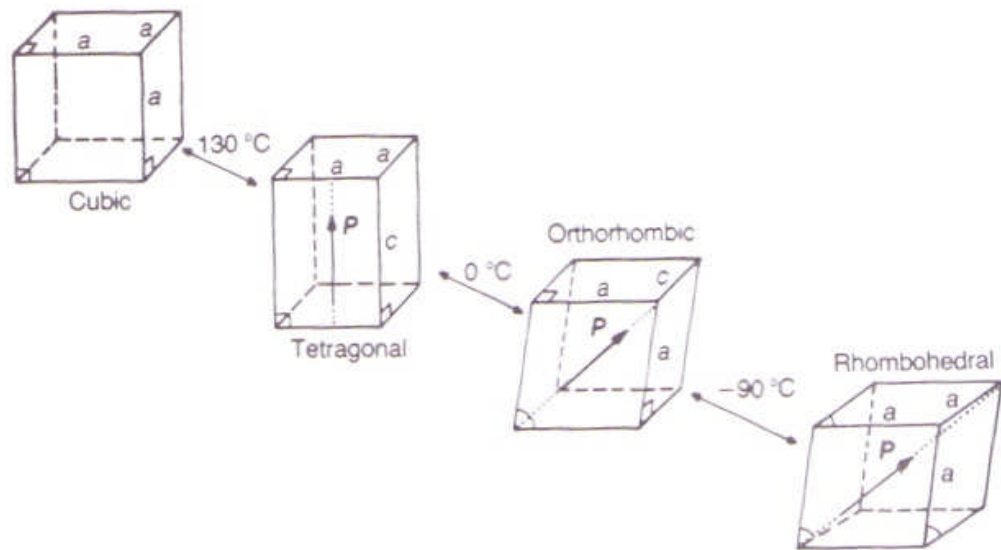
Figure 5 Ferroelectric phase transitions in $BaTiO_3$ [11].

Although $BaTiO_3$ exhibits several ferroelectric phase transitions, only the highest transition temperature where, upon cooling ferroelectricity occurs first, is defined as the Curie temperature. This is the transition from the paraelectric cubic phase, to the ferroelectric tetragonal phase at approximately 130 °C. When cooling further below 0 °C, the structure changes from a tetragonal to an orthorhombic one, until a final phase transition to a rhombohedral crystal structure occurs at -90 °C.

Ferroelectricity in perovskites is mostly due to the off-centre position of the B-site cation (in some cases, it is due to the movement of A-site cations). In cases where there is a shift of the B-site cation, it is shifted towards the <100>, <110> or <111> direction of the cubic system for tetragonal, orthorhombic or rhombohedral crystal-classes respectively. If we consider the B-cation relative to the surrounding oxygen octahedron, these movements correspond to the B-cation moving closer to a corner, an edge or a plane of the octahedron respectively. This relation illustrates the resulting symmetry as well as the number of equivalent directions of B-cation movement. Figure 6 shows idealized perovskite unit-cells for tetragonal,

orthorhombic and rhombohedral symmetry and lists the corresponding directions of B-cation displacement and the number of equivalent directions.
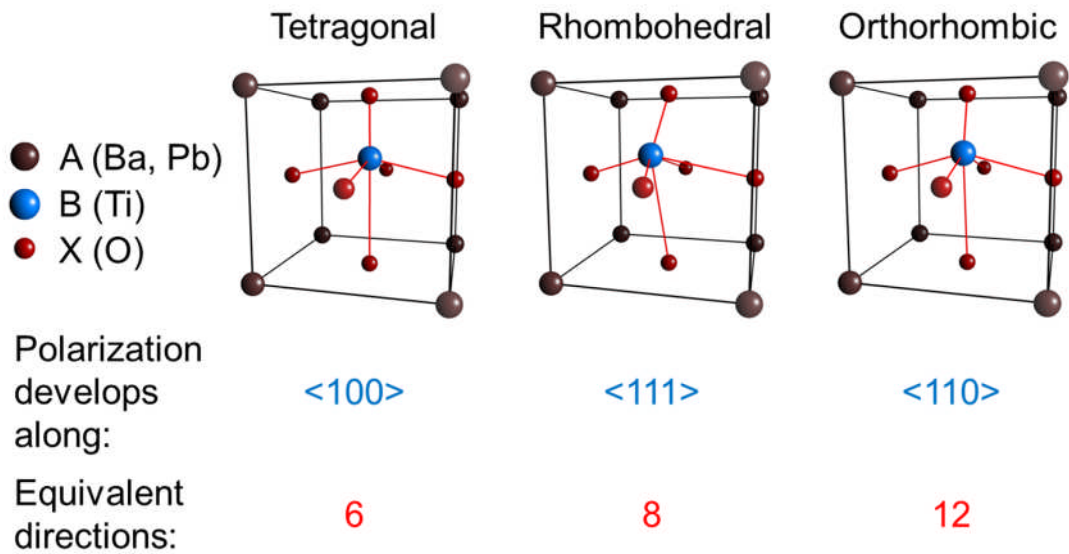
Figure 6 Schematic perosvkite unit cells representing the three major ferroelectric crystal systems. The directions of polarization referenced to the cubic prototype cell and the number of equivalent directions are given underneath.

Note that B-site ion displacements are exaggerated for clarity. The angles between the directions of B-cation displacement define possible angles between ferroelectric domains for different crystal systems. These angles are 90° and 180° in case of tetragonal and 71°, 109° and 180° in case of rhombohedral. Furthermore, the polarization direction gives the number of equivalent directions which are 6,8 and 12 in tetragonal, orthorhombic and rhombohedral crystal systems respectively. The number of equivalent directions are important for poling of polycrystalline ceramics where a higher number of equivalent directions allows for domains in a polycrystalline ceramic to align with the field direction more effectively.

1.4.2 Morphotropic phase boundary

The morphotropic phase boundary (MPB) is defined as a (nearly) temperature independent phase boundary between differing symmetries due to compositional change [12]. Its role will be explained by a very prominent example, PZT, which is by far the most important piezoelectric material for actuators and transducers and has been the subject of intense research.

$PbTiO_3$ is a tetragonal ferroelectric with space group P4mm and a Curie temperature of 490°C [13] while $PbZrO_3$ is orthorhombic and antiferroelectric with a Curie temperature of approximately 228°C [14].

Often it is useful to write mixed perovskites in the form $(PbZrO_3)_x$-$(PbTiO_3)_{1-x}$ instead of $PbZr_xTi_{1-x}O_3$, which facilitates understanding the relationship between structure and composition, since the structure of the mixed perovskite depends on the structure of the two (end members) perovskite components. Usually end members with different symmetry are combined in a mixed perovskite and the structure of the mixed perovskite usually adopts the symmetry of the high content end member with a compositional region of mixed symmetry between the two extremes. This behaviour can be observed in the phase diagram of PZT shown in Figure 7.
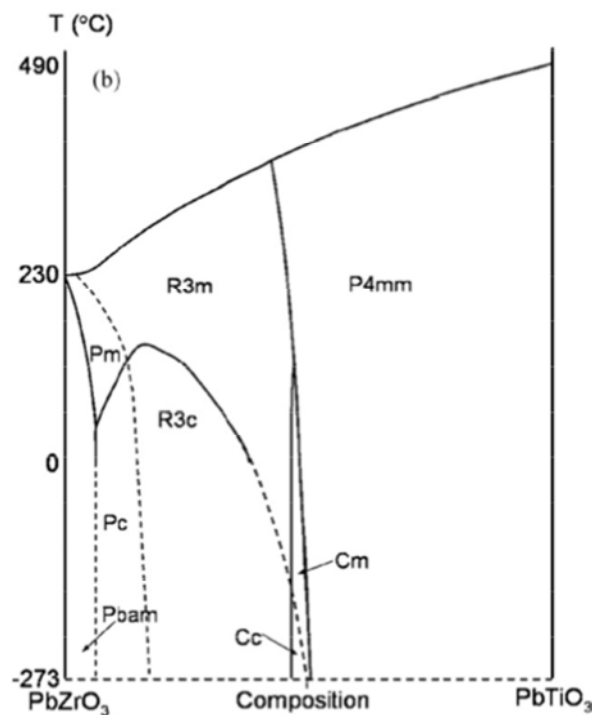
Figure 7 Phase diagram of PZT [15].

The phase diagram shows that the mixed perovskite adopts orthorhombic (Pbam) and tetragonal (P4mm) symmetries of the pure components $PbZrO_3$ and $PbTiO_3$ respectively where these are in high concentration. When going from low to high $PbTiO_3$ concentrations (from left to right in Figure 7), several MPBs are crossed where the crystal structure changes from orthorhombic (Pbam) to monoclinic (Pc) to rhombohedral (R3c). More recent

investigations suggested the existence of a monoclinic (Cm) phase at the important MPB at x = 0.52 which separates rhombohedral and tetragonal structures [16], [17].

The outstanding piezoelectric properties of PZT are attributed to this MPB. As mentioned in Section 1.4.1, a large number of equivalent directions of polarization is beneficial for poling of polycrystalline ferroelectric ceramics. The fact that e.g. piezoelectric coefficients usually peak at the morphotropic phase boundary in a solid solution is explained by the large number of equivalent directions of polarization available from two or in the case of PZT perhaps even three crystal systems. This is illustrated in Figure 8.
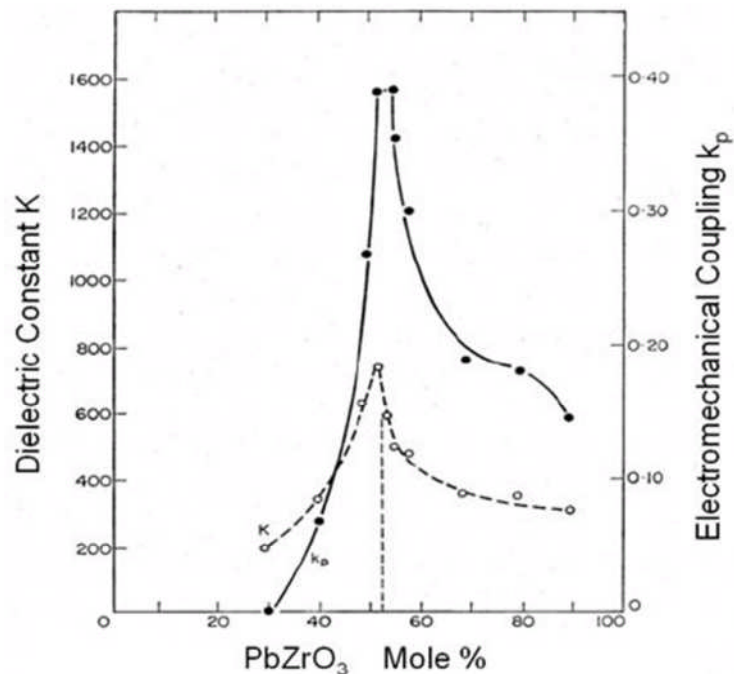
Figure 8 Effect of the morphotropic phase boundary (MPB) in PZT. Dielectric constant (= permittivity, dashed line) and electromechanical coupling coefficient *vs.* mole percentage of $PbZrO_3$ in $PbZr_xTi_{1-x}O_3$ [18]. Both permittivity and electromechanical coupling coefficient peak at the MPB.

It can be observed that the dielectric constant or permittivity as well as the electromechanical coupling coefficient, which is the measure of energy conversion between electric and acoustic energy for a piezoelectric, have a very large and sharp maximum at the MPB.

Often rhombohedral and tetragonal end member perovskites are combined to create an MPB as in PZT which results in 14 available polarization

directions at the MPB in contrast to 6 and 8 available directions for pure tetragonal and rhombohedral phases respectively.

1.4.3 **Relaxor ferroelectrics**

There exists another type of ferroelectric material, which is known as relaxor ferroelectric or relaxor [19]. These are characterized mainly by strong frequency dispersion of broad relaxation peaks in permittivity *vs.* temperature curves and by a lack of macroscopic symmetry breaking at the phase transition [20]. The frequency dispersion behaviour is displayed in Figure 9.
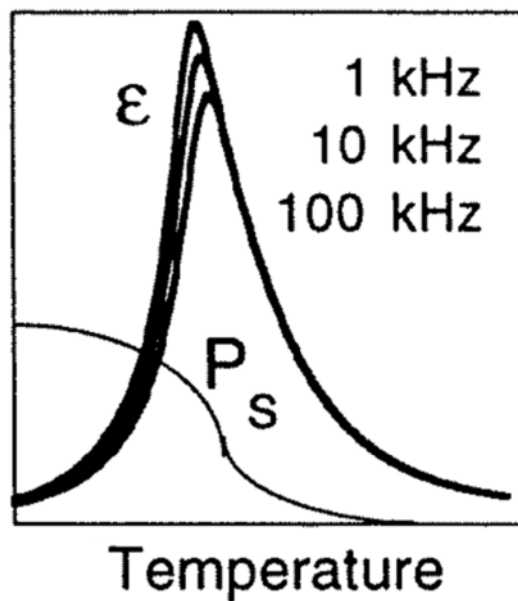
Figure 9 Characteristic development of permittivity ε and saturation polarization P_S *vs.* temperature of a relaxor ferroelectric [10].

It is widely assumed that this behaviour is caused by chemical disorder in the lattice of relaxors. This gives rise to charged compositional fluctuations, which cause quenched random electric fields (random field fluctuation [21]) promoting the freezing of polar nanoregions (PNR) [22], [23]. The archetypical relaxor which has been studied intensively is $PbMg_{1/3}Nb_{2/3}O_3$.

Relaxor ferroelectrics are commercially important mainly in the form of single crystals such as $(PbMg_{1/3}Nb_{2/3}O_3)_x$-$(PbTiO_3)_{1-x}$ (PMN-PT) or $(PbZn_{1/3}Nb_{2/3}O_3)_x$-$(PbTiO_3)_{1-x}$ (PZN-PT), which are widely used as sensors and transducers especially in ultrasound imaging probes and sonar devices [24]. Furthermore, lead free relaxors attract increasing attention due to

legislation that forbids the use of lead in products [25]. However, so far there is still a memorandum on lead containing piezoelectric devices like PZT since lead free cannot yet compete with conventional PZT ceramics.

1.4.4 **Ergodic and non-ergodic relaxor ferroelectrics**

There exist relaxor ferroelectrics where PNR undergo a freezing transition similar to disordered magnetic spin-glasses [26], [27]. Here, PNR freeze into a dipolar cluster-glass state on cooling below the low-f peak temperature T_f [28]. This class of relaxors is connected with the term ergodicity which was elaborated by Boltzmann from the Greek words for work (ergon) and path (odos) [29]. A statistical process is termed ergodic when the time average is equal to the ensemble average. This can be best explained by giving an example. A process would be ergodic if the average of 10^6 consecutive throws of one dice (time average) would be equal to the average of 10^6 dice all thrown at once [30]. This would be the case for perfect non-interacting dice but not if the dice would interact with each other, for example if two specific sides of the dice were magnetic and would attract or repel each other. The same is the case for frozen PNR which begin to interact upon cooling. Here, ergodicity is broken and the relaxor thus behaves glass-like. Since interactions are frustrated, random polarization directions are obtained instead of a parallel alignment as in ferroelectrics. Reasonably large external electric fields, suffice to break the glassy disorder and to align all dipolar moments at saturation which induces a ferroelectric state. The frozen or static PNR (SPNR) characteristic for a non-ergodic relaxor ferroelectric differ from regular domains. While domains are adapted to the crystal lattice via 'ordered' fields and covalent bonds, SPNR are stabilized by a local excess of a certain component of random electric fields which are generated by the inherent charge disorder of the material. This usually gives rise to irregular shapes and fractal surfaces of the clusters, unlike for regular domains. However, SPNR and FE domains behave similarly in that both are polarized permanently and can be poled.

1.5 **Magnetism**

The field of magnetism is very broad and complex. Within the scope of this thesis, only a brief introduction covering relevant aspects will be given.

In principle magnetism arises from two basic phenomena:

- Moving electric charges as caused by an electrical current
- Magnetic moments of elementary particles due to the intrinsic angular momenta ('spins'), e.g. of electrons or neutrons

For considerations related to magnetic structure which are relevant in the context of this thesis, only the magnetic moments of electrons are important which are also referred to as atomic moments since the magnetic moments due to nuclei are negligible in terms of magnetization. There exist 5 basic classes of magnetism in matter: diamagnetism, paramagnetism, ferromagnetism, antiferromagnetism and ferrimagnetism where the three latter classes are due to cooperating spins.

1.5.1 **Diamagnetism and paramagnetism**

Diamagnetism is a property of all matter and is an effect of the Pauli exclusion principle which states that one orbital can only be populated by two electrons with opposite spins which cancel each other out. Materials which only contain paired electrons are diamagnetic which is the case e.g. for pyrolitic graphite or most organic compounds. These materials are repelled by magnetic fields since they oppose an external magnetic field. This results in a negative, albeit low magnetic susceptibility χ_m which is the factor of proportionality between magnetization M and magnetic field H:

$$M = \chi_m H.$$

Equation 1-4

This linear relation is true for diamagnetic and paramagnetic materials in low fields. Analogously to the relative permittivity (Equation 1-2), the relative magnetic permeability μ_r is:

$$\mu_r = \chi_m + 1.$$

Equation 1-5

Paramagnetic materials are materials which contain unpaired electrons that do not interact. Thus the associated spins, are randomized in the absence of a magnetic field and yield no net spontaneous magnetization. However, in an external magnetic field, the atomic dipoles align with the field as illustrated in Figure 10.
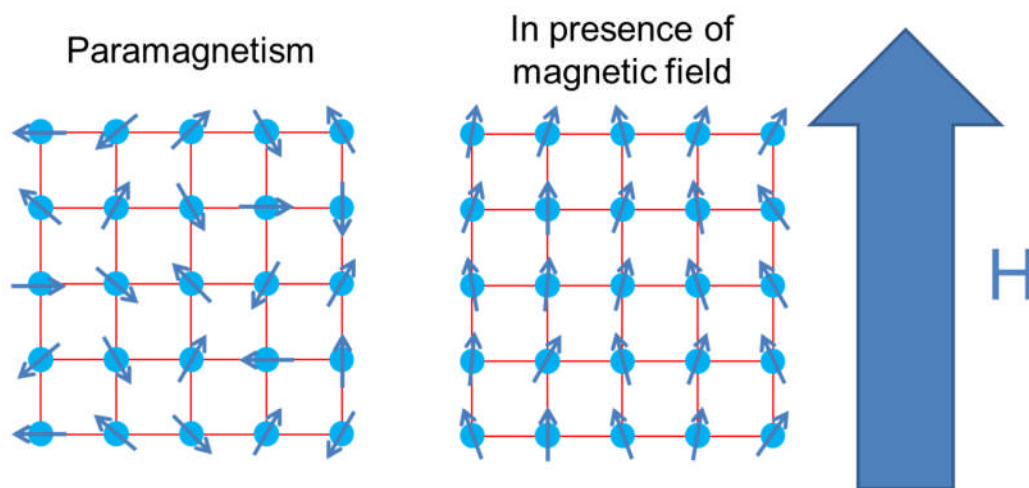
Figure 10 Schematic illustration of paramagnetism and field aligned paramagnetism. Atomic magnetic moments are oriented randomly in absence of external magnetic field resulting in no permanent net magnetization. In presence of magnetic field spins are aligned with field which induces magnetization.

As a consequence, the material is attracted by a magnetic field and χ_m is positive but low. Many metals are paramagnetic as well as some organic radicals or the O_2 molecule.

However, when spins interact with each other, this leads to ordered cooperative magnetic structures which will be treated below.

1.5.2 Ferromagnetism, antiferromagnetism and ferrimagnetism

In ferro-, ferri- and antiferromagnetic materials, spins are ordered inside magnetic domains. This behaviour is often termed magnetically coupled or magnetically ordered. In magnetically ordered materials there exists an interaction between the spins which leads to ordering of the otherwise randomly oriented moments. This interaction is called exchange interaction. Its sign determines whether moments order ferromagnetically (positive sign) or antiferromagnetically (negative sign). The simplest type of magnetic order is ferromagnetism where all spins are aligned parallel. Among all metals,

only few are ferromagnetic at room-temperature such as the well-known elements Fe, Co and Ni but also Gd. Ferromagnetic materials exhibit spontaneous magnetization even in absence of a magnetic field (remanent magnetization). In analogy to ferroelectrics, they exhibit hysteresis and form microscopic domains. In materials with antiferromagnetic order, neighbouring moments are aligned antiparallel. Thus all atomic magnetic moments compensate each other completely, resulting in no net magnetization. Common antiferromagnetic materials are transition metal oxides such as α-Fe_2O_3 (Haematite) or Cr_2O_3 but also $BiFeO_3$. Their ordering temperature is called Néel temperature, named after the discoverer of antiferromagnetism Louis Néel. However, there exist forms of antiferromagnetism where spins do not compensate each other completely. One of these is ferrimagnetism, where two sublattices are present with unequal spins, which results in a residual net magnetization. Common examples of ferrimagnetics are spinel type materials such as $CoFe_2O_4$ (cobalt ferrite) or Fe_3O_4 (Magnetite). The antiparallel spins in antiferromagnets can also be slightly canted (non-collinear) due to Dzyaloshinskii-Morya interactions [31] which results in a small residual magnetization. This is called weak or parasitic ferromagnetism and is approximately 2-3 orders of magnitude weaker than ferromagnetism. Examples are α-Fe_2O_3 which becomes weakly ferromagnetic at elevated temperatures but also thin-film $BiFeO_3$ [32]. The above described magnetic orders are represented schematically in Figure 11.
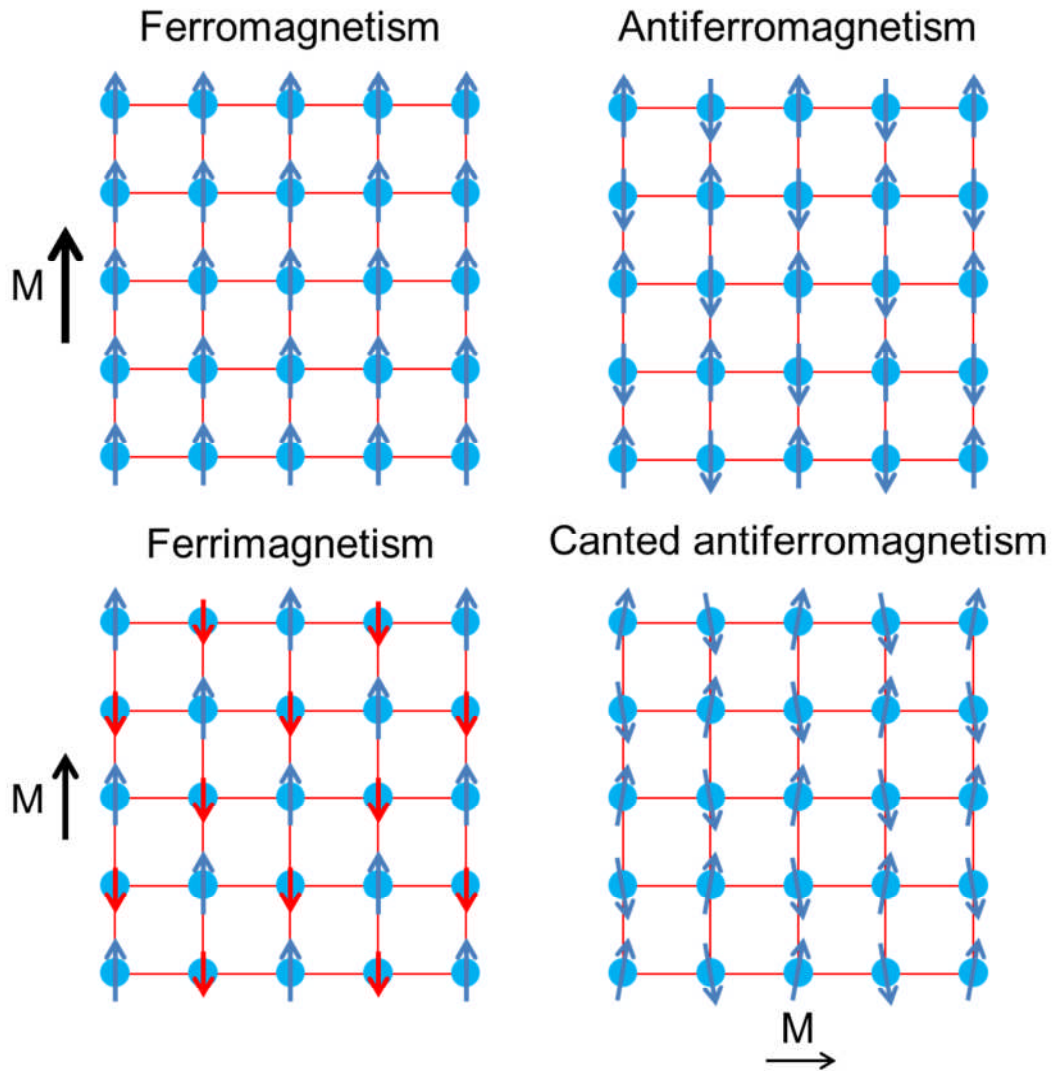
Figure 11 Schematic illustrations of basic magnetic orders. Ferromagnetism: Atomic moments are aligned parallel resulting in spontaneous magnetization. Antiferromagnetism: Atomic moments are aligned antiparallel which compensate each other, resulting in no net magnetization. Ferrimagnetism: Atomic moments are aligned antiparallel but the two sublattices do not compensate each other completely, resulting in a net magnetization. Canted antiferromagnetism: Weak ferromagnetic behaviour arises from canted spins which do not compensate each other completely. Note that the canting angle is exaggerated for clarity. Resulting net magnetizations are represented by black arrows with sizes of arrows illustrating the magnitude of magnetization.

Above the Curie temperature thermal energy overcompensates the exchange interaction and magnetic order is broken while materials become paramagnetic.

Despite all analogies between ferroelectric and ferromagnetic materials, an important difference is however, that while for a ferroelectric material, the atomic structure always changes when crossing its Curie temperature, this is

not the case for ferromagnetic materials where only the spin structure changes.

1.5.3 Cycloidal spin superstructure

Apart from the above mentioned magnetic structures, there exist more complex ones which are not necessarily commensurate with the crystal lattice. One example is the cycloidal spin structure encountered in bulk $BiFeO_3$. Below the Néel temperature of $T_N = 653$ K it attains so-called g-type antiferromagnetic magnetic order. However, the spins are slightly canted which results in small uncompensated magnetic moments. However, in case of bulk $BiFeO_3$ this uncompensated magnetization is cancelled out by an additional incommensurate cycloidal magnetic superstructure, which was found to have a correlation length of approximately 64 nm [33] as illustrated in Figure 12.
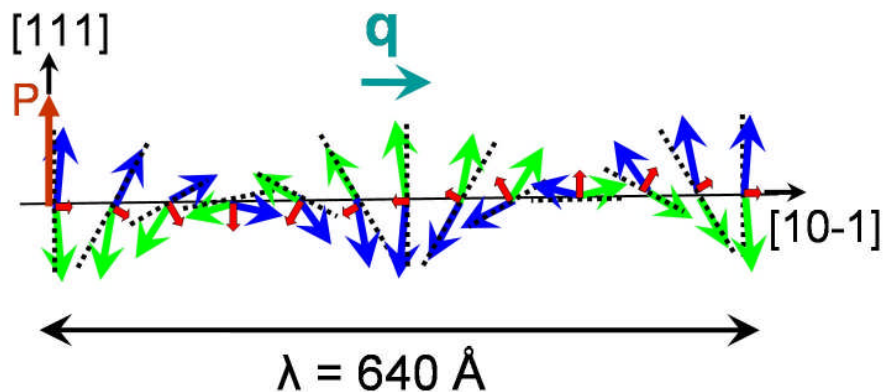
Figure 12 Cycloidal spin superstructure in bulk $BiFeO_3$ [33].

1.5.4 Superparamagnetism

Another class of magnetic materials are superparamagnetics. The word 'super' refers to a superstructure of spins (or spins) which as a whole act like one macroscopic superspin. In superparamagnetic materials, although a large number of spins couple magnetically to form one superspin, those superspins are not coupled magnetically to each other but are randomly oriented like spins in a paramagnet. The classical type of material, where superparamagnetism occurs is realized by ensembles of magnetic nanoparticles [34]–[36]. Here, the magnetization of each nanoparticle is so

small that thermal energy above the blocking-temperature T_B can flip their magnetic moment. As an effect, the material appears to be paramagnetic if the time constant of the measurement is much higher than the Néel relaxation time which is the typical time between two flips. However, if subjected to an external magnetic field, the superspins align with the field and create the same high saturation magnetization as for a ferromagnetic material, which is lost immediately once the magnetic field is removed again. As a result, the magnetization *vs.* magnetic field behaviour resembles that of a ferromagnetic material but without any hysteresis or coercivity as shown in Figure 13.
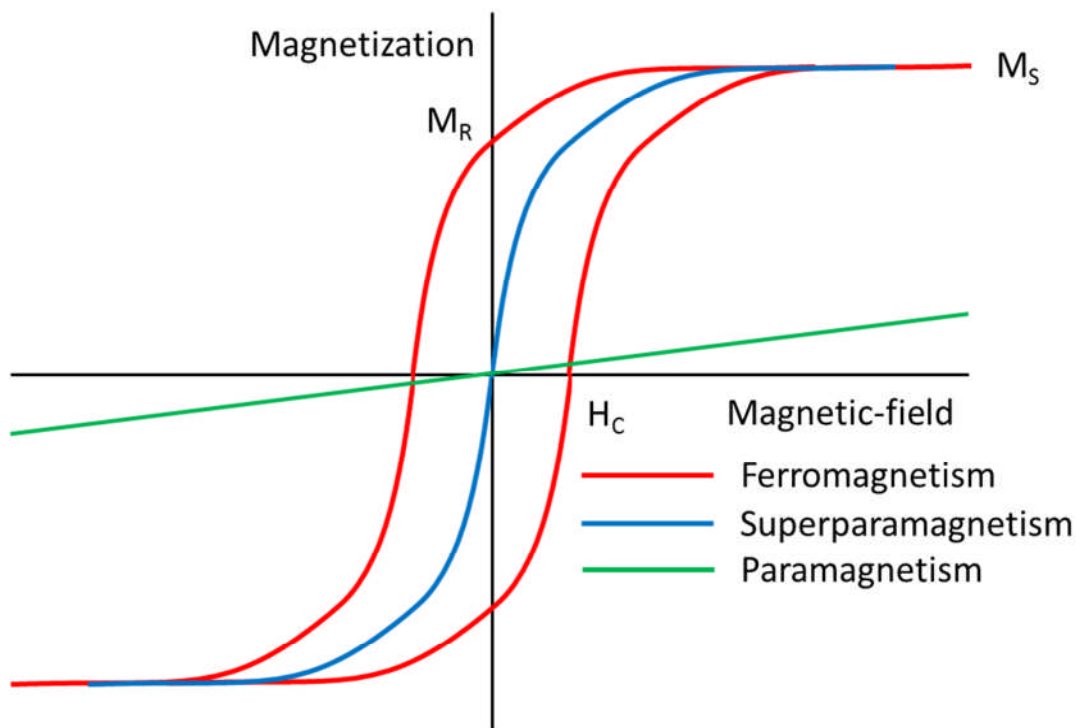
Figure 13 Characteristic magnetization *vs.* magnetic field behaviour of ferromagnetic (—), superparamagnetic (—) and paramagnetic materials (—).

A characteristic of superparamagnetic materials is the blocking transition which is usually measured using Zero-field cooling (ZFC, or more correctly: field heating after zero-field cooling, ZFC-FH) and field cooling (FC) magnetization *vs.* temperature curves. The sample is cooled first at zero field to low temperatures (approximately 5 K). During heating, the magnetization is measured at low fields (approximately 100 Oe) so as not to align any magnetic moments with the field. At low temperatures, the

superparamagnetic particles are frozen, i.e. their magnetization does not flip. However, since no field was applied during cooling, they are in random orientation (due to high temperature relaxation) which leads to a low magnetization. Upon heating, the superspins start to melt, and progressively align with the field leading to higher magnetization. However, at certain temperatures the nanoparticles also start to thermally relax again which leads to decreased magnetization. Thus, a characteristic maximum corresponding to T_B appears in the ZFC curve which is shown in Figure 14.
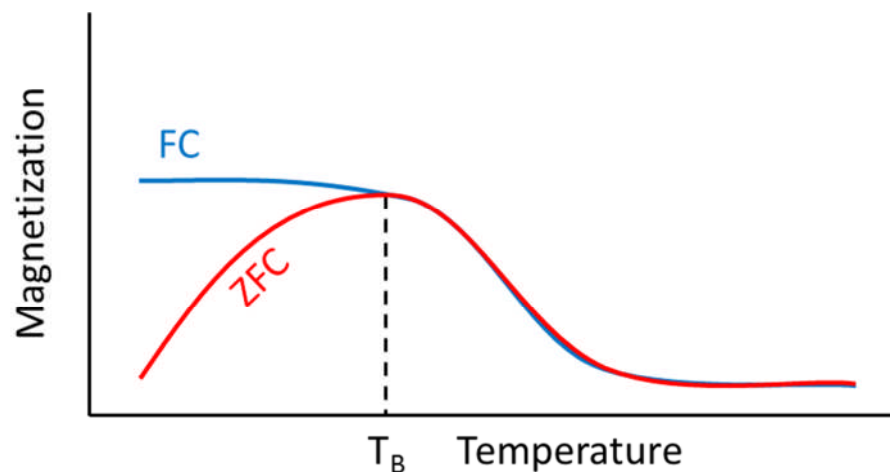
Figure 14 Characteristic blocking behaviour of a superparamagnetic material as observed with zero-field cooling (ZFC, —) and field cooling (FC, —) magnetization *vs.* temperature curves. The maximum in the ZFC curve corresponds to the blocking temperature T_B.

In the subsequent field cooling measurement, the magnetization plateaux below T_B which is typically below 50-250 K for particle sizes in the range of 5-20 nm where smaller particles have lower blocking temperatures [35], [37], [38].

It is very important to note that superparamagnetism is a dynamic process and that T_B depends strongly on the time constant of the measurement. In case of a magnetic nanoparticle, there are usually only two stable orientations of the magnetic moment due to the magnetic anisotropy. These orientations are antiparallel to each other and separated by an energy barrier. At temperatures above 0, there is a probability for the magnetic moment to reverse its orientation. The mean time between two flips of the

orientation is called the mean relaxation time τ_N which is given by the following Néel-Arrhenius term:

$$\tau_N = \tau_0 \exp\left(\frac{KV}{k_B T}\right)$$

where τ_0 is the so called attempt time which is characteristic of the material (10^{-9}-10^{-10} s), K is the magnetic anisotropy and V is the volume of the magnetic nanoparticle, while k_B is the Boltzmann constant and T is temperature.

If the magnetization of a nanoparticle is measured with different methods, the result of the measurement will depend strongly on the measurement times τ_m of the method. When τ_m is much larger than τ_N, the magnetization of the particle will flip several times during the measurement which results in a 0 net magnetization and thus in superparamagnetic behaviour. In case τ_m is much smaller than τ_N, the nanoparticle will appear to be blocked in its initial state. A transition between the blocked and the superparamagnetic state will occur at the blocking temperature T_B when $\tau_m = \tau_N$, which is given below:

$$T_B = \frac{KV}{k_B \ln\left(\frac{\tau_m}{\tau_0}\right)}$$

In contrast to the measurement time dependent blocking transition, a classical Curie transition from the ferromagnetic to the paramagnetic state, is static and thus independent of the measurement time.

1.5.4.1 Superparamagnetism in relaxor ferroelectrics

Magnetic nanoparticles are not the only materials which display superparamagnetic behaviour. It was e.g. also found in single crystals of the relaxor ferroelectric $(BiFeO_3)_{2/3}$-$(BaTiO_3)_{1/3}$. Here, Soda et al. found that the magnetic and the atomic coherence length measured by neutron diffraction and neutron diffuse scattering respectively, were very similar over a wide temperature range [39]. These short coherence lengths were attributed to

the presence of PNR and magnetic nanodomains and it was concluded that the magnetic nanodomains are due to the presence of PNR which give a spatial constraint to the magnetic nanodomains and thus induce superparamagnetism.

Also in the relaxor ferroelectric $PbFe_{1/2}Nb_{1/2}O_3$, a superparamagnetic cluster glass state was found in single crystals below 30 K [40] while T_N = 153 K was found. Interestingly, in thin-films of the same material also exhibiting relaxor properties, there are blocking transitions at 170 and 200 K found by Correa et al. [41] and Peng et al. [42] respectively, and weak ferromagnetic behaviour even above this temperature with superparamagnetic-like M-H-loop at room-temperature, exhibiting low coercivity.

1.6 **Multiferroics**

Now that both ferroelectricity and ferromagnetism have been introduced, we will discuss the combination these two phenomena in multiferroics.

The subject of multiferroics is relatively old with first experiments and prediction of the ME effect dating back to the late 19th century and further important experiments on Cr_2O_3 in the late 1950s [7]. The subject gradually attracted more attention until a climax was reached in the 1970s followed by a decline in the subsequent two decades, which was mainly due to the low encountered magnetoelectric coupling coefficients which made applications elusive. However, as mentioned in the introduction (Section 1.1), the number of publications in this area is rising steeply since the late 1990s.

Multiferroic materials combine at least two ferroic order parameters which are polarization P, magnetization M or strain ε in the case of ferrelectricity, ferromagnetism or ferroelasticity respectively [43]. These order parameters must be spontaneously nonzero below their respective critical termperatures T_C. However, this initial definition was softened to incorporate also antiferromagnetic or antiferroelectric materials because of their magnetic or electric order, repectively. Figure 15 schematically illustrates these order parameters and how they are controlled by their respective driving forces, viz. electric field E, magnetic field H, and mechanical stress σ as well as possible interactions among them.
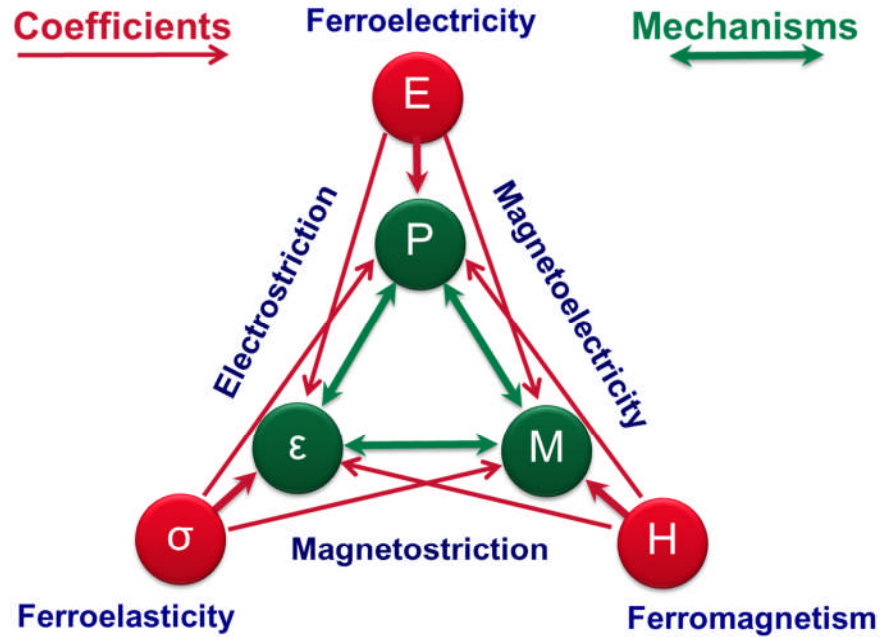
Figure 15 Schematic illustration of possible ferroic order parameters and their respective driving forces in multiferroics. Involved coefficients are indicated by red, while mechanisms are illustrated by green arrows (adapted from [44]).

A classic example of such coupling is e.g. electrostriction (or piezoelectricity), where coupling is between σ and P in case of the direct and between E and ε for the converse effect. Analogously, coupling between H and P is called direct while coupling between E and M is called converse ME coupling.

In case of many multiferroics (e.g. composites) the direct mechanism between P and M might not be available and ε becomes necessary as a mediator in a stress-strain mediated coupling mechanism.

1.6.1 Magnetoelectric coupling

The direct linear ME coupling-coefficient is obtained from an expansion of the free energy density into a power series of the field component, H_j and E_j [7], and can be represented as follows:

$$\alpha_{ij} = \frac{\partial P_i}{\partial H_j}$$

Equation 1-8

with P_i being the ith component of the electrical polarization and H_j being the jth component of the external magnetic field, respectively [7]. In simple words, the linear ME coefficient is the change of polarization with applied magnetic field. However, one should note that in ferroic materials, the resultant magnetic field or magnetic flux density $B = \mu_0 H + M$ can differ significantly from the external magnetic field H.

Often especially in the case of composite multiferroics, the so-called voltage coefficient is used which relates a change of the electric field E_i to the magnetic field H_j and is connected with α_{ij} via ε:

$$\alpha_{ij}^V = \frac{\partial E_i}{\partial H_j} = \alpha_{ij}\varepsilon\varepsilon_0.$$

Equation 1-9

The converse linear ME coupling-coefficient α_c can be expressed as follows:

$$\alpha_{ij}^c = \mu_0 \frac{\partial M_i}{\partial E_j}$$

Equation 1-10

with μ_0 = vacuum-permeability.

The converse ME coupling coefficient is the change of magnetization with applied electric field. Like for the direct ME effect, in ferroic materials, also the resultant electric field or dielectric displacement field $D = \varepsilon_0 E + P$ can differ substantially from E. There exist also higher order coupling coefficients for example the 'paramagnetoelectric' effect ($P_i = 1/2\beta_{ijk}H_jH_k$) that was found in piezoelectric and paramagnetic $NiSO_4 \cdot 6H_2O$ where polarization depends bilinearly on the magnetic field [45].

A fundamental limit to ME coupling is the given by electric permittivity and magnetic permeability [7]:

$$\alpha_{ij}^2 \leq \varepsilon_{ii}\mu_{jj}$$

Equation 1-11

This implies that only for materials with both large electric permittivity and magnetic permeability α can be large, too. Therefore, a material should be

both ferroelectric and ferromagnetic to exhibit a large ME coupling coefficient.

1.6.2 Classes of multiferroic and magnetoelectric materials

In general today two classes of multiferroics are usually distinguished.

- Single-phase multiferroics
- Composite multiferroics

While in single-phase multiferroics the two ferroic order parameters arise from a single-phase, this is not the case for composite multiferroics which consist of separate ferroelectric and ferromagnetic phases which are coupled to each other mechanically.

1.6.3 Single-phase multiferroics

As was shown in Section 1.6.1 single-phase multiferroics should ideally be both ferroelectric and ferromagnetic. However, it can be understood relatively easily that there is a conflict at least between ferroelectric and real ferromagnetic order not including any weaker ferromagnetic-like behaviour. While ferroelectrics are usually metal oxides as in the case of perovskites or at least metal non-metal compounds, true ferromagnets are usually conducting metals or metal alloys. Here paramagnetic atoms are nearest neighbours and the sign of the exchange interaction is positive which leads to ferromagnetism. In metal-oxide compounds such as perovskites, the exchange interaction is usually negative due to the superexchange mechanism mediated by oxygen ions which enables next-to-nearest neighbour coupling and leads to antiferromagnetic order. Although there are cases where superexchange leads to ferromagnetic order, this is relatively rare. A prominent example of a ferromagnetic perovskite is $La_{0.7}Sr_{0.3}MnO_3$ (LSMO), where ferromagnetism is due the double-exchange mechanism which is enabled by the presence of Mn^{3+} and Mn^{4+} ions [46]. This mechanism is, however, also responsible for the material's large conductivity since charges can hop from Mn^{3+} to Mn^{4+} ions which makes it unsuitable as a single-phase mulitferroic because a ferroelectric cannot be electrically conductive by definition. The potential for applications of LSMO lies mainly in the area of spintronics.

Additionally to the above mentioned problems, it was shown by Hill (now Spaldin) that in general, single-phase multiferroics are very rare [47]. This is primarily due to the fact that ions with partially filled electron shells as required for magnetism, reduce the tendency for an off-centre ferroelectric distortion. This can be best explained by the example of $BaTiO_3$ where Ti 3d-O 2p hybridization is essential for stabilizing the ferroelectric distortion. For an effective hybridization, it is important that the d states are unoccupied while partly filled d states are often unfavourable for the emergence of ferroelectricity, since these can for example lead to a Jahn-Teller distortion like in $LaMnO_3$ or $YTiO_3$ which compete against a ferroelectric distortion [47].

1.6.4 Classes of single-phase multiferroics

Smolenskii and Chupis divided single-phase multiferroics into four major groups [48]:

1. Perovskite compounds of general formula ABO_3 in which the B cation sites are partly or fully occupied by magnetic ions possessing unpaired electrons with A = Bi, Pb, Ba, Ca and B = Fe, Cr, Mn, $Fe_{1/2}/Nb_{1/2}$, $Fe_{1/2}/Ta_{1/2}$, $Fe_{2/3}/W_{1/3}$ [46], [49], [50]. It is probably the largest group of multiferroic materials while $BiFeO_3$ is by far the most widely studied and perhaps the most promising single-phase multiferroic due to its high ferroelectric and antiferromagnetic ordering temperatures. $BiFeO_3$ will be treated separately in more detail in Section 1.7.1. Perovskite-like layered compounds such as referring to Aurivilius phases with the general formula $(Bi_2O_2)(A_{n-1}B_nO_{3n+1})$ can be also counted to this class. They have attracted increasing attention recently [51] and might be among the most promising single-phase multiferroics. The superparamagnetic relaxor multiferroics mentioned in Section 1.5.4.1 also belong to this class.

2. Rare earth manganites possessing hexagonal structure [7], [46], [52] and general composition $RMnO_3$ where R = Y, Sc, Ho, Er, Lu, Tm and Yb with the most studied being $YMnO_3$. These are good ferroelectrics at room-temperature and antiferromagnetic at low temperatures. For a number of rare earth elements R = Dy, Tb, Nd, Pr and La the

structure becomes orthorhombic and is not ferroelectric at room-temperature any more since it becomes centrosymmetric.

3. Boracites with the chemical formula $Me_3B_7O_{13}X$, where Me is a 2+ charged ion (M = Cr, Mn, Fe, Co, Cu, Ni) and X=Cl, Br, I [7], [46]. These compounds are often ferroelectrics at room-temperature and antiferromagnetic sometimes displaying weak ferromagnetic behaviour at temperatures below 100 K. Probably the most important one is the nickel-iodine boracite $Ni_3B_7O_{13}I$ where magnetoelectric switching was observed in crystals through application of magnetic fields [53].

4. Flourides with formula $BaMeF_4$ where Me = Mn, Fe, Co, Ni, Mg, Zn [7], [46]. These have orthorhombic structures at higher temperatures and display pyro- or ferroelectric properties and antiferromagnetism at temperatures below 70 K.

As mentioned previously, truly ME multiferroics are very rare. However, materials which exhibit ME coupling do not need to be multiferroic at the same time and vice versa. A well-known example is Cr_2O_3 which is antiferromagnetic but only electrically polarizable and not ferroelectric [54]. On the other hand there also exist materials which are multiferroic but do not exhibit ME coupling. These circumstances can be understood by considering Figure 16 which illustrates schematically a classification of all insulating oxides with the subclasses of electrically and magnetically polarizable, ferroelectric, ferro- or ferrimagnetic as well as magnetoelectric materials.
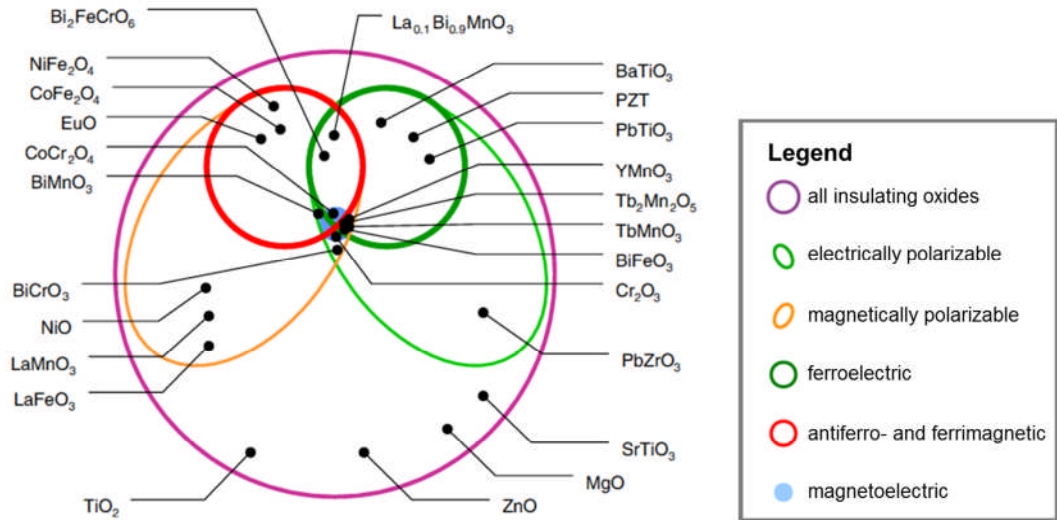
Figure 16 Schematic illustration of the classification of electrically and magnetically polarizable and ordered insulating oxides. ME materials overlap with multiferroic materials but also contain materials which are not ferroic (adapted from [55]).

1.6.5 Composite multiferroics

As mentioned previously, another general class of multiferroics are composites or heterostructures. This class of multiferroics has become increasingly popular within the last two decades particularly in the field of thin-films where new growth techniques have enabled substantial new research [56]–[58].

The largest number of composites are probably sandwich-type or multilayered heterostructures. With this class of materials, ME coupling coefficients could be increased drastically for the first time in almost 30 years in the beginning of the millennium [7] using laminated Terfenol-D/PZT heterostructures [59].

Another very important example of multiferroic heterostructures, is the system $BaTiO_3$-$CoFe_2O_4$. Zheng et al. were able to grow epitaxial and self-assembled hexagonal $CoFe_2O_4$ nanopillars in a matrix of $BaTiO_3$ on a $SrTiO_3$ substrate [60] which showed strong ME coupling.

These multiferroic heterostructures sparked significant new research especially in application driven research, since they combine large coupling coefficients with high ferroelectric and magnetic Curie temperatures.

An important example of possible applications of magnetoelectric materials are sensors of magnetic fields. For this purpose, Lage et al. developed cantilever systems consisting of piezoelectric AlN, coated with a series of exchanged biased magnetic layers. When these cantilevers are excited at resonance, they are extremely sensitive to AC magnetic fields due to the magnetostricitve layer [2].

It is also possible to form heterostructures of single-phase multiferroics and e.g. magnetic materials. This is the case for a thin-film microstructured system where the magnetization of a ferromagnetic layer of $Co_{0.9}Fe_{0.1}$ which is deposited on top of an epitaxial $BiFeO_3$ thin-film, can be switched by 180° by reversing the polarization of the $BiFeO_3$ film using a voltage. In this way a voltage driven spin valve becomes possible [61], which is operated current free and thus, is much less energy consuming than current technologies. A patented technique for ME memory based on voltage driven switching of magnetization in the layered MF system $(Co/Pt)_nCr_2O_3$ has been already developed which is comparable to the above system [4].

1.6.6 **Magnitude of the magnetoelectric effect**

As mentioned in Section 1.6.3, a crucial drawback of single-phase multiferroics is that they usually exhibit only weak magnetic properties at low temperature. Due to the limitation set by the low magnetic permeability (see Equation 1-11), single-phase multiferroics usually only display weak ME coupling [7].

Coupling-coefficients reported for these materials are typically between 10^{-12} – 10^{-10} s/m [7], [58], [62]–[64], which is relatively low and in combination with the low temperatures at which magnetism appears, seems to make them unsuitable for practical devices.

In contrast, state of the art composite multiferroics exhibit much higher coupling-coefficients than single-phase materials and are of the order of 10^{-8} – 10^{-6} s/m [2], [7], [65], [66] at room-temperature. However, we need to mention that some care should be taken when comparing the linear ME response of single-phase and composite materials. In order to permit such an analogy the ME coupling-coefficient for composites is usually defined as an AC effect with low AC fields and frequencies between 100 Hz and 1 MHz

[7] in order to stay in a linear response regime. In contrast, the linear ME response in single-phase multiferroics is usually a static effect. Historically, for composites the ME voltage coefficient was usually measured with the so-called direct method (see Equation 1-9).

Still, composites seem to be so far much more suitable candidates for devices as compared to single-phase multiferroics. Nevertheless, a single-phase material with large ME coupling at room-temperature, would be preferable compared to ME composites for example because of the reduced production effort.

Recently, using piezoresponse force-microscopy (PFM) in combination with magnetic fields, it was shown that strong ME coupling can exist in single-phase multiferroics at room-temperature in the lead containing perovskite $(PbZr_{0.53}Ti_{0.47}O_3)_{0.6}$-$(PbFe_{0.5}Ta_{0.5}O_3)_{0.4}$ [67], [68]. This result sheds new light on single-phase multiferroics also for applications.

1.6.7 Ferrimagnetic ferroelectrics

As mentioned in Section 1.6.1 single-phase multiferroics only display low ME coupling due to the weak magnetism. However, one possibility to overcome this limitation e.g. in $BiFeO_3$, is to introduce paramagnetic ions (Me) with a different number of unpaired electrons as compared to Fe^{3+}. Antiferromagnetic coupling of these Me^{n+} ions with Fe^{3+} results in ferrimagnetism which is characterized by an incomplete compensation of antiparallel magnetic spins and thus causes much larger magnetic susceptibility than WFM (see Section 1.5.2). The largest magnetic moment per formula unit would be achieved for the composition $BiFe_{1/2}Me_{1/2}O_3$ and for a perfect chemical order of Fe- and Me-ions so as not to create Fe-Fe or Me-Me pairs. These ions should however, have a similar size and the same oxidation state as Fe^{3+}-ions in order to occupy the same lattice site as Fe^{3+}. Suitable candidates for this 'ferrimagnetic strategy' are e.g. Cr^{3+}, Mn^{3+} and Co^{3+}-ions. $BiFe_{1/2}Cr_{1/2}O_3$ has been prepared both as ceramic [69] and epitaxial thin-film [70]–[72] where the latter showed good chemical order and ferrimagnetism. However, these thin-films exhibit poor dielectric properties and might not be truly ferroelectric [46]. Another compound which is

potentially ferrimagnetic is $BiFe_{1/2}Co_{1/2}O_3$. It will be discussed in greater detail in Section 1.7.2.

For the sake of completeness it is mentioned that there also exist materials which are ferromagnetic and ferrielectric and thus complementary to the above. One is the recently reported $DyMn_2O_5$ [73].

1.7 Materials

1.7.1 $BiFeO_3$

Certainly the most intensely investigated multiferroic material is $BiFeO_3$ [7], [74], [75]. It has a rhombohedral structure with space group R3c at room-temperature and has an extremely high ferroelectric Curie temperature, $T_C \approx$ 1100 K. Furthermore, it is weakly ferromagnetic at room-temperature in thin-film form, whereas for bulk single crystals the weak ferromagnetism is supressed by a cycloidal spin-superstructure [33] (see Section 1.5.3). Its extremely high ferroelectric Curie and Néel Temperature $T_N \approx 643$ K make it an ideal multiferroic. Therefore, $BiFeO_3$ has been the subject of extensive research, also because it is non-toxic unlike the vast majority of lead containing ferroelectric materials used in devices to date and because its constituents are cheap and abundant. In recent years, tremendous effort has been spent on enhancing its multiferroic properties by modifying it structurally or chemically.

1.7.2 $BiFe_{1-x}Co_xO_3$

So far, not much literature is available on Co-substituted $BiFeO_3$ in literature. However, Sosnowska et al. [76] confirmed Fe-Co ferrimagnetism in $BiFe_{0.8}Co_{0.2}O_3$ using ultra-high-resolution neutron diffraction which is in line with other reports of greatly increased magnetization in Co substituted $BiFeO_3$ compounds as compared to pure $BiFeO_3$ [77]–[79]. However, to participate in the antiferromagnetic order the free electrons of Co^{3+}-ions need to be in a high-spin state since there are no unpaired electrons if Co^{3+} is in a low-spin state which is usually the case. However, recently it was shown that Co^{3+}-ions are in high-spin configuration in $BiCoO_3$ [80], [81] which also seems to be the case in Co substituted $BiFeO_3$ [76], [79].

Furthermore, dielectric properties such as resistivity are also improved by the Co-substitution [79], [82]. Therefore this component was identified as ideal for further investigations in this project.

1.7.3 $Bi_{1/2}K_{1/2}TiO_3$

$Bi_{1/2}K_{1/2}TiO_3$ (BKT) is a tetragonally distorted ferroelectric with space group P4mm. For a lead-free ferroelectric it has a surprisingly high Curie temperature. Razumovskaya et al. [83] reported a T_C of 380°C for conventionally sintered ceramics while Hiruma et al. [84] reported a T_C of 437°C for hot pressed pellets. It was found, that the FE long-range order can be reduced by adding only small amounts of $LiNbO_3$ (($LiNbO_3)_x$-$(Bi_{1/2}K_{1/2}TiO_3)_{1-x}$ x = 0.02) [85] to the system and the material, hence, becomes relaxor FE due to quenched ionic charge disorder [86] similarly as, e.g., in the archetypical relaxor $PbMg_{1/3}Nb_{2/3}O_3$ [22].

1.7.4 $(BiFeO_3)_x$-$(Bi_{1/2}K_{1/2}TiO_3)_{1-x}$

The system $(BiFeO_3)_x$-$(Bi_{1/2}K_{1/2}TiO_3)_{1-x}$ has been the subject of extensive investigation carried out by J. Bennett at the electroceramics group in Leeds [87]. The main results of this work are summarized below:

A broad MPB between rhombohedral and pseudo-cubic phases was found at x = 0.4 and supposedly an additional phase boundary between pseudocubic and tetragonal at x = 0.1, which was, however less obvious as the one at x = 0.4. Matsuo and Ozaki et al. also found a pseudo-cubic phase in the BF-BKT system and proposed that it consists of a mixture of non-polar cubic and polar rhombohedral nanoregions which they observed using TEM [86], [88]. These nanoregions apparently yield an average pseudo-cubic crystal structure on a macroscopic level as observed by X-ray diffraction. The presence of PNR suggests that the material is a relaxor ferroelectric similar to solid solutions of BKT and $LiNbO_3$ [85]. This is supported by the fact that a very low or no negative strain is observed for compositions with x = 0.4 and below from strain vs. electric field (x-E) measurements in contrast to BF richer compositions. For compositions with very high BF content (x = 0.8 and higher) also very little negative strain was found which is, however, attributed to high coercivity and conductivity. A low negative strain is indicative of electrostriction dominated electromechanical response

and therefore relaxor behaviour. In addition, a strong frequency dependence of the x-E behaviour which is typical of relaxor FE, was found for the pseudo-cubic compositions. Furthermore, a large discrepancy between direct and converse piezoelectric coefficients which were measured using Berlincourt and x-E loops respectively, was observed for pseudo-cubic compositions. This was also attributed to the relaxor behaviour and the presence of PNR which was further confirmed by positive-up-negative-down (PUND) measurements which measure a material's switchable polarization. It was found that for the BF rich composition with $x = 0.6$ the switchable polarization was comparably high as for other conventional ferroelectrics. In contrast, for $x = 0.4$ a very low switchable polarization was found which was attributed to a low FE long range order which is further indication of the material's relaxor behaviour. Leakage current measurements confirmed that the low switchable polarization for $x = 0.4$ is not due to increased conductivity. All investigated compositions $x = 0.6$, 0.5 and 0.4, have similar low conductivity typical of good electroceramics.

The findings by Bennett et al. and other authors are summarized in Figure 17.
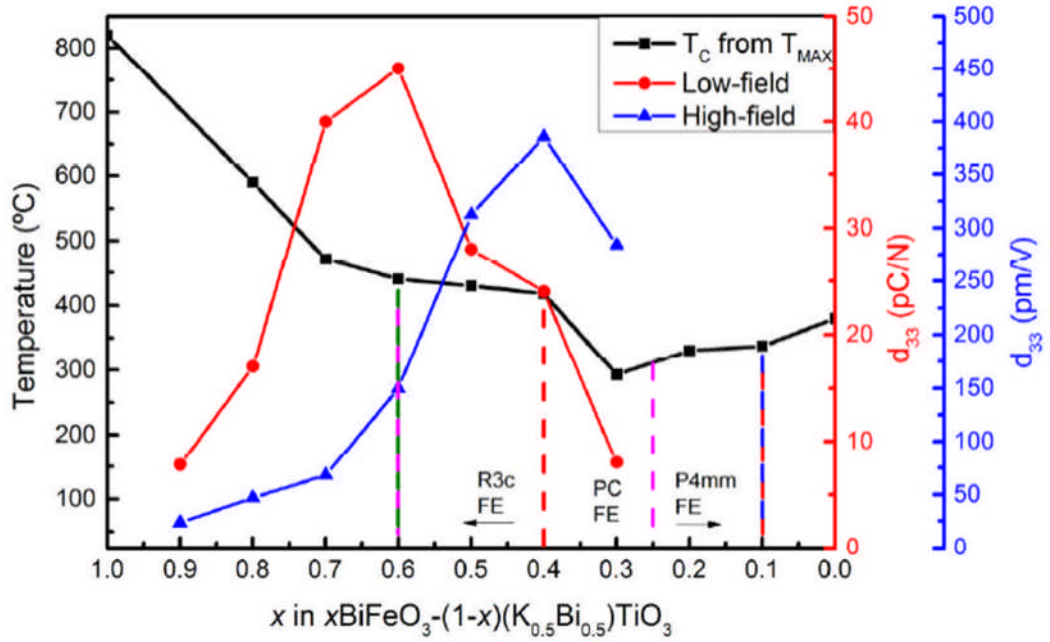
Figure 17 Phase diagram of BF-BKT as found by J. Bennett illustrating the Curie temperature, direct (low field) and converse (high field) piezoelectric coefficients [87]. The dashed lines represent phase boundaries between rhombohedral (R3c) and pseudo-cubic (PC) phase found by Matsuo [86] (green), Morozov [89] (pink) and Bennett (red) while the boundary at x = 0.1 represents the boundary between PC and tetragonal (P4mm) phase found by Bennett (red) and Kim [90] (blue).

J. Bennett also investigated BF-BKT compositions with PFM and observed a dipolar structure, where ferroelectric clusters (SPNR) (might be also referred to as static PNR) are distributed within a polar matrix with low piezoresponse which presumably incorporates PNR. He found that the concentration of SPNR decreased with increasing BKT content which is in line with the increasing relaxor properties of BKT rich compositions. In other words, the ergodicity (see Section 1.7.4) increases with the BKT content in the pseudo-cubic phases while non-ergodicity increases with BF content.

Bennett et al. [91] also investigated magnetic properties of these materials and found antiferromagnetic order using neutron diffraction at room-temperature for compositions with x = 0.8, 0.7 and 0.6 similar as for $BiFeO_3$. As expected, the antiferromagnetic peak at approximately 4.6 Å decreased in intensity with decreasing BF content.

1.7.5 $(PbZr_{0.52}Ti_{0.48}O_3)_x$-$(PbFe_{2/3}W_{1/3}O_3)_{1-x}$

In the past few years, a number of articles were published on magnetoelectric coupling and multiferroic behaviour in the perovskite solid solution $(PbZr_{0.52}Ti_{0.48}O_3)_{1-x}$-$(PbFe_{2/3}W_{1/3}O_3)_x$ (PZT-PFW) [92]–[94]. This composition is a solid solution of the well-known PZT with strong piezo- and ferroelectric properties, and the relaxor ferroelectric and antiferromagnetic PFW [95]. PZT-PFW has been proposed to be a good candidate for single-phase multiferroics [92]. Thin-film PZT-PFW, with compositions of $x = 0.2$, 0.3 and 0.4 were reported to have tetragonal structures with large dielectric polarization and modest magnetization as for weak ferromagnetic materials. For $x = 0.2$ Kumar et al. [96] reported switching from a ferroelectric state with high polarization to a linear lossy dielectric with no polarization via a magnetic field of 0.5 T and hence proposed that the material might be used in a three state logic device with $-P_r$, 0, $-P_r$ states. However, Kempa et al. [93] could not confirm such behaviour in bulk ceramic samples with magnetic fields up to 3.2 T while Pajic et al. [94] only found linear magnetic behaviour without hysteresis down to 5 K for compositions $x \geq 0.25$. However, they found a blocking behaviour and signatures of magnetic nanoregions (MNR) for all compositions $x \leq 0.7$ with strongest blocking for $x = 0.63$. Futhermore, analysis of AC susceptibility measurements, indicated spin-glass behaviour of compositions with $x \leq 0.7$.

Thus, results in literature are therefore somewhat inconclusive regarding the strong ME effect reported in the thin-films.

1.7.6 $LiNbO_3$

$LiNbO_3$ is another material where ferroelectricity is due to an off-centred ion. It has the point group R3c and is related to the perovskite crystal structure but has a considerably larger unit cell. In contrast to perovskites, polarization can only occur along the crystallographic c-axis and can therefore only form 180° domains. It has an extremely high Curie temperature of approximately 1210°C [97] and is an important material in telecommunications (*e.g.* by using 'surface acoustic waves'), but also in non-linear optics and high frequency or high temperature transducers. Large lithium niobate single crystals can be grown along the crystallographic c-axis (or Z-axis) by a

Czochralski process and cut into thin wafers. Usually crystals have c-facets which are also often referred to as Z-facets. Especially important in non-linear optics is periodically poled lithium niobate (PPLN) which is single crystalline lithium niobate that is periodically poled with electrodes that are applied by a lithography process. PPLN comprises of stripe-shaped domains that usually have a width of 5-35 μm and have polarization in +c and -c (+Z- and −Z) direction. The d_{33} coefficient is parallel to the Z-direction and orthogonal to the Z-face. PPLN is represented schematically in Figure 18.
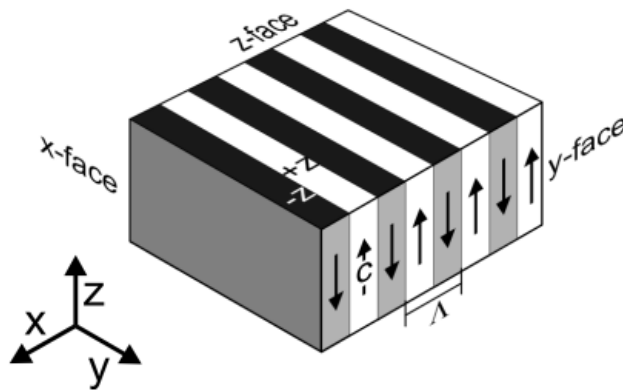
Figure 18 Schematic representation of PPLN crystal showing crystal axes and polarization directions.

2 Methods

2.1 Chapter overview

This chapter will give an overview of the experimental methods used for sample preparation and characterisation. General theoretical aspects and set-up of measurement techniques will be given. Specific experimental procedures and experimental details of experiments will be given in separate subsections.

2.2 Sample preparation

2.2.1 Preparation of oxide powders

Preparation of dielectric oxide ceramics is a complex process, which can be extremely sensitive even to slight changes of parameters which can cause dramatic changes of properties, e.g. due to the concentration of impurities or vacancies. Thus a well-established process of sample preparation is highly recommendable, where parameters are controlled adequately. Conventional solid state reaction from binary metal oxide powders has been used for synthesis of perovskite powders for many years in the group of Prof. Bell in Leeds and the process is well-understood as outlined in previous work [91], [98]–[101].

All perovskite powders for compositions investigated in this thesis were prepared using the following procedure. As starting materials for synthesis of $(BiFe_{1-x}Co_xO_3)_{0.4}$-$(K_{1/2}Bi_{1/2}TiO_3)_{0.6}$, Bi_2O_3 (99.9%), Fe_2O_3 (99+%), TiO_2 (99.9%), CoO (99+%) and K_2CO_3 (99+%) while additionally PbO (99.9%), WO_3 (99.9%) and ZrO_2 (99.9%) (Sigma Aldrich) were used for preparation of $(PbZr_{0.52}Ti_{0.48}O_3)_x$-$(PbFe_{2/3}W_{1/3}O_3)_{1-x}$ (x = 0.8, 0.7, 0.6) samples. Powders were first dried in an oven at 130 °C to remove any moisture in order to allow accurate weighing. These reagent powders were then suspended in isopropanol and (attrition) milled in a Dyno-mill KDL Type-A (Willy A. Bachofen, Switzerland) with yttria-stabilised zirconia (YSZ) beads (Tosoh, Japan) for 30 minutes. After milling, powders were separated from the

solvent using distillation at low temperatures under reduced pressure. Dry powders were sieved through a 300 μm mesh before calcination at 800°C for 4 hours in an alumina crucible which was sealed loosely with an alumina tile. The resultant pre-reacted perovskite powder was again sieved and attrition milled where 1 wt% of Glascol HA-40 binder (Allied Colloids, UK) was added to the solvent. After repeated drying, the powder was again sieved in a final step.

2.2.2 **Sintering of ceramics**

The pre-reacted powder was pressed into pellets using a uniaxial press followed by cold isostatic pressing at 200 MPa for approximately 15 minutes. For sintering, these pressed pellets were then placed in a bed of the pre-reacted powder inside an alumina crucible closed with an alumina tile. On one hand, the powder bed prevents contamination of pellets during sintering but also acts as a source of volatile elements which are Bi and K in this case. An atmosphere of these elements is created inside the closed crucible which reduces loss of volatile elements in the pellets. Since the powder has a much larger surface than the pellets, volatile elements mainly evaporate from it and not from the pressed compact pellets.

Sintering was always followed the temperature program depicted in Figure 19 with the exception of the sintering temperature.
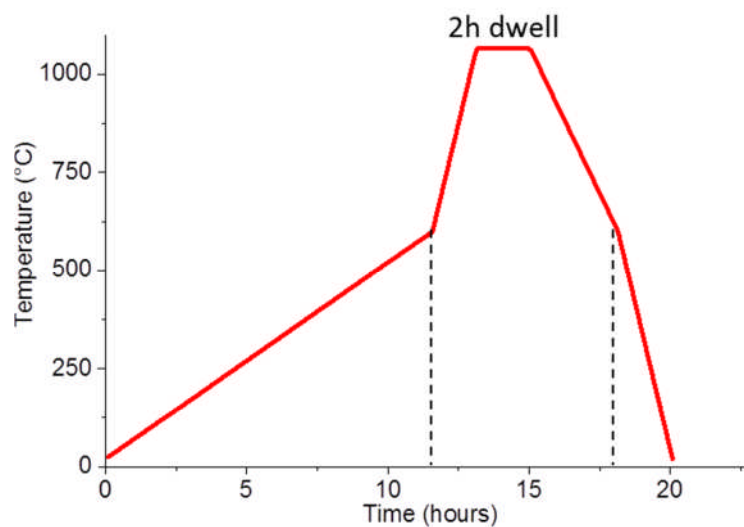
Figure 19 Temperature regime used for sintering of pellets.

The above temperature regime was chosen to allow for slow heating of pellets and slow burning of the binder to avoid large porosity or decomposition of ceramic pellets due to rapid release of gaseous burning products. Cooling is also slowed down to avoid cracking of pellets due to mechanical tension.

BFC-BKT ceramics were sintered at a temperature of 1065 °C, while PZT-PFW ceramics were sintered at 1200-1150 °C.

2.2.3 Grinding and polishing of surfaces

Since sintered pellets always have a surface layer, which is not representative of the bulk material, this layer needs to be removed by grinding before any further investigations such as electrical characterisation are carried out. For grinding, relatively coarse SiC or diamond paper was used with grit size P 800.

Other characterisation techniques such as AFM or SEM require surfaces to be polished for a surface roughness below 100 nm. Especially for PFM, which is a relatively surface sensitive technique, it is important that sample surfaces are structurally not distorted as compared to the bulk in order to image the dipolar structure as similar as possible to the bulk structure. Therefore, it is necessary that the sample surface is not structurally damaged. In order to achieve this, a multi-step polishing route was used, where the particle size of an abrasive was gradually reduced in consecutive steps. In this way, damages induced by a previous grinding or polishing step were removed by the consecutive, while the removed layer gets thinner at each step. For this, various polishing-cloths (TexMet P®, TriDent®, ChemoMet®, Buehler, Germany) were used, in combination with diamond abrasive-liquids where the diamond particle-size was gradually reduced for consecutive steps (9 μm, 3 μm, 1 μm, also Buehler). Finally, in the last and most important step, only very little material is removed which also involves a very mild chemical etching which removes structurally distorted material and reveals the grain structure. For this step 200 nm sized colloidal silica particles were used.

2.3 Structural and chemical characterisation

2.3.1 Atomic force microscopy (AFM)

Since its invention by Binnig, Quate and Gerber in 1986 [102], atomic force microscopy has become an invaluable tool in today's science due to its extremely high resolution especially in vertical direction in combination with exceptional versatility in probing local properties which manifests itself in a multitude of different techniques. Many of those properties such as local stiffness, friction, adhesion and electric conductivity can usually not be measured with other microscopy techniques utilizing electromagnetic radiation or particles. The underlying principle of AFM is that of a record player, where a thin needle moves over a surface and is deflected due to the contact to the surface. Of course there are prime differences between the way an AFM and a record player work. First of all, the tip that is used in AFM is extremely small due to micro processing techniques and the tip's apex is usually only approximately 20 nm wide. The miniature tip is attached to a flexible beam (cantilever), which is deflected through interactions between tip and surface, while it is scanned over the surface. The scanning is achieved using piezoelectric actuators for the x-, y- and z-directions, which usually have an accuracy in the range of nanometres. Here, it is irrelevant whether the tip is scanned while the sample surface position is kept constant or vice versa.   The vertical deflection or torsional movements of the cantilever are usually detected by a laser-beam which is reflected from the back-side of the cantilever onto a four-quadrant photodiode. Figure 20 shows a schematic set-up of an AFM.
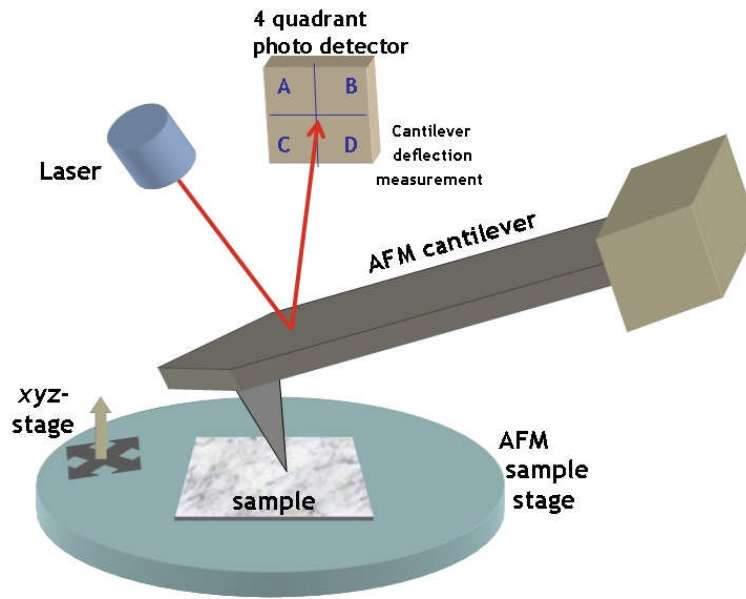
Figure 20 Schematic illustration of an atomic force microscope (AFM) with cantilever, laser diode and four-quadrant photodiode [103].

Vertical deflection of the cantilever results in vertical movement of the laser spot on the photodiode, which is detected using the relative measured intensities between the upper (A+B) and lower (C+D) quadrants. In this way, a height value is obtained as a function of the lateral position on a sample. These information are used to assemble a topographic image of the scanned surface. Similarly, torsional movement of the cantilever results in sideways motion of the laser spot which is detected using the relative measured intensities between quadrants on left (A+C) and right (B+D) side.

An alternative method for measuring cantilever deflections and thus height values is interferometry, which will not be covered in greater detail here.

There exist several different operation modes for AFM. Usually AFM is operated in a constant-force mode which means that the force between tip and sample are kept constant. This is achieved by a feedback loop which actively compensates cantilever deflections by moving the tip in z-direction, thus keeping the laser spot in the same vertical position on the photodiode. In this way, large forces which could potentially damage tip or surface are avoided. Furthermore, 'crashes' between tip and large surface features can be prevented. For best imaging performance, it is important that the parameters that control the sensitivity of the feedback loop are set correctly.

In contrast, in constant-height mode cantilever deflections are not compensated and are used as height signal. This mode is, however, not widely used. In reality, a perfect constant force mode can never be achieved, since cantilever deformations will always occur.

In addition to the above operation modes, AFM is usually operated in one of the following three imaging modes:

- Contact mode: Here the tip is in permanent contact with the surface (contact regime) and repulsive forces between tip and sample are dominant. Lateral signals due to cantilever torsion can be detected, e.g. to measure sample friction. However, due to permanent contact, tip and sample are readily worn or damaged, which makes it unsuitable for soft materials. This mode is used, e.g., in PFM.

- Non-contact mode: The cantilever is mechanically excited to oscillate close to its resonance frequency and scanned over the surface in close proximity. Due to long range interactions between tip and sample, the phase of the oscillation changes, which is used as a measure for interaction between tip and surface. This mode offers advantages such as lower tip wear and sample damage which comes, however, at the expense of resolution. It is also not possible to detect a lateral or friction signal. A modified non-contact mode is used in MFM.

- Intermittent contact: This mode is also-called 'tapping mode' and is probably most widely used for imaging purposes. It is similar to non-contact mode with the difference that the cantilever touches the surface during oscillation. Here, the amplitude of oscillation is usually kept constant via height adjustment. It offers high resolution and low tip wear and surface damage.

2.3.2 Scanning electron microscopy with energy dispersive *X*-ray spectroscopy (SEM-EDX)

SEM is a widely used microscopy technique to obtain a high resolution micrograph of a sample's surface topography by scanning a focused beam of electrons across a sample in a raster fashion.

In general, an SEM uses electrons instead of visible light to achieve high resolution. As known from quantum mechanics, particles have wave character and their wavelength is connected to the particles' momentum according to de Broglie's law. Accordingly, electrons with a large velocity, e.g., due to a high acceleration voltage have very short wavelengths in the sub nanometre range, while visible light has wavelengths in the range of 400-700 nm. According to the Rayleigh criterion the limit of lateral resolution is approximately half of the wavelength of the electromagnetic radiation used for imaging. Hence, it becomes obvious that high energy electrons are suitable to achieve much higher resolution than visible light microscopy.

An SEM mainly consists of an electron emitter, electron lenses and detectors. The electron emitter might be a tungsten filament, which thermionically emits electrons, or a field emission gun made of LaB_6 which allows for higher resolution through smaller spot sizes. Emitted electrons are usually accelerated by voltages in the range of 0.2-40 kV. Those electrons are focused by one or more condenser lenses to a beam with a spot size typically in the range of a few nanometres, which is scanned across a sample in a raster fashion by scanning coils or deflector plates.

When the electrons interact with the sample, several processes can occur, which include emission of high-energy electrons due to elastic scattering, emission of secondary electrons due to inelastic scattering and emission of electromagnetic radiation. The resulting emissions can each be detected by specialized detectors corresponding to different imaging modes and spectroscopy methods. The set-up of an SEM is illustrated schematically in Figure 21.
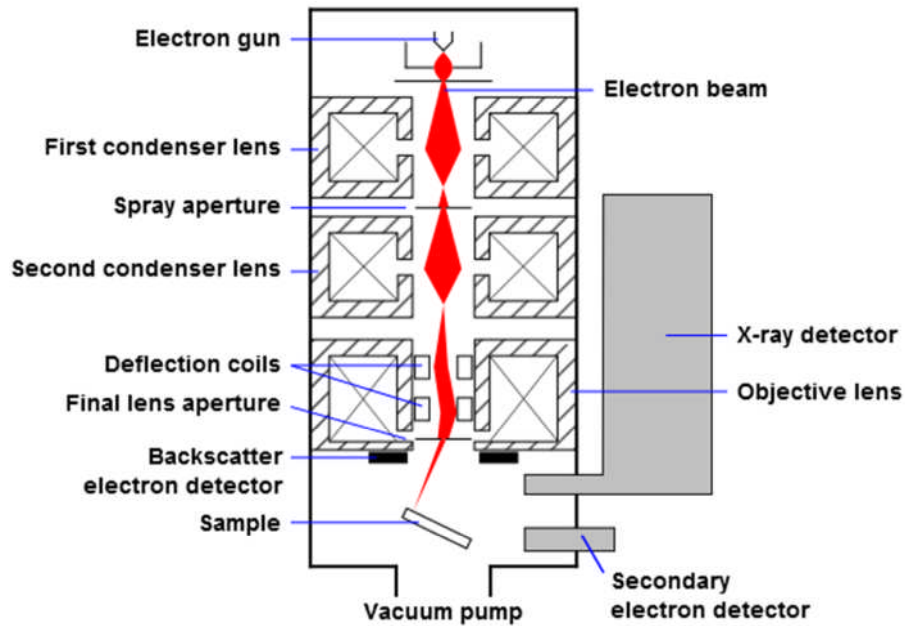
Figure 21 Schematic illustration of an SEM showing electron gun, condenser lenses, deflection coils and detectors for secondary and backscattered electrons as well as for *X*-rays [104].

The most common imaging mode uses the collection of secondary electrons. The intensity of secondary electrons as a function of scanning position yields an image, which reveals the sample's topography. Samples should be conductive or covered with a film of conductive material for this mode to avoid charging effects.

Another imaging mode is the collection of high energy back scattered electrons (BSE). Since electrons are backscattered much more effectively by heavy elements (high atomic number) than by light elements (low atomic number), heavy elements appear brighter in a BSE image, which results in an atomic number-contrast (Z-contrast). Furthermore, it is much less prone to charging and thus can be usually applied to insulating samples without need for deposition of a conductive film.

A commonly used spectroscopy method which is used in junction with SEM is energy dispersive *X*-ray spectroscopy (EDX). Here, *X*-rays emitted from the sample due to inelastic scattering of electrons are detected which have specific energies corresponding to the difference of atomic energy levels depending on the atomic number. Hence, the energy of emitted *X*-rays are element specific and can be used for compositional analysis of a sample.

Transitions from atomic energy levels to K-shell levels result in *X*-rays belonging to the K-series, whereas transitions to L-shell levels correspond to the L-series and so on. Furthermore, *X*-rays which correspond to a transition from one shell to the shell which is next lower in energy are termed α, whereas *X*-rays corresponding to shells which are two levels lower are termed β and so on. For example, a transition from L to K shell corresponds to Kα, while a transition from N to L shell corresponds to Lβ radiation.

Many EDX spectra can be obtained with relatively high lateral resolution by scanning a small electron beam over larger areas to obtain maps of elemental composition in order to reveal compositional inhomogeneity with high lateral resolution (below 1 μm).

2.3.3 **Time-of-flight secondary ion mass spectrometry (TOF-SIMS)**

Secondary ion mass spectrometry (SIMS) is a technique which is effectively similar to SEM with EDX in that it is able to spatially resolve the chemical composition of a sample. However, there are fundamental differences between the two techniques considering the principle. While in EDX, the wavelength of *X*-rays being emitted from a sample is analysed to gain information about its composition, in SIMS, information is obtained through the mass of ions coming from a sample surface. Atoms are ablated from a sample surface by ion bombardment using a pulsed ion beam. These are partly ionized by the bombardment process and subsequently extracted and submitted to mass analysis through a time-of-flight (TOF) mass spectrometer via transport optics as illustrated in Figure 22.
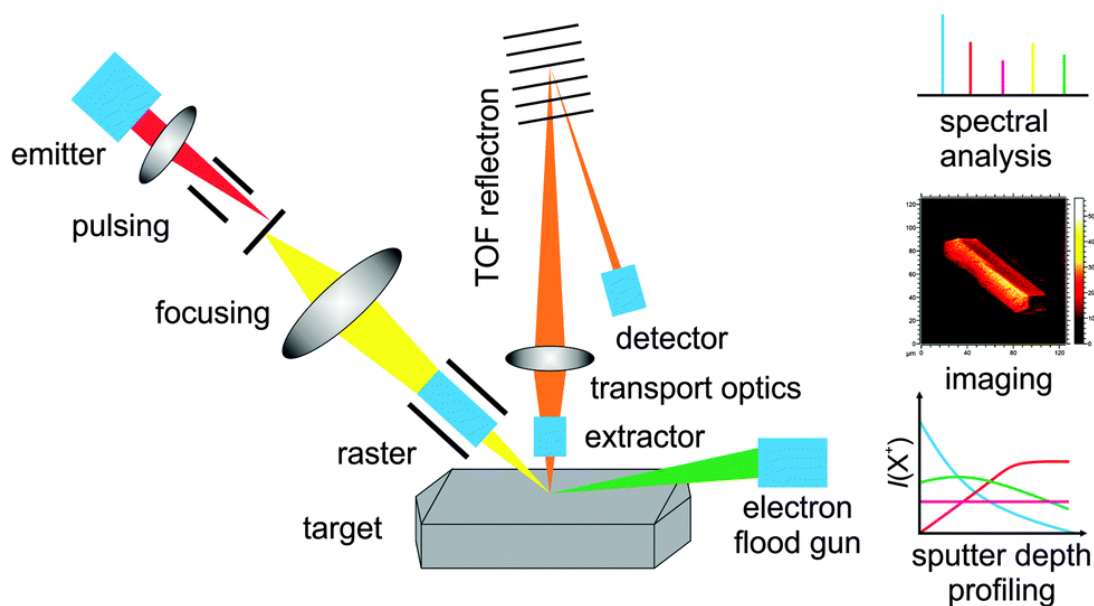
Figure 22 Schematic illustration of a TOF-SIMS. A focused and pulsed beam of ions is generated from an emitter and rastered across a sample. Secondary ions being ablated from the sample are analysed via a time-of-flight mass spectrometer. Chemical information can be gained via the mass of ions which can be assigned to elements via isotope patterns. Spatially resolved spectra can be used for imaging, while recording consequent mass spectra after sputtering steps can be used to obtain depth profile measurements [105].

Additionally, secondary electrons can be also detected for imaging purposes. The obtained mass spectra are analysed by assigning elements to peaks using element specific isotope patterns. Not only single ions but cluster- or molecular-ions are detected in SIMS, which can yield additional information. To obtain a spatial distribution map of certain peaks or elements, many spectra are recorded in a raster fashion. The achievable resolution depends on the diameter of the ion beam. However, it should be noted that spatial resolution comes at the expense of mass resolution and vice-versa, since an ion-beam with small diameter results in a longer duration of bombardment as compared to a beam with large diameter when the pulse duration of the beam is kept constant. The duration of bombardment in turn is directly connected to the achievable mass resolution. The information gained is usually very surface sensitive, since the penetration depth of ions is only in the range of approximately 1-2 nm. Furthermore, depth profiles can be recorded consisting of consecutive mass spectra, being recorded each after an additional sputtering step to expose deeper lying layers of a sample.

The most important advantage of TOF-SIMS over other techniques like SEM-EDX, is its extremely high sensitivity which enables detection of elements in the ppm range and below due to the electron multiplier principle of the detector. Furthermore, the small beam sizes of state-of-the-art instruments, allow high lateral resolution down to approximately 50 nm. It is widely used for the spatially resolved determination of dopant concentrations in semiconductors. However, peaks corresponding to different elements can usually not be correlated to each other or converted to elemental composition, due to the different sensititivy factors of each element. These are due to the different ionization probabilities of different elements being mainly responsible for the large intensity differences for different elements observed in SIMS. All alkali metals, have, for example, ionization probabilities close to one, whereas noble elements such as Ag have a probability which is several order of magnitude lower. Therefore, only relative intensities for a given element can be compared e.g. for different sample areas [106].

2.3.4 *X*-ray diffractometry (XRD)

The most widely used technique for crystal structure determination is XRD. As the name suggests, it is based on diffraction of *X*-rays by atoms of a crystalline material. *X*-rays are suitable for this purpose since their wavelength is in the same order as interatomic distances in solids given by the size of atoms in the order of 0.1 nm. Due to constructive and destructive interference of *X*-rays scattered by atoms of a crystal, a diffraction pattern forms similar as for diffraction of visible light by an optical grating. In a crystal, where atoms are arranged regularly, lattice planes can be defined, which are separated by the interplanar distance *d*. Constructive interference occurs which results in diffraction maxima or peaks, when *X*-rays fulfil the Bragg condition which connects *d* with the scattering angle θ and the wavelength λ of the *X*-rays:

$$2d\sin(\theta) = n\lambda,$$

<div align="right">Equation 2-1</div>

where n is a positive integer. When the Bragg condition is met, scattered waves remain in phase since the path length of each wave is equal to an

integer multiple of the wavelength which leads to constructive interference. This principle is illustrated in Figure 23.
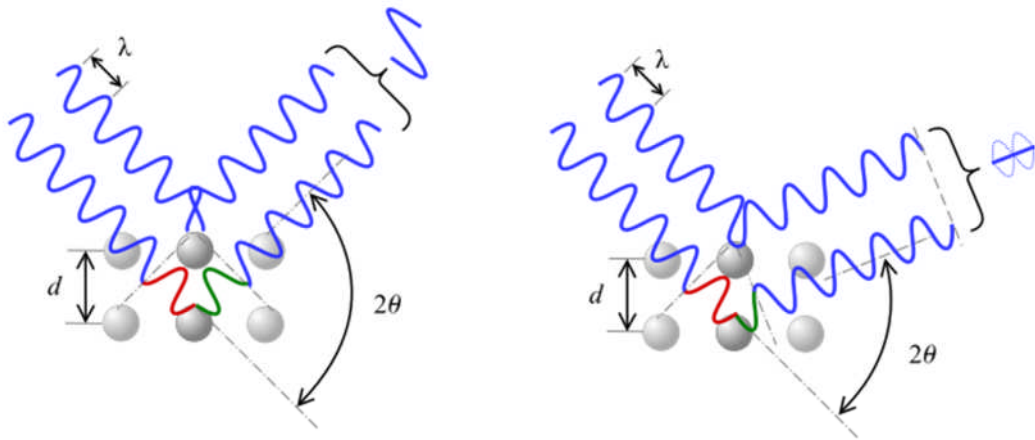
Figure 23 Diffraction of *X*-rays of given wavelength λ by a crystal. An angle for which the Bragg condition is fulfilled, results in constructive interference by atoms belonging to two lattice planes with interplanar distance *d* (left). For the angle shown in the right image, the condition is not fulfilled and interference is destructive [107].

As a result, a crystal effectively acts as a mirror for *X*-rays, but only under certain angles where the Bragg condition is met.

While diffraction on large single crystals results in diffraction patterns with individual peaks which allow elucidation of the crystal symmetry and structure, diffraction on polycrystalline materials, where crystallites are oriented randomly, results in diffraction patterns consisting of concentric rings. These patterns, which are referred to as powder diffraction pattern, contain less information than single crystal patterns and are usually displayed in so-called *X*-ray diffractograms, where intensity is plotted *vs.* 2θ.

2.3.5 Experimental details

All AFM experiments were carried out on a 5420 AFM by Agilent Technologies (now Keysight technologies, Santa Clara, California, USA) with the MAC Mode III extension except where explicitly stated. Polished samples (see Section 2.2.3) were used for imaging.

Furthermore, all SEM images were recorded on an EVO MA15 by Carl Zeiss (Oberkochen, Germany) in back-scatter electron (BSE) imaging mode with 20 kV acceleration voltage. EDX spectra were acquired using an AZtecEnergy EDX system (Oxford Instruments, Abingdon, United Kingdom). Polished and uncoated samples as for PFM measurements (see Section 2.2.3) were used for imaging which were attached to the sample stage using adhesive pads. The edges and back side of ceramics were electrically connected to the sample stage using black carbon conductive glue.

X-ray diffraction, was conducted on powder of sintered and crushed ceramic pellets, using a PANalytical X'Pert Diffractometer (Phillips, The Netherlands) with a theta-theta goniometer. Cu Kα radiation was used with a Ni foil monochromator. Scanning times were relatively long (approximately 40 minutes) with small step size of 0.033° and scan ranges from 14° to 70° 2θ or larger.

Diffraction peaks were indexed using the PANalytical Highscore Plus software. Furthermore, peaks due to Cu Kβ radiation were removed with the same software.

TOF-SIMS measurements were carried out on a TOF.SIMS 5 by ION-TOF (Münster, Germany) using a beam of Bi ions in positive mode.

2.4 Dielectric characterisation

2.4.1 Polarization *vs.* electric field (*P-E*)

Polarization *vs.* electric field measurements are essential for characterisation of ferroelectric materials to measure the hysteretic *P-E* behaviour, '*P-E*-loop', as outlined in Section 1.4. These measurements are relatively simple. Electrodes are applied to opposite facets of a flat sample, which should be plane parallel in order to achieve a plate-capacitor like structure allowing for a homogeneous electric field distribution inside the sample.

A simple method to measure the *P-E* behaviour is to use the Sawyer-Tower circuit as shown in Figure 24, where the capacitor-like sample at test C_F is in series with a sensing capacitor C_S possessing a much larger capacitance than C_F. The voltage is cycled by the voltage generator $V_i(t)$ which usually

needs to be able to generate high voltages of 10 kV or higher in order to reach electric fields necessary for saturation of ferroelectric samples which are often in the range of 5 kV/mm or above.
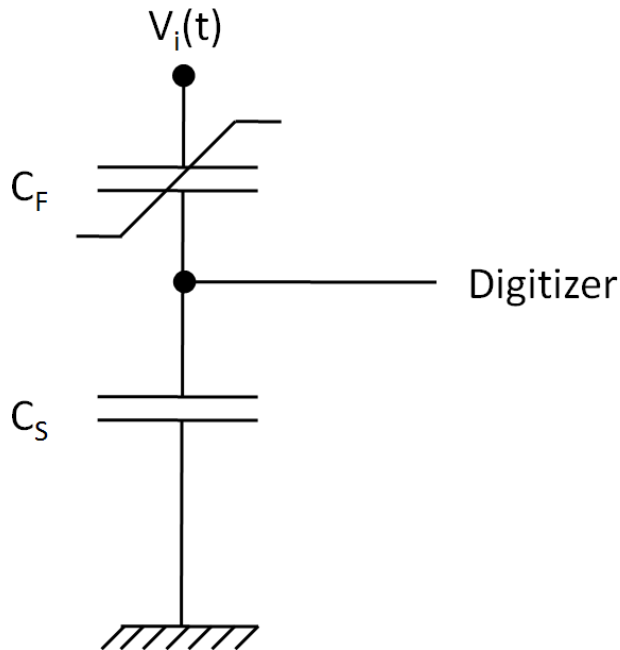
Figure 24 Simple Sawyer-Tower circuit for *P-E* measurements [108].

Since the capacitors are in series, their charge must be the same and the charge on the sample can be found by the capacitance *C* of C_S and the voltage *V* measured across it:

$$Q = C \cdot V.$$

<div align="right">Equation 2-2</div>

By taking the sample's area *A* into account, the polarization can be calculated by:

$$P = \frac{Q}{A}.$$

<div align="right">Equation 2-3</div>

P is plotted against *E* which is calculated from the applied voltage *V* and sample thickness *d*:

$$E = \frac{V}{d}.$$

<div align="right">Equation 2-4</div>

This method has several disadvantages such as a limited frequency window or the back voltage of the sense capacitor causing the voltage across the sample to be asymmetric.

A more accurate method is the direct integration of the charging current I to yield Q, which can be done electronically:

$$Q = \int I \, dt.$$

<div align="right">Equation 2-5</div>

It should be noted that parasitic effects such as leakage currents due to conductivity can mimic ferroelectric behaviour and cause closed loops of switched charge *vs.* applied voltage. However, in those cases the 'hysteresis' loops do not show saturation or a concave Q *vs.* V-region [109]. Therefore, it is important to carry out complementary investigations such as resistivity measurements to support ferroelectric behaviour.

2.4.2 **Permittivity *vs.* temperature**

As outlined in Sections 1.4 and 1.4.3 the permittivity *vs.* temperature behaviour is important to determine T_C of a ferroelectric or to identify relaxor ferroelectric behaviour using frequency dependent measurements. The sample configuration is the same as in *P-E*-measurements except that the sample is situated inside a furnace with automated temperature control and is contacted using silver or platinum wires. The permittivity is calculated using Capacitance C, sample thickness d and area A:

$$\varepsilon_r = \frac{C \, d}{\varepsilon_0 \, A}.$$

<div align="right">Equation 2-6</div>

Furthermore, the imaginary part of permittivity ε'' which corresponds to the out-of-phase response is measured, too:

$$\varepsilon^* = \varepsilon' + i\varepsilon'',$$

<div align="right">Equation 2-7</div>

with the complex permittivity ε^*.

2.4.3 **Piezoresponse force microscopy (PFM)**

A few years after the invention of the atomic force microscope, PFM was first used to image and locally pole ferroelectric domains in polyvinylidene fluoride (PVDF) by Güthner and Dransfeld [110]. Later, important achievements, which led to more widespread use of PFM were made by Gruverman, Kholkin and Kalinin et al. who developed new techniques and improved microscopical understanding of ferroelectrics [111]–[119]. The term piezoresponse force microscopy (PFM) was first coined by Lehnen and Kleemann [120].

Nowadays, piezoresponse force-microscopy (PFM) has become the standard tool to investigate ferroelectrics on the micro- and nanoscale, which is confirmed by the fact that the number of publications with relation to PFM has grown constantly over the past years.

The principle of PFM is relatively simple. The AFM based method, makes use of the converse piezoelectric effect to induce local expansions and contractions in a piezoelectric sample, which are detected by the AFM tip. It requires a conductive AFM tip and a bottom electrode underneath the sample, which are necessary to apply a voltage to the sample. However, sample deformations due to the converse piezoelectric effect are usually only in the range of 100 pm and it is very challenging to measure these small height differences accurately using DC voltages. A way to increase the signal-to-noise ratio significantly is to use an AC voltage instead and detect the resulting movements with a lock-in-amplifier (LIA). The LIA extracts all signals from the photodiode with the same frequency as the AC-voltage applied to the sample. Figure 25 shows the principle of PFM schematically.
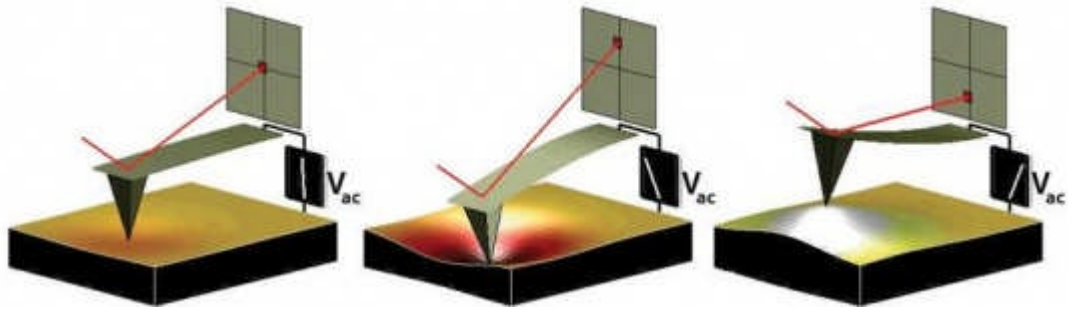
Figure 25 Schematic principle of piezoresponse force microscopy (PFM). Without application of voltage, there is no sample deformation (left). Upon application of an AC voltage, the piezoelectric material underneath the tip contracts and expands (middle and right respectively), which results in AC deflection of the cantilever, detected by the photo diode and extracted by a lock-in-amplifier [121].

The frequency of the AC voltage needs to be chosen sufficiently high so that the topography feedback-loop of the AFM cannot compensate the cantilever deformations. In practice, frequencies are typically in the range of 10 kHz up to several MHz.

In order to increase the Q-factor and thus the signal to noise ratio, PFM can be operated at the contact resonance frequency of the cantilever, which is typically at approximately 300 kHz for cantilevers standardly used in PFM. However, this usually results in strong topography cross-talk in PFM images due to changing contact resonance, which depends on the stiffness of the tip-surface junction. Special methods such as dual AC resonance tracking (DART) [117] and band excitation [122] were developed, which use two frequencies or a band of frequencies respectively, to overcome these drawbacks by effectively tracking the change of the contact resonance. However, conventional single frequency PFM operated away from the contact resonance is still most widely used.

In PFM, it is not only possible to record out-of-plane or vertical PFM signals as shown in Figure 25, but also in-plane or lateral signals, which correspond to shear-deformations of the cantilever resulting in sideways deflection of the laser on the photodiode. This motion can be recorded by a second LIA, which enables simultaneous recording of the lateral PFM signal.

As mentioned above, the dominant contrast mechanism in PFM is the converse piezoelectric effect. Electrostatic contributions or capacitive forces

can also play a role in PFM. However, these can usually be neglected if a sufficiently stiff cantilever in combination with relatively high contact pressure is used [123].

For investigations of the local dipolar structure it is important to understand how PFM signals are recorded and represented.

2.4.3.1 Signal representation

Due to the principle of the PFM experiment, signals should in theory be always either exactly in-phase or out-of-phase with the reference-frequency signal. This corresponds to the fact that the polarization-vector of a ferroelectric domain can either point upward or downward relative to sample surface. PFM signals are complex and can either be represented as sets of X- and Y-amplitude (X and Y) or R-amplitude (R) and phase (Θ) corresponding to Cartesian and polar coordinate systems, respectively:

$$X = R \cos \Theta,$$

Equation 2-8

$$Y = R \sin \Theta.$$

Equation 2-9

R contains the magnitude of the converse piezoelectric response, while Θ conveys whether the response is in-phase or out-of-phase with respect to the reference-signal and thus whether the polarization points up or down. Ideally, X contains both information, where its absolute value and sign correspond to R and Θ respectively. For illustration Figure 26 schematically shows signals for R, Θ and X that would be obtained for domain configurations as shown on the top.
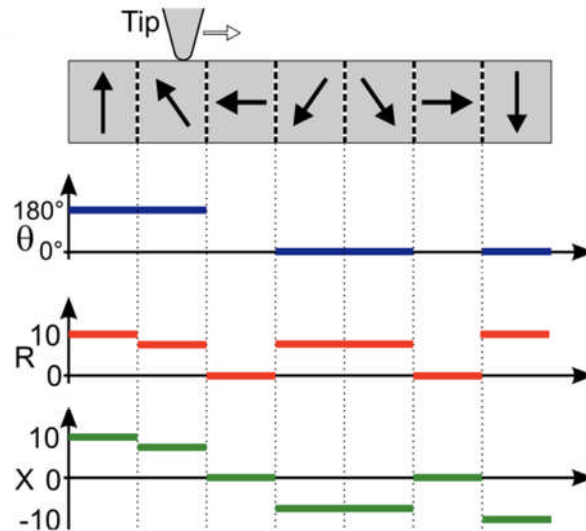
Figure 26 Schematic illustration of theoretical signals of R-amplitude, phase and X-amplitude that would be obtained for above domains [112].

As shown in Figure 26, ideally X might be regarded as a product of R and Θ. Thus, X is also often referred to as 'mixed-signal' in literature.

2.4.3.2 Background-signal and its consequences

Soergel et al. [112][124] reported a frequency-dependent background-signal in PFM. They found that a PFM background-signal could be measured on piezoelectric, but also on non-piezoelectric samples like glass or metal which had exactly the same magnitude when using the same AFM tip and setup. Thus, it was concluded that the background-signal is independent of the sample and was attributed to mechanical resonances of the AFM head. Furthermore, the authors suggested that this background should be subtracted from PFM signals, since it is not due to the piezoelectric effect.

The same group also pointed out the different consequences of this inherent background-signal on representation of signals as R and Θ or as X and Y.

Figure 27 shows phasor-diagrams illustrating these consequences.
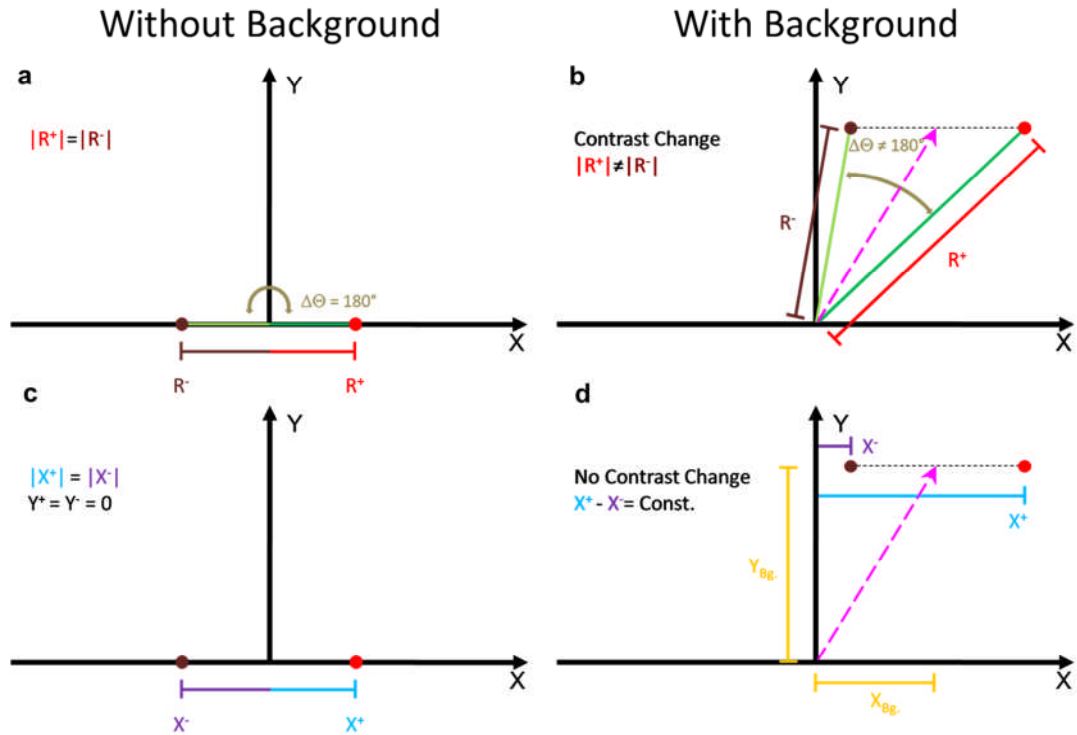
Figure 27 Phasor-diagrams illustrating consequences of background-signal for recording of R-amplitude and phase or for X- and Y-amplitude. Two PFM signals of equal magnitude, but opposite sign are illustrated which correspond to light and dark red dots. Phasor- **a** and **b** illustrate the situation for recording of R-amplitude and phase without and with background-signal respectively. **c** and **d** show the same for recording of X- and Y-amplitude. Partially adapted from [112].

Two PFM signals of equal magnitude, but opposite sign are illustrated which correspond to light (•) and dark red (•) dots. Figure 27a and b illustrate the case when R and Θ are recorded. Values for R corresponding to these PFM signals are represented by the length of red lines R^+ and R^-. Without any background-signal all PFM signals caused by the piezoelectric effect must lie on the X-axis because they can only be in-phase or out-of-phase with respect to the reference signal. Thus, R^+ and R^- have the same length and the angle (Θ) between the two signals is 180°. However, the situation changes when a background-signal is measured on top of signals due to the piezoelectric effect, which is illustrated by the magenta arrow. This background-signal transfers the signals corresponding to up- and down-domain off the X-axis because it is added to the other signals and is neither in-phase nor out-of-phase with the reference-frequency. As a consequence,

R signals for both domains are no longer equal and Θ is different from 180° (Figure 27b).

When no background-signal is present, there is no large difference between recording of X and Y or R and Θ (Figure 27c and a, respectively). In this case the information of R is given by the absolute value, while Θ is represented by the sign of X, respectively. Y does not contain any information in this case. However, if there is background-signal as discussed above, both signals X^+ and X^- are subject to an offset which is the X-component of the background $X_{Bg.}$. The important difference to recording of R and Θ is that although the absolute values of X^+ and X^- change, the difference between the two signals which is the domain-contrast does not. Thus, X^+ and X^- can be corrected by subtracting the background the $X_{Bg.}$ and discarding the signal in Y which only contains the corresponding component of the background-signal $Y_{Bg.}$. $X_{Bg.}$ can be determined by an additional measurement on an appropriate reference sample.

2.4.3.3 Background-signal and calibration

The PFM background-signal $X_{Bg.}$ which can vary with frequency and presumably depends on the condition of the tip, but is independent of the sample, can in principle be determined in two ways. By measuring it on a non-piezoelectric sample, which might be for example glass. The second possibility is to use a single crystalline reference sample, containing only ferroelectric domains with equal magnitude, but different signs of polarization (i.e. only 180° domains). Such a material is periodically poled lithium niobate (PPLN) (see Section 1.7.6). Since the background-signal is equal for both up and down domain, the level of the background-signal is simply the mean of the two signals. This is displayed in an exemplary way in Figure 28, which shows a typical PFM image (X-amplitude) of PPLN (Figure 28a). Here, dark and bright areas correspond to polarization facing downwards or upwards respectively, while the magnitude of the piezoresponse is given by the darkness or brightness of the respective colours. Figure 28b shows the averaged cross-section and the background-signal.
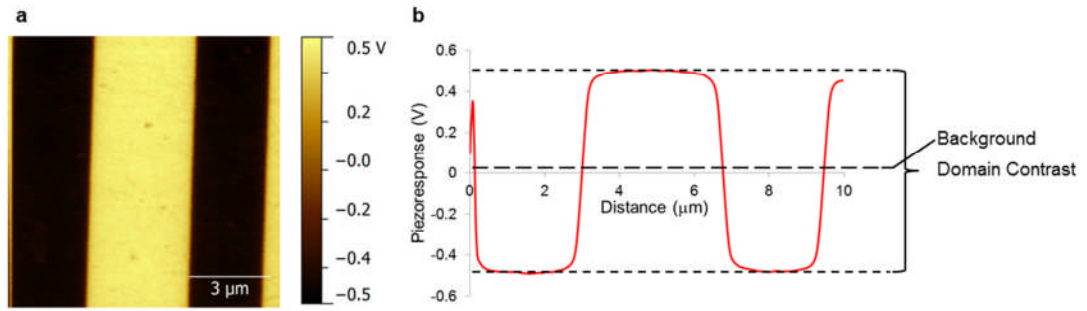
Figure 28. **a**, A typical vertical PFM image (X-amplitude or mixed signal) of PPLN. **b**, Cross-section of image with domain contrast and background-signal.

However, PPLN cannot only be used to determine the background-signal, but also to calibrate PFM signals at the same time. Crystals are usually cut perpendicular to the Z-direction, so that measurements can be carried out on the Z-face. Hence, PFM signals can be calibrated when the signal difference for up and down domains (domain contrast) is related to twice the macroscopic value of the d_{33} coefficient of PPLN which is approximately d_{33} = 20 pm/V [125]. This contrast is displayed in Figure 28b. Additionally, PPLN has the advantages that it is readily available and robust to, e.g., changes in temperature, which makes it an ideal material for calibration and background-signal determination.

2.4.3.4 Background-signal correction

As mentioned before, the background-signal can be corrected for by subtracting it from the PFM X-amplitude, which is displayed in Figure 29.
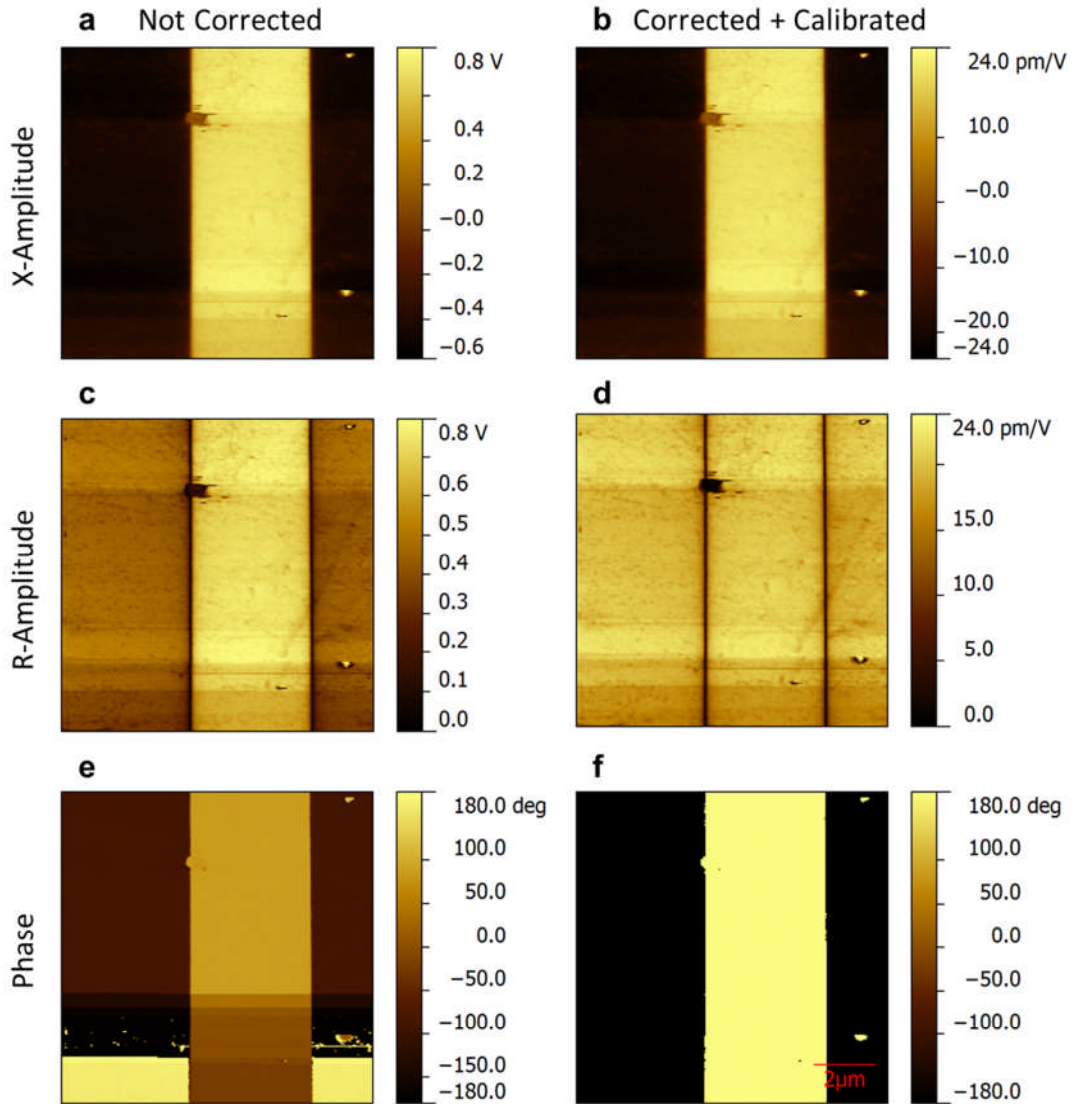
Figure 29 X-, R-amplitude and phase PFM images of a PPLN sample showing the effect of background subtraction. Images **a**,**c** and **e** are as recorded, while in images **b**,**d** and **f** the background-signal is eliminated. Corrected R-amplitude and phase images were generated from the corrected X-amplitude image.

Figure 29a shows an X-amplitude PFM image with a background-signal of approximately 0.13 V (see scale bar, bright corresponds to 0.8 and dark to 0.6 V). which corresponds to approximately 8.8% of the PPLN domain contrast. Figure 29b shows the same image with the background subtracted and PFM signals calibrated with average PFM domain contrast corresponding to 40 pm/V. Note that there is no change of contrast between corrected and uncorrected X-amplitude images as discussed in Section 2.4.3.2.

However, many PFM users prefer data representation in R and Θ, and indeed it can be easier to have separate representations of the information of piezoresponse and direction of polarization since the available image-contrast only needs to cover half of the data-range in case of R as compared to X. R and Θ (Figure 29c and e) were recorded simultaneously to X (Figure 29a). As discussed in Section 2.4.3.2 there is a contrast between the oppositely poled domains in Figure 29c due to the background-signal, although both domains should have equal amplitude in theory. Furthermore, the phase difference between the two domains is not 180° across the whole image (Figure 29e). Additionally, another problem of the phase signal the so-called phase-wrapping occurs, which is a sudden jump to the opposite end of the range due to the signal exceeding a limited range of ±10V or ±180° respectively. This can be seen in the lower half of Figure 29e. The corrected R (Figure 29d) and Θ (Figure 29f) images were obtained by using the absolute value and sign respectively, of the corrected X image in Figure 29b, thus discarding all information in Y-amplitude which only contains background-signal. Now, R and Θ are displayed correctly with equal amplitude for oppositely poled domains and phase difference of 180°. Additionally, this procedure also eliminates the problem of phase-wrapping visible in Figure 29e. The image correction were be done conveniently using built in functions of the free AFM software Gwyddion [126].

2.4.4 **Experimental details**

For electrical testing, silver electrodes were applied onto coarsely polished samples at 550 °C using silver paint. *P-E*-loops and permittivity *vs.* temperature measurements were carried out on a Radiant (Albuquerque, New Mexico, USA) Precision 10kV HVI II and a HP 4284 A Precision LCR Meter (now Keysight technologies, Santa Clara, California, USA) in combination with a tube furnace, respectively.

PFM experiments were carried out on the AFM mentioned in Section 2.3.5 and DCP11 conductive-diamond coated tips by NT-MDT (Moscow, Russia) were used. The tip was electrically grounded whilst a 'bottom-electrode' underneath the sample and in electrical contact with it, was biased. All PFM

imaging was carried out at a frequency of 70 kHz of the AC voltage. The AC voltage applied was usually ±10 V except where explicitly stated otherwise.

Magnetic fields for in-situ under magnetic field PFM experiments were generated by the Magnetic Lateral Field Module 5420 by ScienTec (Les Ulis, France) with magnetic fields of up to ±750 Oe.

2.5 Magnetic characterisation

2.5.1 Magnetization *vs.* magnetic field (*M-H*)

The *M-H* behaviour of a material is essential for characterisation of magnetic materials as was shown in Section 1.5.4, e.g. to distinguish between different magnetic phenomena such as ferromagnetism, superparamagnetism or paramagnetism.

Magnetization is nowadays usually measured using vibrating sample magnetometers (VSM). The sample is usually situated in a chamber which allows temperature control down to the temperature of liquid helium. Furthermore, a homogenous magnetic field which is often generated by a superconducting magnet can be generated at the sample position. When the sample is physically vibrated sinusoidally, typically using a piezoelectric actuator, this causes a sinusoidally modulated magnetic flux according to Faraday's law of induction through a pickup coil situated close to the sample. This modulated flux is detected by a lock-in amplifier using the piezoelectric signal as its reference signal. Thus, only contributions due to the vibrating sample are measured but not due to the external magnetic field. The set-up of a VSM is schematically represented in Figure 30.
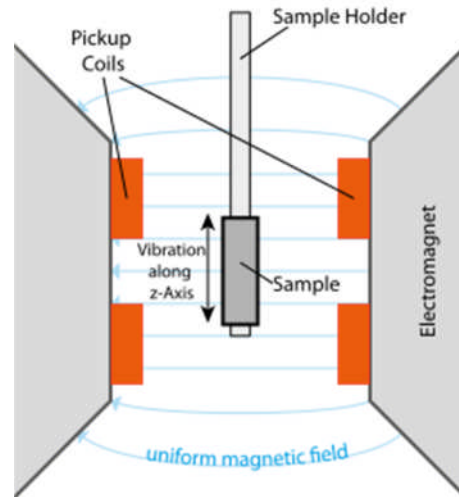
Figure 30 Schematic set-up of vibrating sample magnetometers (VSM) with vibrating sample inside a homogenous magnetic field and pickup coils close to the sample [127].

The magnetic moment of the sample is proportional to the induced voltage in the pick-up coil. By ramping the applied magnetic field, it is possible to acquire the *M-H*-behaviour of a material which can be e.g. hysteretic exhibiting the characteristics as outlined in Figure 13.

Alternatively, magnetization can be measured using a superconducting quantum interference device, SQUID, which is able to measure extremely small magnetic fields due to superconducting loops containing junctions utilizing the Josephson effect. Here the sample is repeatedly moved across a superconducting pick-up loop, which makes the measurement relatively slow compared to VSM measurements. However, nowadays SQUID-VSMs are available which combine the high sensitivity of SQUID and fast measurement VSM.

2.5.2 **Magnetization *vs.* temperature**

In the previous section, the principles of *M-H* measurements were discussed. However, the magnetization *vs.* temperature behaviour of magnetic materials is of utter importance especially when dealing with superparamagnetic materials (ZFC-FC measurements) as discussed in Section 1.5.4 of for determination of the magnetic T_C as outlined in Section 1.5.2.

Temperature dependent measurements are usually carried out at different magnetic fields, since the magnetic field strength often decides which mechanism of magnetization dominates. For superparamagnetic materials for instance, the blocking temperature T_B depends on the magnetic field [38].

Another important method is measuring of the AC susceptibility, χ *vs.* temperature. Here, an AC field is applied to a sample and the resulting AC moment is measured. Those measurements deliver information about magnetization dynamics. Both real, χ', and imaginary part, χ'', can be measured where the latter yields information about energy dissipation and thus can be an indication of magnetic phase transitions.

χ' can be measured as a function of frequency, to characterize spin-glasses which exhibit frequency dispersion [128] similar to relaxor ferroelectrics in permittivity *vs.* temperature behaviour.

2.5.3 Magnetic force microscopy (MFM)

MFM was invented in 1987 by Martin and Wickramasinghe [129] which is, like PFM, a technique based on AFM. It has been used since to study magnetic structures or fields with very high lateral resolution down to several nm. It is the most widely used magnetic microscopy technique together with other techniques like magneto-optical Kerr effect (MOKE) microscopy or X-ray magnetic circular dichroism photoemission electron microscopy (XMCD-PEEM).

In MFM a magnetic tip is used to detect stray fields from a sample surface, which is usually a conventional AFM tip covered with a magnetic layer which is magnetized in the out-of-plane direction, i.e. perpendicular to the sample surface. MFM is a 'dual pass' technique, where each line is scanned in two consecutive passes of the AFM tip across the sample surface. First, the topography is obtained using a pass in conventional tapping mode. In the second pass, the tip is scanned above the surface with a certain height offset which typically lies between 20-100 nm. During the second pass, the tip follows the topographic profile of the sample obtained during the first pass to compensate for any interactions due to sample topography and therefore only detects magnetic forces. The principle of MFM is depicted in Figure 31.
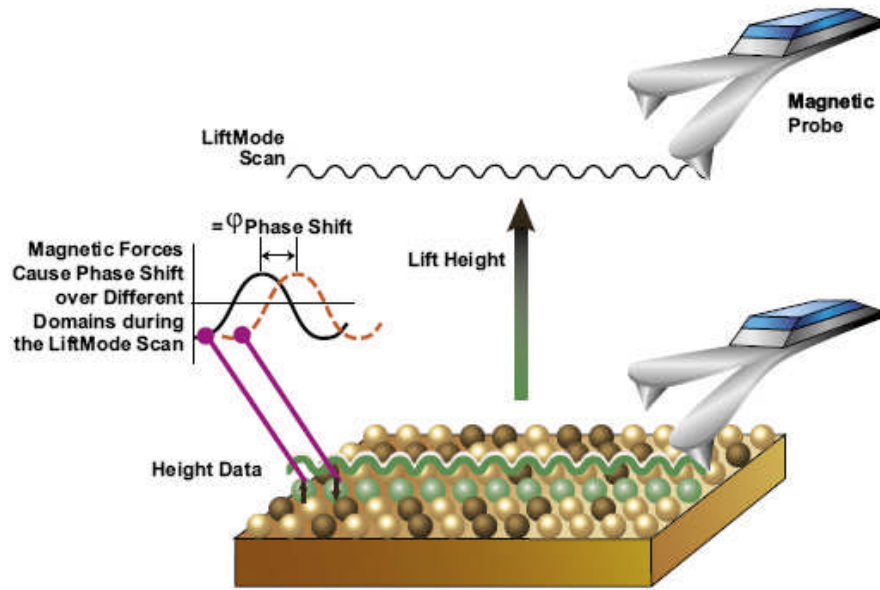
Figure 31 Schematic principle of magnetic force microscopy (MFM). Topography is obtained during first pass in tapping mode, while information about magnetic domains or structures are acquired in the second pass, which tracks the topography profile in a distance to the surface [130].

Magnetic stray fields are usually detected as a change of phase while the tip is oscillated at a constant frequency close to its resonance frequency. MFM is prone to artifacts for example due to electrostatic coulomb interactions between sample and conducting tip. Such artifacts can be ruled out, e.g., by repeated imaging before and after switching the tip's magnetization in an external magnetic field and observation of inverted image contrast. Furthermore, MFM is only sensitive to out-of-plane stray fields, but cannot observe in-plane and out-of-plane magnetization unlike e.g. MOKE.

2.5.4 Magneto-optical Kerr effect (MOKE) microscopy

This microscopy technique makes use of the magneto-optical Kerr effect which describes changes to polarized light reflected from a magnetic surface due to rotation of the light's plane of polarization. Before illuminating the sample, the light first passes through a polarizer filter which creates linearly polarized light. After reflection of light from the sample, its polarization is rotated and it passes through another polarizer filter at close to 90° to the first. An analyser converts the changes of light polarization into changes of intensity, to make magnetic domains visible. Switching of magnetic domains can be observed by applying a magnetic field in-situ. Different geometries of

magnetic field to sample and differently polarized light can be realized in a Kerr microscope, e.g., to measure in-plane or out-of-plane contributions to the MOKE [131]. By using proper calibration procedures absolute values of magnetization can be deduced from Kerr microscopy [132]. Even without calibration, the (anisotropic) coercive field of selected particles or regions can be measured.

2.5.5 **Mössbauer spectroscopy**

Mössbauer spectroscopy is one of the most powerful tools to study magnetism, yet it is practically limited to few elements since an isotope needs to be Mössbauer active, i.e. an excited state with relatively low energy and relatively long lifetime must exist. Furthermore, an appropriate emitter of gamma rays for excitation is required. Fortunately, Fe (^{57}Fe to be exact) as one of the most important magnetic elements, is among those few, since it fulfils the above criteria. A suitable emitter of gamma rays for ^{57}Fe Mössbauer spectroscopy is ^{57}Co, which first decays to an excited state of ^{57}Fe and thereafter decays to the ground state by emitting gamma rays.

Mössbauer spectroscopy which was invented by Rudolf Mössbauer in 1957 is based on recoil-free, resonant absorption of gamma rays in a solid. Since the absorption of gamma rays in a solid occurs to a significant fraction recoil free, the emission and absorption of gamma rays by the same isotope is possible, since no energy is lost to recoil. In Mössbauer absorption spectroscopy, a sample is exposed to gamma radiation which must be emitted from a source consisting of the same isotope as the absorbing atoms in the sample while a detector measures the transmitted radiation. During a measurement the energy of the gamma rays is varied slightly due to the Doppler effect by accelerating the source through a range of velocities using a linear motor. This slight energy variation results in an extremely high energy resolution due to the high energy and extremely narrow line widths of gamma rays. Typical velocities which are used are ±11 mm/s which corresponds to ± 480.075 neV. At certain energies corresponding to resonant absorption into discrete nuclear energy states, a dip in the recorded Mössbauer spectrum occurs. Therefore, even tiny energy changes

can be resolved which are mainly due to three effects influencing an atom's hyperfine structure:

- Isomeric or chemical shift which depends on the state of oxidation and the chemical environment of an atom.
- Quadrupole splitting due to nuclei which are non-radially symmetric (magnetic quantum number above ½) and are subjected to an electric field gradient as in ferroeletric materials.
- Magnetic hyperfine splitting due to the Zeeman effect conveying information about magnetic order.

From these effects, magnetic splitting is most relevant in our case. Hence, the other two effects will not be covered within this thesis. In magnetically ordered materials, the strong local magnetic fields cause hyperfine splitting of nuclear energy states into non-degenerate energy states according to the Zeeman effect. In the case of Fe, restriction rules allow transitions between six energy levels resulting in six absorption lines in Mössbauer spectra. This is regardless of whether magnetic ordering is ferro-, ferri- or antiferromagnetic. Figure 32 illustrates these facts schematically.
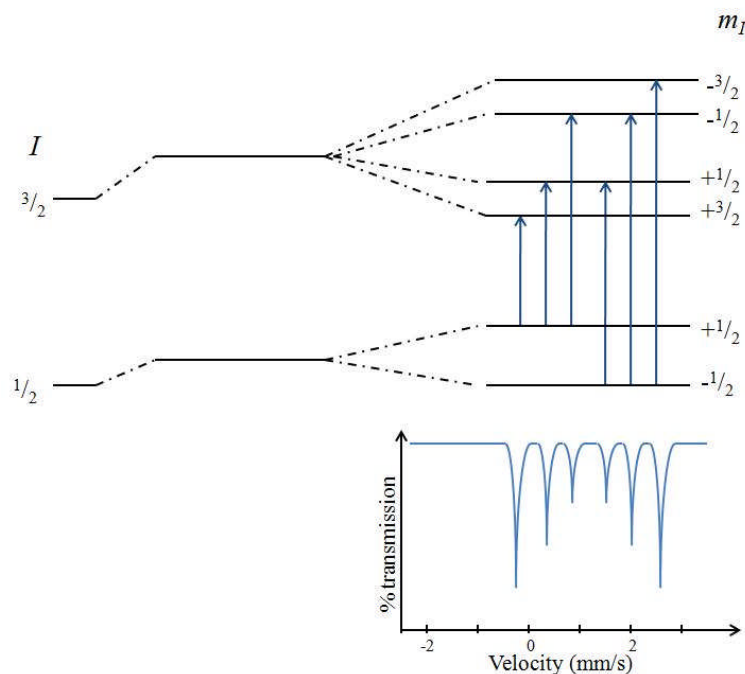
Figure 32 Principle of magnetic or hyperfine splitting due to the Zeeman effect in Mössbauer absorption spectroscopy resulting in six absorption lines [133].

Therefore, Mössbauer spectroscopy is suitable to unambiguously detect element specific magnetic ordering via the occurrence of six absorption lines. Through detailed analysis, much more information can be deduced from Mössbauer spectra, such as Fe occupation of lattice sites in ferrites (degree of inversion). However, the focus of Mössbauer spectroscopy within this thesis lies mainly in the determination of magnetic structure. Thus, other aspects of Mössbauer spectroscopy are not covered in greater detail but the interested reader is referred to more comprehensive sources [134], [135].

2.5.6 Magnetic neutron diffraction

Neutrons with appropriate kinetic energy have similar wavelengths as *X*-rays of the order of 0.1 nm according to de Broglie's theory. Therefore, neutrons are suitable for diffraction experiments in crystals to reveal their structure. But unlike *X*-rays, neutrons are not scattered at the electron cloud, but at the nuclei. Furthermore, there is another fundamental difference between neutron and *X*-ray diffraction: Since neutrons have a spin unlike *X*-rays, they carry a magnetic moment which interacts with that of electrons. Therefore, magnetic peaks or magnetic contributions to diffraction peaks occur in neutron diffraction experiments of magnetically ordered materials in addition to nuclear Bragg peaks which can be used to determine the magnetic structure of a material [136]. In antiferromagnetic materials, additional peaks occur as compared to *X*-ray diffraction pattern, which disappear above the Néel temperature. In simple antiferromagnetic materials, magnetic peaks are half indexed, which corresponds to a doubling of the nuclear lattice constants. In case of ferromagnetic order, there is an additional contribution on top of nuclear Bragg peaks since the ferromagnetic order has the same lattice constants as the nuclear structure. These additional contributions can be best observed with temperature dependent neutron diffraction experiments where the additional contributions disappear above the Curie temperature. For ferrimagnetism, a mixture of antiferromagnetic and ferromagnetic behaviour is observed since the compensated part of spins cause antiferromagnetic peaks, while the uncompensated moments cause additional magnetic contributions with the same lattice constants as nuclear Bragg peaks. These facts are schematically illustrated in Figure 33.
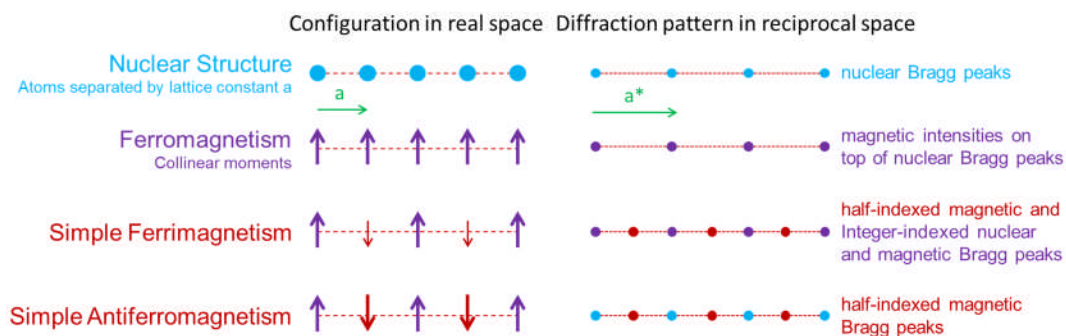
Figure 33 Illustration of simple types of 1D magnetic order and corresponding neutron diffraction pattern. Adapted from [137].

2.5.7 Experimental details

For magnetic measurements, the powder of sintered and crushed pellets was used and measurements were carried out on a SQUID-VSM MPMS 3 by Quantum Design (San Diego, California, USA). High temperature magnetometry measurements were performed on a Quantum Design PPMS DynaCool using the VSM oven option.

Most MFM measurements were carried out on the AFM mentioned in Section 2.3.5 with lift heights of 70-100 nm. PPP-MFMR AFM tips by Nanosensors (Neuchatel, Switzerland) with a magnetic coating with 300 Oe coercivity and remanent magnetization of approximately 300 emu/cm^3 were used. Some MFM measurements were carried out on an AttoMFM I by Attocube (Munich, Germany) which is explicitely stated in the text. All MFM images presented in this thesis show the phase of the second pass scan and were measured in a constant frequency mode.

Magneto-optical Kerr effect (MOKE) hysteresis loops were taken using an Evico (Dresden, Germany) wide-field Kerr microscope, set to be sensitive to the longitudinal Kerr effect. To take a hysteresis loop, the intensity of light from a selected region of the microscope image was monitored, while an in-plane magnetic field was swept.

Mössbauer spectroscopy measurements were performed using a constant acceleration spectrometer in transmission geometry with a ^{57}Co source (Rh-matrix). Powder from crushed sintered pellets was mixed with chemically inert boron nitride. Measurements below ambient temperature were

conducted using a liquid helium bath cryostat. Spectra were analyzed using the 'pi'-program package .

Neutron diffraction was carried out on the D1B - High resolution neutron two-axis powder diffractometer at the Institut Laue-Langevin (ILL) in Grenoble, France. The schematic instrument layout is shown in Figure 34.
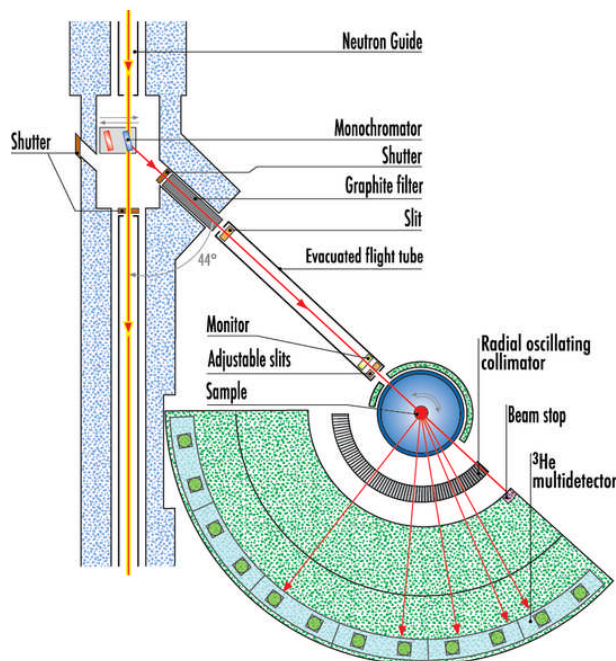
Figure 34 Schematic instrument layout of D1B neutron powder diffractometer at ILL [138].

Pyrolitic graphite monochromators (002 reflection) were used for neutrons with a wavelength of 2.52 Å. In case of BFC-BKT, ceramic pellets with 8 mm diameter were used in a vanadium can with total sample weight of approximately 17 g. In case of PZT-PFW, crushed ceramic pellets were filled in a vanadium sample can with total sample weight of approximately 20 g. A cryo-furnace sample chamber was used for temperature dependent measurements, which allowed temperature control between 1.5 and 550 K.

The resolution function of D1B, which will be used to calculate the size of magnetic regions, is shown in Figure 35.
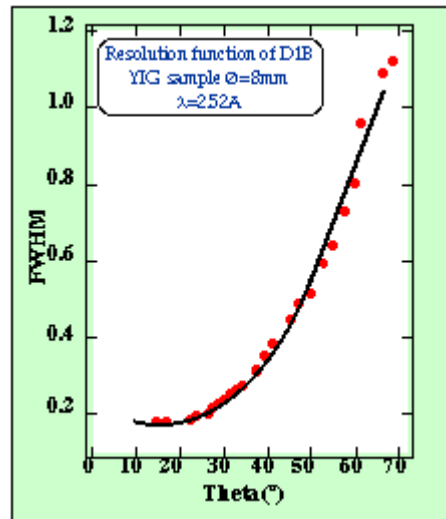
Figure 35 Resolution function of D1B measured on yttrium iron garnet with neutrons at λ = 2.52 Å [139].

Further information can be obtained on the instrument's website [138].

3 Signal stability and calibration in piezoresponse force microscopy

3.1 Chapter overview and motivation

As mentioned in Section 2.4.3 piezoresponse force-microscopy (PFM) has become the standard tool to investigate ferroelectrics on the micro- and nanoscale. For the experimental work of this thesis, PFM also plays a vital role for investigation of dipolar microstructure and also for local ME coupling where PFM is employed under in-situ magnetic fields. Here, one of the goals was to quantify PFM signals, in order to measure local ME coupling coefficients locally. However, stability and reproducibility of PFM signals is usually problematic and their quantification is challenging [140] and thus not widely applied [112]. The possibility to reproduce PFM experiments especially concerning the magnitude of obtained signals has been a matter of debate.

For this reason, a statistical study on the stability of PFM signals and on the magnitude of the background-signal is presented in this chapter, in order to make an estimation on how reliably ME coupling coefficients could be determined with PFM. The background-signal which is presented in Sections 2.4.3.2 to 2.4.3.4 was studied because it can have a significant influence on PFM signals and should be corrected for. Furthermore, practical aspects concerning PFM imaging like choice of the tip, imaging artifacts, and correct sample preparation are presented in this chapter. Lastly, preliminary experiments for PFM under in-situ magnetic field to investigate the influence of the magnetic field on PFM signals are presented.

3.2 Stability of the instrument

Before PFM studies were started, preliminary experiments on general stability of the instrument were carried out. Here, the tip was approached to the fixed and rigid sample and kept in one position for a certain time with the feedback loop enabled. It was found that the value for topography changes

after the tip was in contact with the sample surface, which is shown in Figure 36.
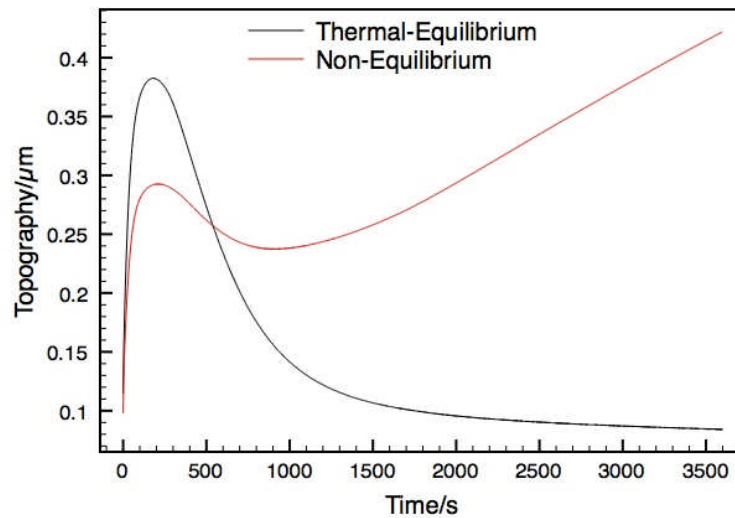
Figure 36 Topography value *vs.* time, shortly after the AFM tip was approached to a rigid surface, when the laser was switched on shortly before (—) or several hours (—) before the experiment was carried out.

In the case where the laser diode was switched on long before the experiment, the topography value had returned to its initial value after approximately 20 minutes. This initial change of topography seems to be an inherent instability of the instrument, which was verified in cooperation with technicians of the manufacturer. However, if the laser diode was switched on shortly before the experiment (red curve), there is a constant increase of the topography value over time in addition to the initial increase. This constant increase is probably due to heating of the laser-diode. Laser diodes usually increase their intensity for some time due to heating after they were switched on. Because in contact mode the laser is not centred on the photodiode which was also the case here, an increase of laser intensity gives rise to a change of topography as observed here.

Nevertheless, it is possible to run PFM experiments with good stability. In Figure 37 cross-sections of 20 consecutive images (averaged over 256 lines) are presented.
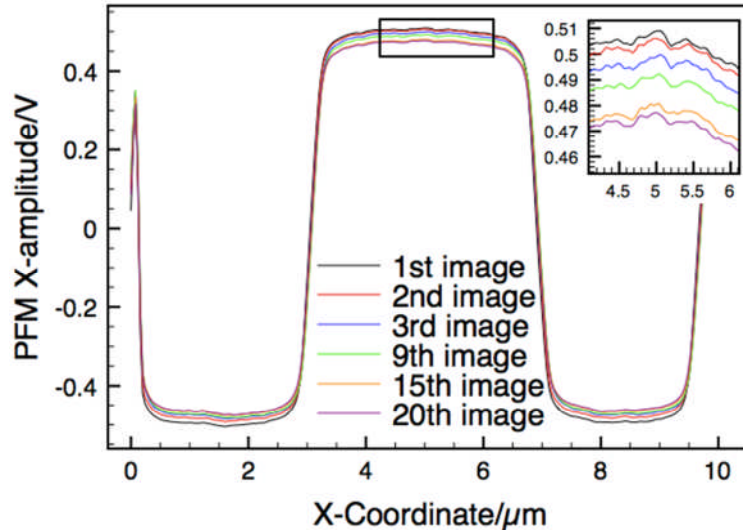
Figure 37 Cross-sections of PFM images taken on PPLN averaged over 256 scan lines. PFM signals remain almost stable for 20 consecutive images with only little decrease of the PFM signal over scanning time.

After recording 20 images with 256 scan lines (10 x 10 μm), there is only a small decrease of the domain contrast of approximately 6 %, which might be attributed to wear of the conductive layer. Furthermore, the PFM signal changes approximately linearly with the number of images. However, it should be noted that PFM signals can be in some cases much less stable and can change several times during one image (see Sections 3.4 and 3.5), which is attributed to the mechanical stability of the tip or the level of contamination of the sample surface.

3.3 Frequency dependent background-signal

First, experiments were carried out, to verify whether results by Soergel et al. [112] regarding the background-signal could be confirmed, i.e. whether the background-signal is dependent on the frequency of the driving voltage and not on the sample. PFM measurements were carried out both on PPLN and on glass.
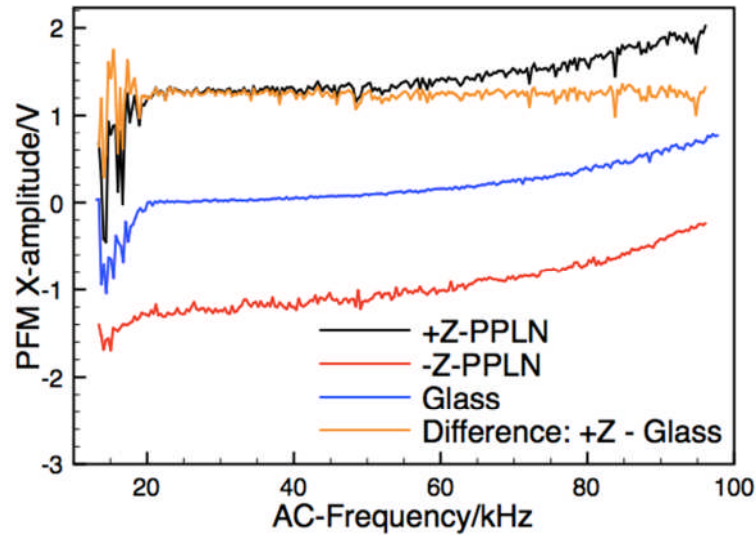
Figure 38 X-amplitude PFM signal *vs.* frequency of the driving voltage measured on a +Z- and -Z-PPLN domains and on glass.

Figure 38 shows that even on non-piezoelectric glass, there is a PFM signal different from 0 for frequencies above approximately 40 kHz, which shows that there is apparently a background-signal above these frequencies. Furthermore, the frequency dependence of PFM signals on PPLN and glass is approximately the same which supports that the background-signal is independent of the sample as found by Soergel et al. This becomes obvious when looking at the difference between the signal for the +Z-PPLN domain and glass which approximately stays constant with frequency while the value of the difference corresponds to the piezoelectric coefficient of PPLN with subtracted background signal.

Furthermore, in agreement with considerations in Section 2.4.3.3 the mean value of PFM signals measured on +Z- and –Z-PPLN domains is approximately equal to the PFM signal measured on glass, which both show the background-signal. Thus, experiments by Soergel et al. could be confirmed.

3.4 Statistical assessment of signal stability and background-signal

3.4.1 Quantification of PFM signals using the z-piezo method

In the scientific community, the reproducibility of PFM signals has often been a matter of debate. Researchers who express doubts about the reproducibility refer to PFM measurements taken on PPLN on different days, which are shown in Figure 39 [141].
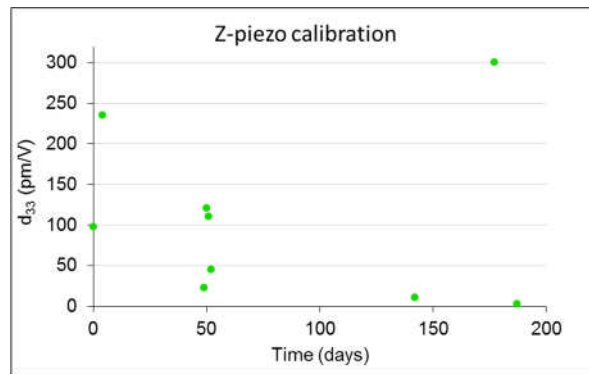
Figure 39 Piezoelectric coefficients of PPLN measured by PFM on different dates using the z-piezo method [141].

Measured values on PPLN on different days range from 3 to 301 pm/V, while the average deviation from the mean is 76.9%. These measurements would in fact suggest that reproducibility of PFM measurements is hardly possible. However, these PFM signals had been calibrated using a technique which shall be referred to as z-piezo method henceforth. It is proposed that the large deviation of PFM signals is, at least partly, due to the inaccuracy of this method as will be discussed below.

The z-piezo method is currently one of the most widely used techniques of quantification in PFM, since it is standardly implemented in AFMs by Asylum Research[®] which are widely used for PFM. It involves the z-piezo element of the AFM [142], [143]. The principle is illustrated schematically in Figure 40.
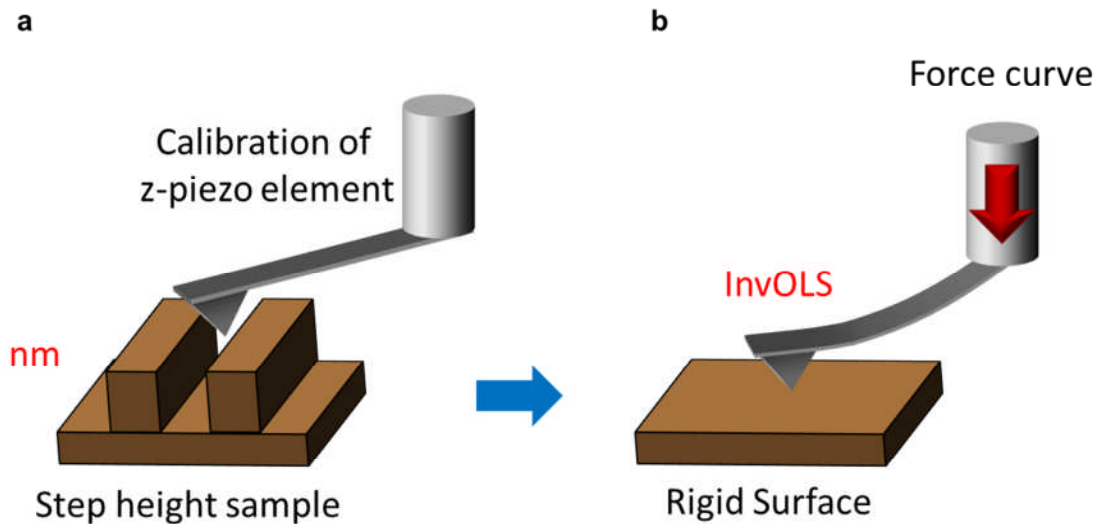
Figure 40 Schematic illustration of the z-piezo method which involves: **a** calibration of the z-piezo element and **b**, obtaining the inverse optical lever sensitivity (InvOLS) by taking a force curve on a rigid surface.

Initially, this method requires calibration of the z-piezo element, e.g. by using a height-calibration sample (Figure 40a). Afterwards, the so-called inverse optical lever sensitivity (InvOLS) which connects cantilever deflection to a certain height difference is obtained. This can be extracted from the slope of the repulsive part of a force curve taken on the sample. With this method, cantilever deflections can in principle be related to sample deformations due to the converse piezoelectric effect and thus PFM signals can be quantified.

However, a major drawback of this method is that force curves are taken at much lower frequencies as compared to cantilever deflections in PFM experiments, which are in the range of several 10 kHz up to several MHz. This discrepancy inevitably results in a calibration error, e.g. due to the frequency dependence of electronic components of the AFM system such as the four-quadrant photodiode or electric amplifiers. The fact that the initial height information ultimately used for PFM signal calibration is obtained on height-calibration samples, which are usually 2-3 orders of magnitude larger than actual sample deformations measured in PFM, adds another factor of uncertainty. Furthermore, height-calibration involves the use of the AFM's feedback loop, which is not the case in a PFM experiment.

3.4.2 **Quantification of PFM signals using a reference sample**

A more accurate method for quantifying PFM signals might be to use a ferroelectric reference sample as was already discussed in Section 2.4.3.3. Such an approach has the advantage that conditions during calibration (frequency, magnitude of deformation) are very similar as during the actual measurement, which would eliminate several errors with respect to the z-piezo method. However, due to the inherent background-signal in PFM a single crystalline reference sample, containing only ferroelectric domains with equal magnitude, but different sign of polarization (i.e. only 180° domains), should be used to calibrate PFM signals and measure the background-signal at the same time. Since the background-signal is equal for both up and down domains (see Section 3.3), the level of the background-signal is simply the mean of the two signals. One material that fulfils those requirements is PPLN (see Section 1.7.6 and 2.4.3.3). In order to assess the stability of PFM signals, the statistical deviation of PFM signals was measured on PPLN randomly on different days analogously to measurements presented in Figure 39. Furthermore, the background-signal was determined at the same time to assess its magnitude and influence on PFM signals. These results are important to answer the question, to what extent PFM signals are reproducible at all. But it is also important for the prospect of using PPLN as a reference sample to get an estimate on the stability of calibration over a certain time.

Two different types of AFM tips were used: NCP-14 Ti/Pt by Mikromasch® with a conductive layer of Pt on top of a Ti layer and DCP 11 by NT-MDT®, which were coated with a conductive layer of nitrogen doped diamond. Both types of cantilevers are made of doped silicon with typical force constants of approximately 5 N/m. As reference signal, the difference of X-amplitude PFM signals between +Z and –Z domain (up and down domain) of PPLN was used, which was usually averaged over 256 lines of the PFM image. A contrast in the Y-amplitude between +Z and –Z domain was usually minimized by adding a phase-shift to the LIA signal with respect to the drive signal. However, the contrast in the Y-amplitude was always small compared to the contrast in X-amplitude as expected in PFM due to the fact that

signals should in principle be always in-phase or 180° out of phase with respect to the driving frequency [124]. PFM measurements were carried out using the parameters as listed in Section 2.4.4.

All values presented here were taken on different days and no specific condition of the tip was maintained e.g. values were not necessarily recorded with a new or sharp tip. Tips might have been new, but also heavily used or blunt. Usually values would stay relatively constant during the same day when multiple measurements were carried out on that day (see Section 3.2). Only one value was picked for a single day to assess the variation of PFM signals over longer timescales more realistically. PPLN results for conductive diamond and Pt coated tips are illustrated in Figure 41a, c, e and Figure 41b, d, f respectively.
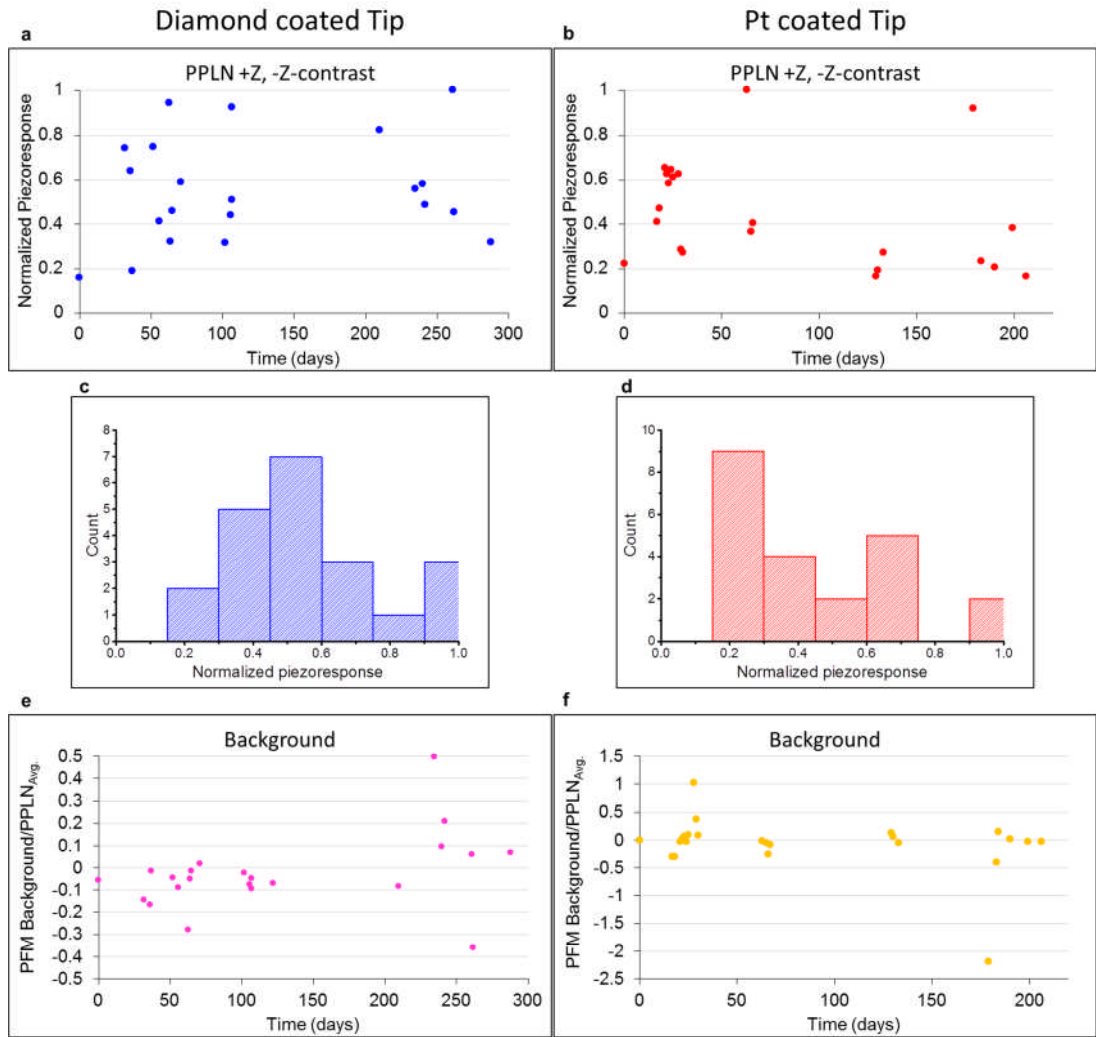
Figure 41 Vertical PFM contrast of +Z to –Z domains of PPLN measured with a conductive diamond coated tip **a** and a Pt coated tip **b**. PFM background-signal divided by average +Z to –Z PPLN domain contrast (PPLN$_{Avg.}$) for conductive diamond coated tip **c,e** and Pt coated tip **d,f**.

Overall, signals varied between 0.26 V and 2.40 V (Output voltage of LIA) with average deviations of 38.3% and 48.8% of the mean for diamond coated and for Pt coated tips respectively. For both tips, similar signals for the domain contrast (close to 1 V) were measured, which indicates that the magnitude of the piezoresponse is similar for both tips. It is important to note that the spread of values for diamond and Pt coated tips differ signicantly (Figure 41a and b). In case of diamond coated tips, the spread of values is rather uniform, whereas for Pt coated tips, there are few very high values and the majority of values being in the range between 10-50% of the highest (see histograms in Figure 41c and d respectively). It is assumed that the

large values correspond to an intact conductive layer while the lower ones correspond to worn tips with degraded conducting layer. Since both new and used tips were used randomly for both tip types, it seems that Pt coated tips degrade much faster which results in the majority of measurements having low values, while diamond coated tips seem to always remain very stable. This is in line with the observation, that the resolution of new Pt coated PFM tips decreased very rapidly (approximately a few scans with 5 x 5 μm scan size and 256 lines) during imaging, whereas this is not the case for diamond coated tips. Of course, this is expected from the mechanical properties of the two film materials. Fast degradation of the Pt layer is probably due to scanning in contact mode and the relatively stiff cantilevers used for PFM. This diminishes the advantage of lower tip diameter of Pt coated tips (approximately 25 nm) in comparison to diamond coated tips (approximately 100 nm). Figure 41f and e show that the background-signal can vary strongly from -218.9% up to 102.5% of the average PPLN domain contrast for the platinum coated tip while for the diamond coating the range lies only between -35.8% and 49.9%. While the average background signal over many measurements is close to 0 for both tips, the average deviation from 0 per measurement are 11.6% and 24.0% of the mean PPLN domain contrast for diamond and Pt coated tips respectively. Thus the background-signal should not be neglected for samples with a similar piezoresponse as PPLN, which is the case for many ferroelectric samples. If the background-signal is not corrected, it distorts PFM signals (especially R-amplitude and phase) as shown in Section 2.4.3.2 and should be corrected by determining the background-signal and subtracting it from X-amplitude data as shown in Section 2.4.3.4.

The above results are summarized in Table 1.

Technique	PPLN		z-Piezo[141]
Tip	Cond. Diamond	Pt on Ti	-
Min, Max value for PPLN contrast	0.266, 1.62 V	0.345, 2.47 V	3.00, 301 pm/V
Mean value	0.971 V	1.03 V	105 pm/V
Average dev. of mean	38.3%	48.8%	73.1%
Min, Max value of background/PPLN$_{Avg.}$	-35.8%, 49.9%	-219%, 103%	-
Mean value of background/PPLN$_{Avg.}$	-2.91%	-7.01%	-
Average dev. of background from 0/PPLN$_{Avg.}$	10.5%	26.0%	-

Table 1 Comparison of results of PFM signal stability and background for different conditions.

The results indicate that PFM data are reproducible to a certain extent although signal variation is relatively high. However, taking in mind that PFM is a technique based on scanning probe microscopy, which is usually very sensitive to the state of the tip (e.g. contaminations, electric field distribution at the tip apex), the relatively large deviation is not surprising. Tips coated with conductive diamond exhibit better signal stability and lower background-signals as compared to Pt coated tips.

Furthermore, the results indicate that the poor reproducibility found by Gruverman et al. [141] is at least partly due to the z-piezo calibration method, which adds another factor of uncertainty to the experiment.

3.5 Imaging artifacts

As discussed previously, PFM is a technique which depends strongly on the state of the tip and is relatively prone to imaging artifacts. Figure 42 shows an artifact which is frequently encountered in PFM.
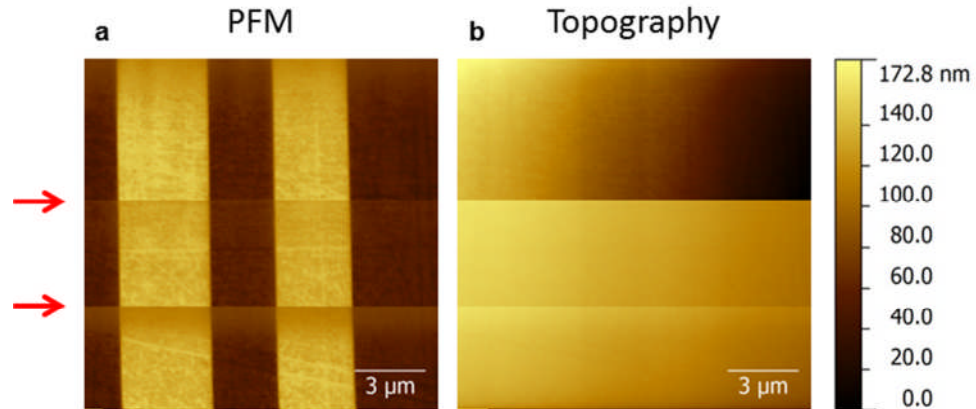
Figure 42 Common artifact in PFM. 'Skips' occur in (vertical) PFM (X-amplitude or mixed signal) image **a** and topography **b** in the same line (indicated by red arrows).

Here (vertical) PFM signals (X-amplitude) decrease gradually while scanning (direction of scanning is up) until a 'skip' in the signal occurs (Figure 42a, marked by red arrows). These sudden changes are often accompanied also by a skip in the absolute values for topography, which is visible in the unflattened topography image (Figure 42b). It was found that these skips are associated to the PFM experiment, because they occurred almost only when an AC voltage was applied. The skips are attributed to a sudden change of the conductive layer of the tip or to a sudden release of contaminants on the tip-apex which both result in a sudden change of PFM signals due to a sudden change of the electric field distribution at the tip-apex. Furthermore, these skips occurred much more frequently in case Pt coated tips were used, as compared to diamond coated tips. This is in line with the above explanation of the skips because the much improved stability of the conductive layer as compared to Pt will reduce sudden damages to the conductive layer of the tip. This is in line with the above findings of lower signal spread for diamond coated tips. Therefore, the use of diamond coated tips is strongly recommended for PFM.

3.6 **Influence of sample preparation**

As mentioned in Section 2.3.1, AFM requires very flat sample surfaces with sample roughness below 1 μm.

Figure 43 shows the influence of appropriate sample polishing on PFM signals.
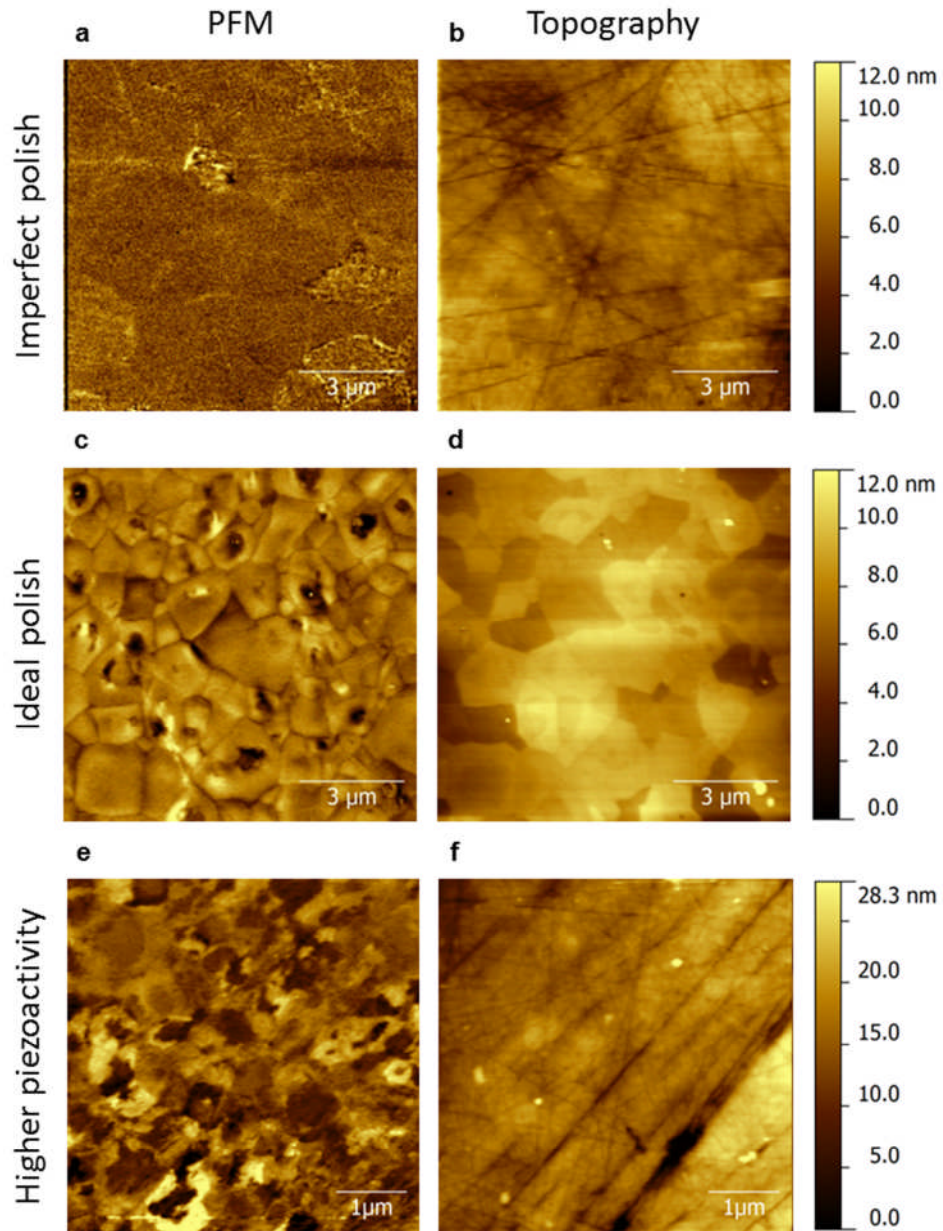
Figure 43 Influence of polishing on PFM signals. Images **a-d** were all obtained on the same material $(BiFe_{0.9}Co_{0.1}O_3)_{0.4}$-$(Bi_{1/2}K_{1/2}TiO_3)_{0.6}$ which has a relatively low d_{33} coefficient. Images **a** and **b** were obtained on a sample that was not sufficiently polished, while images **c** and **d** were obtained on a well polished sample. PFM images **e** and **f** were taken on a $(BiFeO_3)_{0.65}$-$(PbTiO_3)_{0.35}$ ceramic with relatively high d_{33} coefficient. Here PFM signals are strong, even though the sample is not perfectly polished.

Figure 43a,b and Figure 43c,d show (vertical) PFM images (X-amplitude) and topography for an insufficiently and for a well-polished sample of the

same composition, respectively. Note that while in Figure 43b scratches are visible in topography, this is not the case for Figure 43d, where no scratches are visible and the grain structure is revealed through appropriate polishing. The corresponding PFM images differ largely. While the PFM image corresponding to the insufficiently polished sample (Figure 43a) is very noisy and barely exhibits any PFM contrast, the image corresponding to the well-polished sample (Figure 43c) exhibits strong signals and a clear ferroelectric pattern. Those images were all recorded on perovskite ceramic samples of the material $(BiFe_{0.9}Co_{0.1}O_3)_{0.4}$-$(Bi_{1/2}K_{1/2}TiO_3)_{0.6}$, which has a low d_{33} coefficient of approximately 16 pm/V.

All ceramics shown in Figure 43 were polished using a multistep polishing route presented in Section 2.2.3 except that the last polishing step involving 200 nm sized colloidal silica particles was only carried out on the sample corresponding to Figure 43c,d. It is obvious that this step is particularly important and is mainly responsible for the difference between samples shown in Figure 43d and Figure 43b,f.

For ceramics of $(BiFeO_3)_{0.65}$-$(PbTiO_3)_{0.35}$, which exhibit higher piezoelectric coefficients, this does not seem to be the case. Here, strong PFM signals and a clear FE pattern are obtained, although the sample surface exhibits scratches (see Figure 43e,f). It is concluded that PFM signals strongly depend on the quality of polishing for materials with low piezoelectric coefficients, whereas for samples with higher coefficients, this does not seem to be the case. Although, a perfect polish does not seem to be very important for highly piezoelectric samples, it is always beneficial to measure on well-polished ceramic samples in order to be able to correlate the true microstructure as visible in Figure 43d with the dielectric structure from PFM.

3.7 Influence of in-situ magnetic field on PFM signals and drift

ME coupling coefficients especially for single-phase multiferroics are often small. Thus it is very important for local ME coupling investigations that the magnetic field does not cause a change of PFM signals itself without the presence of any ME effect. To this end, the influence of the magnetic field on

PFM signals was investigated. PPLN was used again as a non-magnetic and ferroelectric reference sample. Figure 44 shows investigations of the magnetic field influence on the PFM signal.
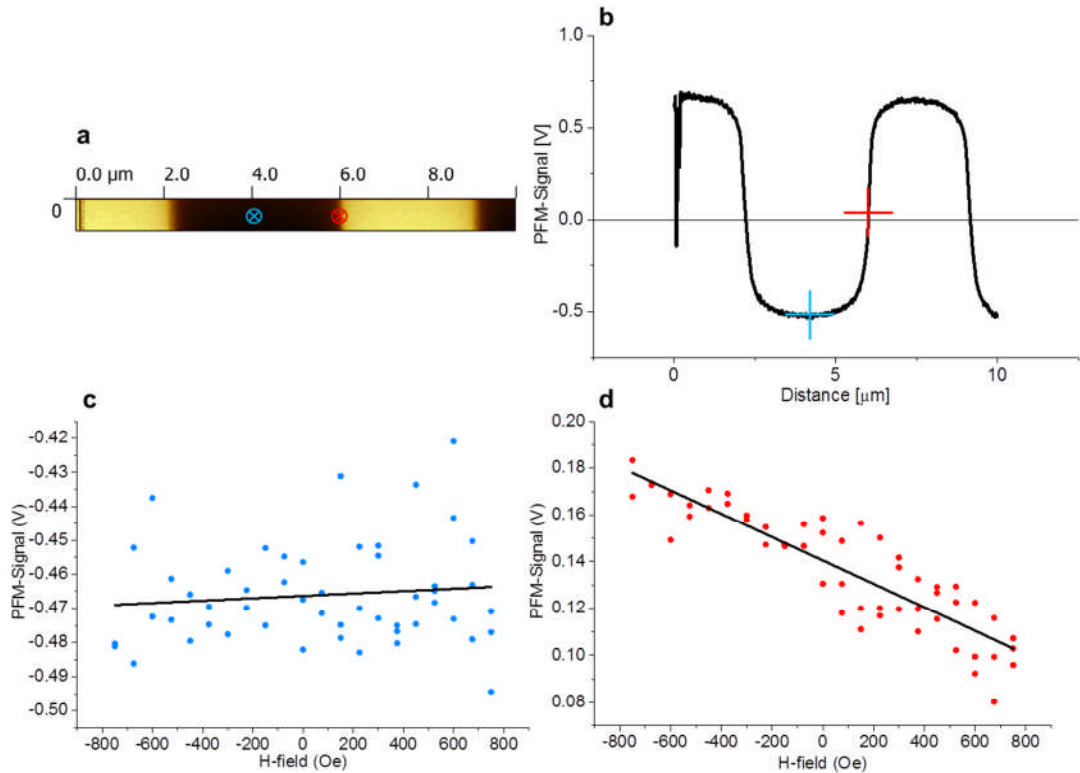
Figure 44 Influence of magnetic field on PFM signal. **a** High resolution PFM (X-amplitude) image of PPLN. **b** Cross-section corresponding to **a**. Positions of the AFM tip for measurements shown in **c** and **d** are marked by blue and red marks respectively in **a** and **b**.

Figure 44c shows a PFM signal *vs.* magnetic field measurement carried out in the centre of the dark ferroelectric domain as indicated by blue marks in Figure 44a and b. The data points are scattered almost randomly while the slight slope of the linear fit through the data points is attributed to a slight relative movement between sample and tip due to the magnetic field. This slight movement is confirmed by the measurement presented in Figure 44d, which was recorded at the domain boundary as indicated by red marks in Figure 44a and b. It is obvious that the relative movement has a much larger influence on the PFM signal at this position due to the much higher slope as shown in Figure 44b. The same measurement carried out on the other domain boundary visible in the left half of Figure 44a yielded the same result but with inverted slope as expected. The relative movement between sample

and tip is estimated to be less than 10 nm by relating minimum and maximum PFM signals in Figure 44d to corresponding X-coordinates in Figure 44b. However, it was observed that relative sample to tip movements increased for longer duration of magnetic field activation. It is possible that the small relative displacements are due to parts, in the tip and sample environment e.g. in the nose cone holding the AFM cantilever, which are slightly magnetic. However close to tip and sample only non-magnetic parts were used where possible. For example aluminium was used as bottom electrode underneath the sample, which reduced sample drift dramatically as compared e.g. to brass which was found to be slightly magnetic probably due to iron impurities.

Additionally, the slight relative movement might be also due to thermal drift caused by the electromagnetic field generator. However, the temperature change at the sample position due to the electromagnet was small. At operation in full power over several hours the temperature change at the sample position was approximately 2°C.

However, due to the drift during magnetic field operation, it is advisable to carry out ME investigations not only in one sample position, but to record consecutive images at certain magnetic fields to ensure that changes of PFM signals are not due to the drift, especially when magnetic fields are applied over longer times.

3.8 **Conclusions**

In this chapter, investigations on signal stability and background-signal in PFM and related topics were presented.

Preliminary studies of the instrument's stability were followed by general investigations of PFM signal stability and background-signal. It could be shown that it is possible to acquire PFM signals stable over longer times of scanning and over many images with a large number of scan lines. Previous results by Soergel et al. [112] about the frequency dependent, but sample independent background-signal in PFM could be confirmed. A statistical assessment of the long term reproducibility of PFM signals and of the magnitude of the background-signal revealed that PFM signals recorded on

one particular sample independently on different days are reproducible to a certain extent, although signal variation is relatively high. This is in contrast to data from literature [141], which suggested no appreciable reproducibility of PFM signals. The average deviation of the mean PFM signal for the PPLN domain contrast is 38.3% and 48.8% for tips coated with conductive diamond and platinum respectively. The background-signal which was obtained as the mean value of the PFM signal on +Z and -Z PPLN domains could in extreme cases be higher than the PPLN domain contrast for single measurements. The average deviation of the background-signal from 0 per measurement was 10.5% and 26.0% of the average PPLN domain contrast for diamond and platinum coated tips respectively. Thus, the background-signal cannot be neglected and should be corrected for as presented in Section 2.4.3.4.

The better reproducibility of diamond coated tips is also supported by the observation that typical PFM artifacts such as sudden changes of PFM signals (see Figure 42), which occur much less frequently for these tips as compared to Pt coated tips. Based on these findings, it is strongly recommended to use tips coated with conductive diamond for PFM.

Furthermore, it was shown that appropriate polishing of samples has a crucial influence on PFM signals especially for samples with low piezoelectric coefficient. Therefore, a multistep polishing route involving 200 nm sized colloidal silica particles as the last step of polishing is recommended. For samples with higher piezoelectric coefficient, the influence of surface treatment does not seem to be as important. However, it is advisable in any case to polish the sample surface appropriately in order to reveal e.g. the grain structure of a material, which remains concealed without the use of e.g. colloidal silica particles or similar agents.

Finally, it was shown that there is no intrinsic influence of the in-situ magnetic field on PFM signals. Changes of PFM signals are probably only due to a slight relative tip-to-sample movement which is in the order of 10 nm. However, especially when magnetic fields are applied for longer times, the drift can be larger. Thus, complete images should be acquired at

different magnetic fields instead of recording PFM *vs.* magnetic field only in a single point.

4 Marking of distinguishable micro-areas for microscopy using TEM grids

4.1 Chapter overview and motivation

This chapter will introduce a method that was developed during the project to mark individual micron sized areas in order to study the very same area with different microscopy techniques. Since the main topic of this thesis are single-phase multiferroics, it is obvious that a combination of different microscopy techniques is desired to study local dielectric and magnetic structures. However, this approach is not only important for multiferroic materials, but also for a large number of today's (nano)-functional materials, usually exhibiting complex physical properties and require local investigation with different microscopy techniques covering different physical aspects. Material classes which belong to this group are for example functional oxides, semiconductors or biomaterials. In modern materials science, a general tendency is the progressive miniaturization of feature or device sizes [144]. At the same time, multifunctionality becomes more and more important, thus material properties become more and more complex. Therefore, it becomes necessary to study their multiple properties with different microscopy techniques suitable for investigating different properties. These can provide information on, for example, local composition, crystal structure, mechanical properties, magnetic and dipolar order [115]. Areas of materials research where it is important to acquire these information locally, are in multiferroics, Li-ion battery, fuel cell materials and graphene [7], [145], [146]. As has been discussed in Chapter 2, there exist numerous microscopy techniques today which are able to measure different properties with high spatial resolution. Among those certainly are AFM with related techniques PFM and MFM (see Sections, 2.3.1, 2.4.3, 2.5.3 respectively) as well as electron microscopy (see Section 2.3.2) or confocal laser scanning microscopy [147] for all of which, numerous sub-techniques have been developed. However, it is often necessary to use these different techniques on the very same sample area in order to truly correlate the corresponding

properties with each other. This can be challenging if not impossible without marking techniques, given the fact that the local information are obtained on areas that are often not larger than 10x10 μm.

PFM and SEM with EDX spectroscopy were chosen to demonstrate how the marking technique can be used to combine different microscopy techniques, and thus acquire information of local dipolar order and chemical composition on selected areas. Results of these investigations will be given in subsequent sections.

4.2 **Marking process**

Commercial copper grids as used in transmission electron microscopy (TEM) for sample support (without a support film) in combination with thin-film deposition were used for marking. In this way, more than 500 areas on a sample can be marked at one time.

First a TEM grid is put on top of the samples surface to act as a shadow mask for a metal thin-film which leaves open areas on the sample surface that are connected in a cross shape manner, and coated square shaped areas. The uncoated areas which usually have sizes of approximately 15x15 μm can be used for imaging. Figure 45a-c illustrates the principle of this method schematically.
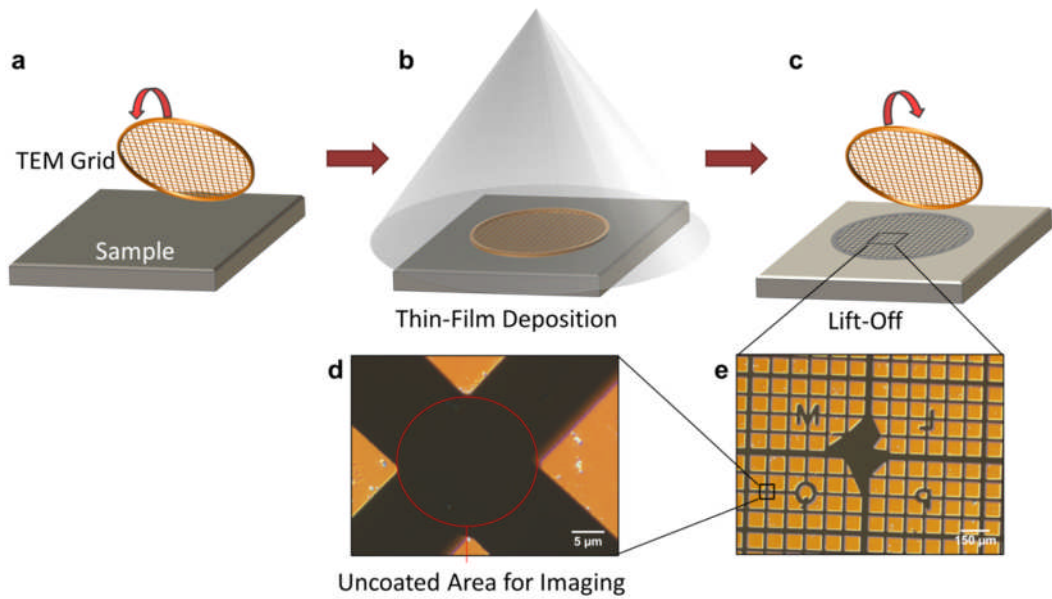
Figure 45 Schematic illustration of the principle of the marking technique. The marking technique involves three steps: **a**, Applying TEM grid to flat sample surface. **b**, Deposition of thin-film. **c**, Lift-off of TEM grid from sample surface, leaving uncoated sample area in shape of the TEM grid. **e**, Light microscopy image showing finder structure on glass slide (note colours are false due to differential interference contrast DIC used for imaging). **d**, Magnification of cross shaped uncoated area. Imaging can be carried out e.g. in the centre of the cross shaped open sample areas. These can be made distinguishable by using an appropriate TEM grid with finder structure (i.e. letters).

TEM grids with appropriate finder structure (letters) enable discrimination of different sample areas e.g. using a conventional light microscopy (see Figure 45d,e). These grids are inexpensive and can be bought in large quantities, which allows single use of each TEM grid. Figure 45e shows a cross-shaped uncoated area in high magnification suitable for imaging.

4.3 **Experimental procedure**

Polycrystalline bismuth ferrite based ferroelectric ceramics with polished surfaces as prepared according to Section 2.2, were used for PFM and SEM investigations. The TEM grid (Maxtaform Reference Finder Grids, Style H7, 400 mesh, Copper, Ted Pella, California, USA) was clamped on the surface of each sample which were then attached to a sample holder. For thin-film deposition, the whole assembly was loaded into the process chamber of an electron beam evaporator Leybold Univex 350 system (Oerlikon Leybold

Vacuum, Cologne, Germany) with sample to source distance 375 mm. Electron beam evaporation of aluminium was carried out under a vacuum of below 1×10^{-6} mbar. Thin-film deposition and thickness were controlled by an automated shutter system in combination with a quartz crystal microbalance. The film thickness was approximately 50 nm.

4.4 **AFM/PFM investigation**

Fig. 2 shows how the technique is employed to image a specific sample area with AFM and PFM.
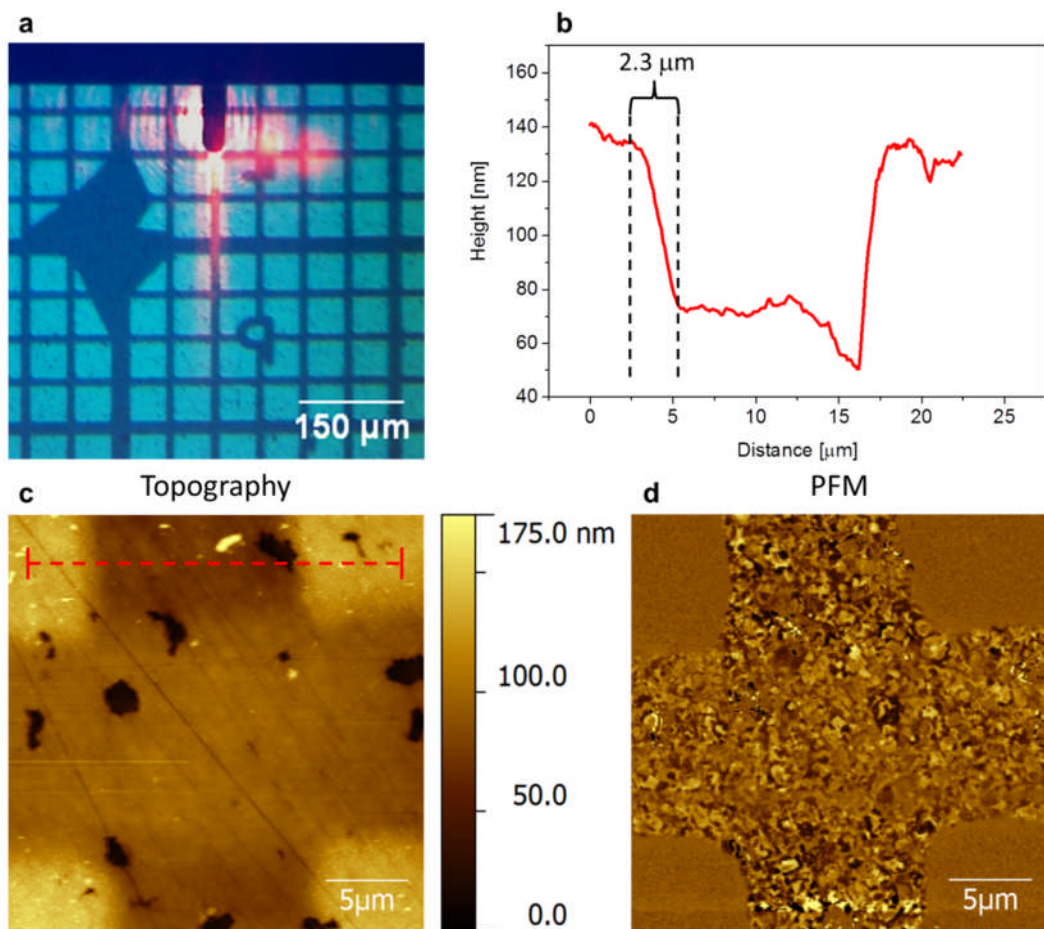
Figure 46 Finding specific sample area with AFM/PFM. **a**, Micrograph taken with the light microscope integrated in the AFM. The cantilever with laser spot reflected from the back side is visible at the top middle, with the AFM tip situated underneath the bottom end of the cantilever. **b**, Cross-section through topography according to red dashed line in **c**. The width of the film edge is approximately 2.3 μm. **c,d**, Topography and corresponding PFM image (X-channel or mixed signal) of cross shaped uncoated area respectively. Note that PFM contrast is only seen in the uncoated areas.

Figure 46a shows how the finder structure can be used to move the AFM tip to the desired free sample area, using an integrated light microscope with low magnification. A simple X-Y-stage which was operated manually using two screws to move the sample relative to the tip was used in this case. Figure 46c and d show topography and PFM images (X-channel or mixed signal) respectively of a cross shaped open sample area. Note that in coated areas (bright in topography) there is no PFM signal, whereas in the uncoated area, the ferroelectric domain pattern of the sample is visible. The low width of the thin-film edge (2.3 μm) visible in the topography cross-section (Figure 46b) according to the red dashed line in Figure 46c, allows accurate localisation of sample areas.

4.5 SEM-EDX investigation

The same localization procedure was also tested for SEM with EDX spectroscopy, which is shown in Figure 47.

SEM BSE-Imaging
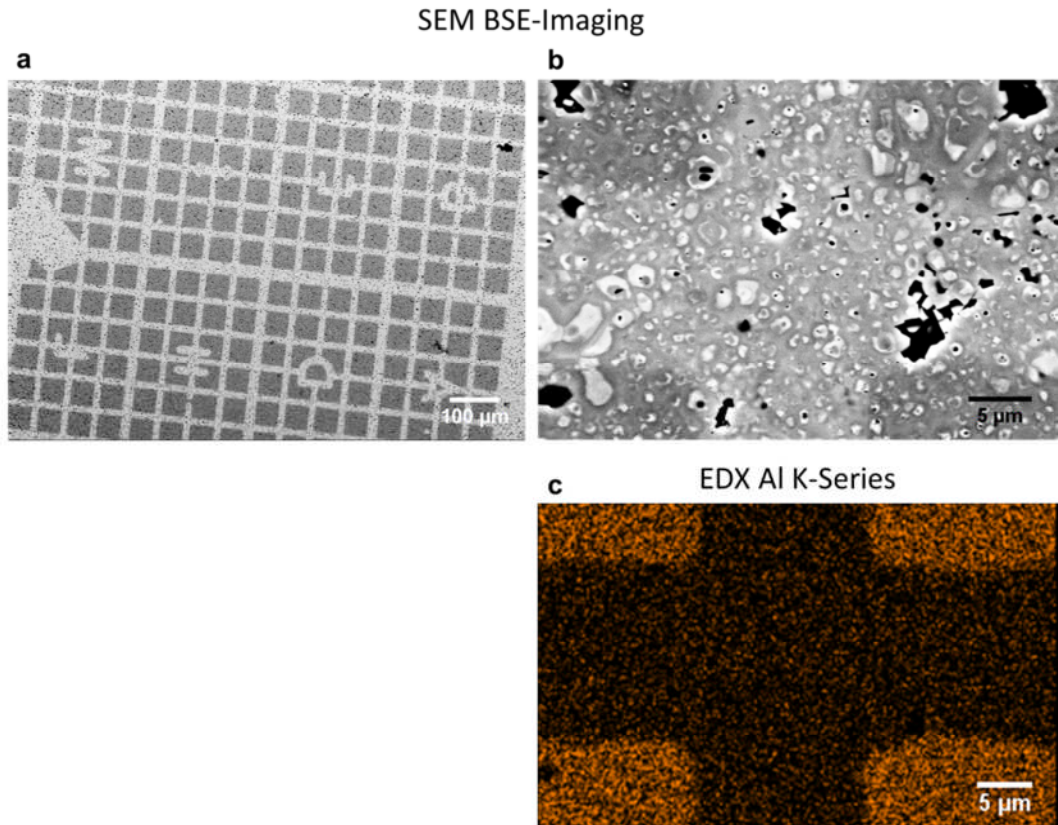
EDX Al K-Series

Figure 47 Finding specific sample area with SEM and EDX. **a**, SEM backscattered electron (BSE) image of larger area showing the finder structure on the sample surface. **b**, Zoomed SEM BSE image of an area suitable for imaging. **c**. Map of EDX Al-K series of the same area as in b showing the elemental distribution of aluminium in this area. As expected, aluminium is found only in coated areas.

Figure 47a shows how coated and uncoated area can be easily distinguished by SEM using backscattered electron (BSE) imaging mode which has an atomic number contrast (z-contrast). Note that in conventional secondary electron imaging, a thin-film would usually not be visible. Furthermore, the BSE mode has the advantage that it causes much less charging on insulating samples, which is the case here. The finder structure (letters) can be used to find exactly the same area as in scanning probe microscopy and vice versa. Figure 47b and c show SEM image and EDX aluminium K series map respectively of a similar area as in Fig. 2c and d. Figure 47c clearly shows that aluminium is restricted only to coated areas. EDX mapping can be also used to distinguish between the coated and uncoated areas in case the average atomic number of film and sample is too similar for discrimination via BSE imaging. Note that bright features in Figure

47b correspond to ferroelectric domains, which are visible in certain cases in SEM BSE imaging.

4.6 Parameters of thin-film deposition

Two different deposition techniques, electron-beam evaporation and sputter-coating with argon plasma, were tested. As expected, it was found that edges were narrower for electron-beam evaporation due to the deposition being almost exclusively in line-of-sight. In contrast, sputter-coating causes more diffuse deposition and thus edges become broader and blurry, although marking is still possible.

Furthermore, several thin-film materials were tested and the best results, in terms of mechanical stability, were achieved for aluminium films. In case of a softer gold film, problems were encountered for AFM imaging. In contact imaging mode which is used for PFM, the film was damaged, while the tip was scanned across it. This resulted in stripe-like imaging artifacts presumably due to the 'smearing' of gold particles across the surface during scanning. However, this was not the case for the aluminium film presumably due to the much harder aluminium oxide layer on the surface.

For deposition of the film, it was found that a flat sample surface is very important to ensure that gaps between grid and sample surface are minimized. If the grid does not lie flat, but in some distance away from the surface, this results in formation of a shadow from the aluminium source to the sample surface. As a result, there exists a grey area between the fully exposed and fully obscured area. This leads to undefined and broad edges between coated and uncoated areas, which is undesirable.

4.7 Conclusions

A simple and inexpensive method for marking individual and distinguishable areas on a sample, using TEM grids in combination with thin-film deposition was successfully implemented. Furthermore, it was shown that it can easily be used to combine microscopy techniques like AFM/PFM, SEM-EDX and light microscopy. Main advantages of the technique are that it is convenient,

inexpensive and that many areas (several hundred, approximately 15x15 μm large) can be marked at the same time on several samples with one thin-film deposition, which makes it suitable for high throughput or batch processing. These features distinguish the technique from other marking techniques like using a focused ion-beam (FIB) [148] which is time consuming and expensive. Nevertheless, the technique could be particularly valuable, when used in junction with e.g. FIB sectioning to obtain a thin lamella of a particular pre-selected area.

In principle, this marking technique can be used for many other microscopy techniques like confocal Raman microscopy or X-ray tomography with the only requirement that coated and uncoated areas need to be distinguishable. Marking of sample areas is especially important on samples, which lack prominent surface features, which might be used for orientation. A finder structure engraved in the TEM grid enables easy distinguishing of individual areas, while the size of marked areas can be varied by choosing a TEM grid with appropriate bar width.

Best results in terms of sharp edges between coated and uncoated areas and mechanical stability of the thin-film were achieved, for an aluminium thin-film (thickness approximately 50 nm) deposited via electron-beam evaporation. This ensured good line-of-sight deposition, while the relatively long sample to source distance presumably is also beneficial. Furthermore, it is important to have a flat sample surface with a close contact between TEM grid and surface to avoid blurry undefined film edges. The film material should be relatively hard which avoids problems with sample handling and imaging artifacts in AFM. In this case, aluminium proved well suitable for this purpose in contrast to gold.

5 $(PbZr_{0.52}Ti_{0.48}O_3)_x$-$(PbFe_{2/3}W_{1/3}O_3)_{1-x}$ solid solution ceramics

5.1   Chapter overview and motivation

As outlined in Section 1.7.5, the system PZT-PFW was reported to show large ME coupling effects, which could however not be reproduced by other groups. Therefore, this system was selected, to further investigate its multiferroic properties. Especially, magnetoelectric coupling should be investigated using PFM under in-situ magnetic field.

5.2   Structural characterisation

Three different compositions, $x = 0.8$, 0.7 and 0.6, of the system $(PbZr_{0.52}Ti_{0.48}O_3)_x$-$(PbFe_{2/3}W_{1/3}O_3)_{1-x}$ (PZT-PFW) were prepared using the procedure as outlined in Section 2.2. X-ray diffraction confirmed formation of perovskite phases with only very minor peaks not belonging to the main perovskite phase as illustrated in Figure 48. However, no impurity phase could be assigned to those minor peaks.
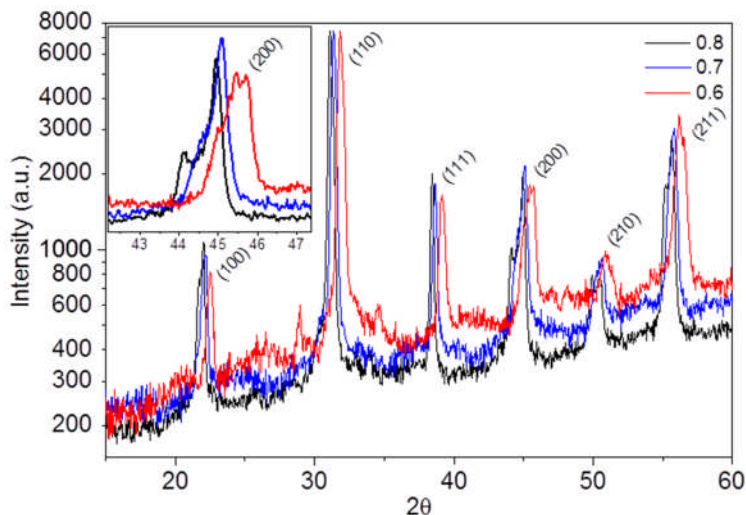
Figure 48 X-ray diffraction pattern (Cu Kα, logarithmic intensity scale) of PZT-PFW ceramics for compositions $x = 0.8$, 0.7, 0.6. Lattice constants decrease gradually for increasing PFW content. Splitting of (200) peak family indicates tetragonal distortion (see inset, linear intensity scale) for all compositions with less pronounced splitting for increasing PFW content as expected from increasing relaxor properties. No major peaks not belonging to the main phase were found.

Since the perovskite crystal structures are not largely distorted from the ideal cubic structure, peaks belonging to the same family e.g. (100) and (001) will be collectively referred to as (100) peak henceforth. For $x = 0.8$ a tetragonal distortion is clearly evident by the splitting of the (200) peak family which is less pronounced in the PFW richer compositions, as expected from the fact that pure PFW exhibits a pseudo-cubic crystal structure. This is in agreement with findings on thin-films by Kumar et al. [96] at least for $x = 0.8$, but not with the rhombohedral structure found by Pajic et al. [94] for $x = 0.8$, 0.7 and 0.6. However, different distortions for nominally same compositions are not surprising, since PZT is at an MPB, where the structure is very sensitive to slight changes in composition.

Neutron diffraction was carried out for $x = 0.6$ in the temperature range between 1.5-550 K. Two structural transitions were observed which are shown in Figure 49.
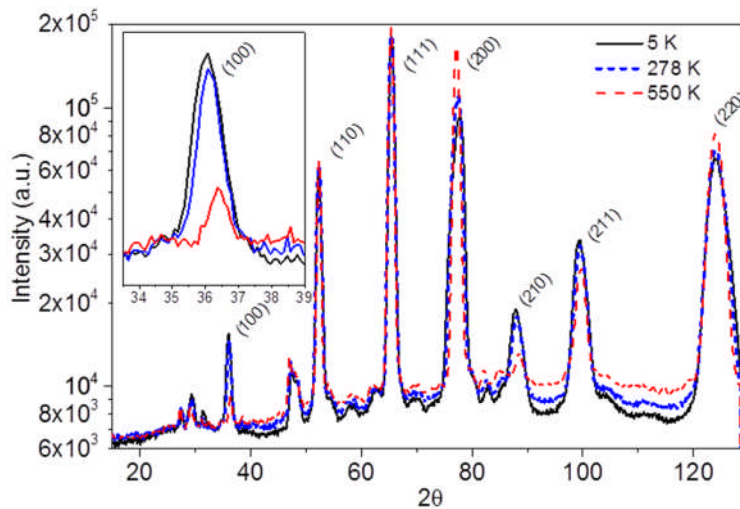
Figure 49 Neutron powder diffraction pattern of PZT-PFW ceramics ($x = 0.6$) as function of temperature ($\lambda = 2.52$ Å, logarithmic intensity scale). Inset shows the (100) peak family. Changes in peak height and widths indicate structural phase transitions.

As temperature increases, a number of peaks decrease considerably ((100), (210), (211)) while other peaks become sharper and more intense ((111), (200), (220)). It should be noted, that the decrease of peak width is not due to thermal strain relief, since this process was reversible under heating and

cooling. It is particularly noteworthy, how the intensity of the (100) peak becomes almost 0 (see inset), while the peak position shifts from lower to higher angles, corresponding to a contraction of the lattice, contrary to what would be usually expected for increasing temperatures. Similar trends were found for other peaks. These facts are emphasized in Figure 50.
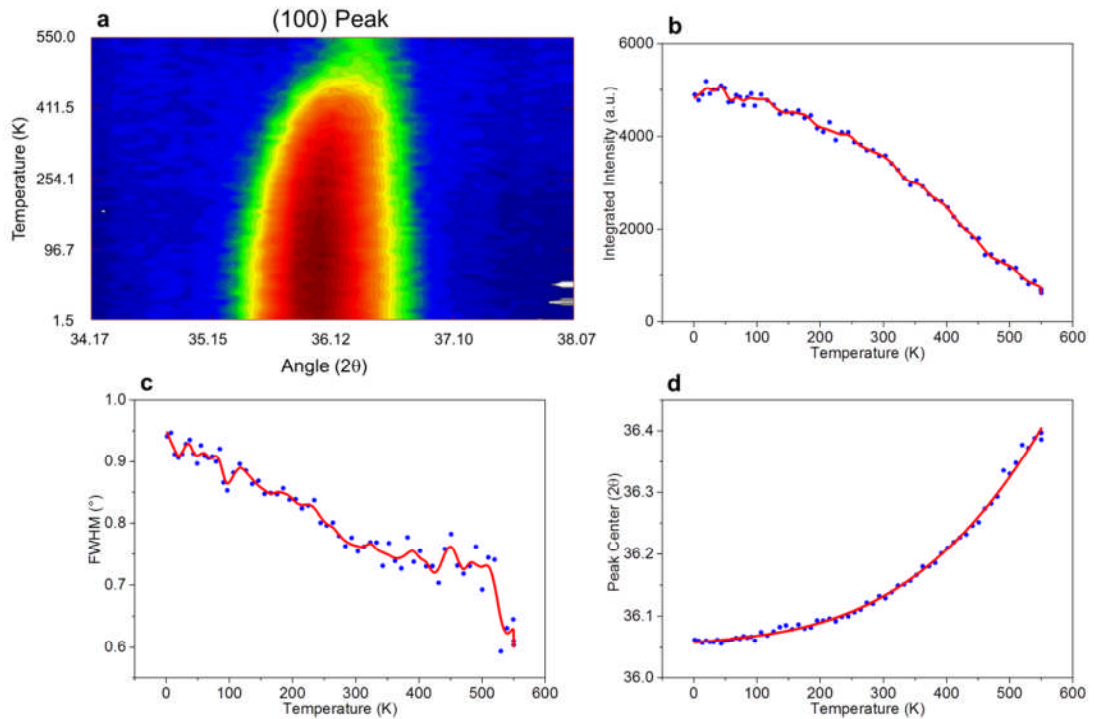
Figure 50 Temperature dependence of the (100) peak family by neutron powder diffraction. **a**, Colour map showing temperature evolution *vs.* bragg angle with intensity represented by colours from red to blue. **b**, Integrated intensity *vs.* temperature. A slower decrease up to approximately 300 K is followed by a more rapid decrease until peak disappears almost completely. The transition at approximately 300 K is also reflected in peak width (**c**) while position of the peak centre increases for higher temperatures and follows a polynomial law (**d**).

Figure 50a displays a false colour map for the temperature dependence of the (100) peak where the temperature is plotted *vs.* the bragg angle and intensity is displayed as colours with decreasing intensity from red>yellow>green>blue. The peak centre *vs.* temperature curve follows a polynomial law.

At 460±5 K there is a structural phase transition which is the Curie transition from ferroelectric to paraelectric, which becomes evident when observing the (200) peak as function of temperature as illustrated in Figure 51.
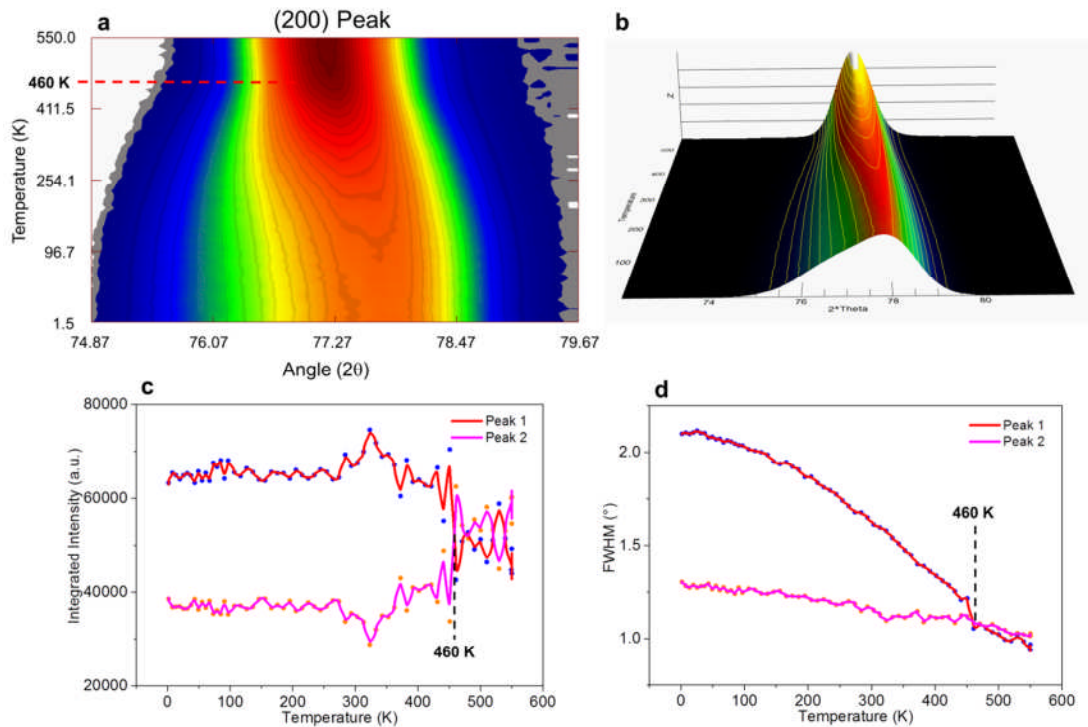
Figure 51 Temperature dependence of the (200) peak family by neutron powder diffraction. **a**, Colour map showing temperature evolution *vs.* bragg angle with intensity represented by colours from red to blue. **b**, 3D representation of (**a**). **c**, Integrated intensity of the two peaks stays relatively constant, until both peaks merge at approximately 460 K, leading to a collapse of the two-peak fitting. **d**, Peak merging is also reflected in the widths of the two peaks.

It becomes clear from observing the temperature evolution in Figure 51a and b that the (200) is split into two peaks at low temperatures which merge at T_C ≈ 460±5 K. Figure 51c shows the fitted intensities of the two peaks which become equal at T_C, while the two peak fitting becomes unstable above this temperature. The transition can be also clearly observed when looking at the peaks' widths (Figure 51d). T_C ≈ 460±5 K is in good agreement with values reported in literature for similar compositions (*x* = 0.8, 0.7; 525, 485 K respectively) [93].

5.3 **Electrical characterisation**

All compositions did show ferroelectric pattern in PFM images as illustrated in Figure 52.
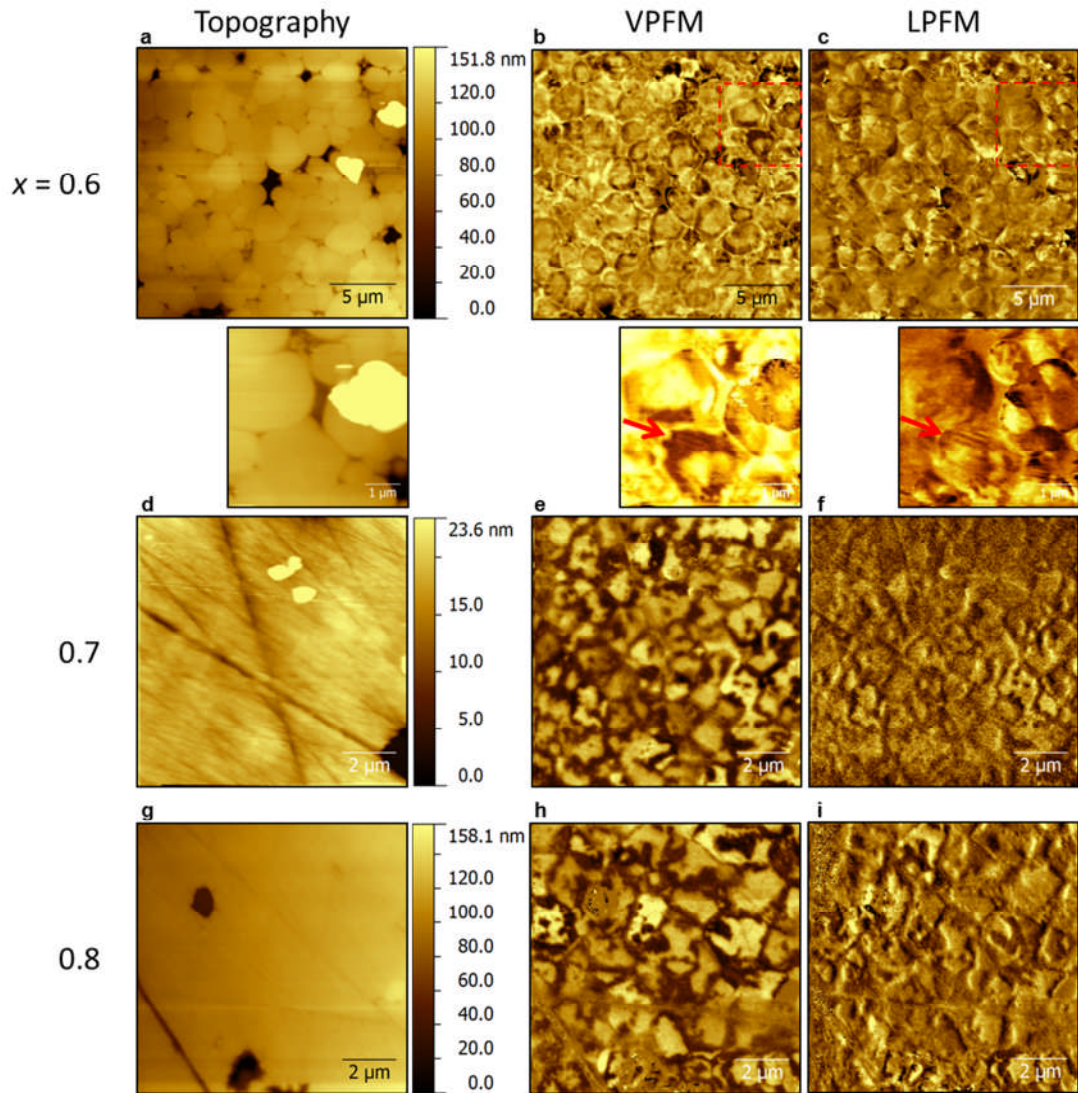
Figure 52 PFM investigation of PZT-PFW ceramics. Topography, vertical PFM (VPFM) and lateral PFM (LPFM) images are shown according to column labels while compositions is according to row labels. $x = 0.8$ and $x = 0.7$ display more pronounced FE domains as $x = 0.6$, which is in line with expectations of more pronounced relaxor properties with increasing PFW content. Stripe-shaped FE domains are found in $x = 0.6$ as indicated by red arrows.

$x = 0.7$ and 0.8 both exhibit relatively similar disordered FE domain patterns. In agreement with our expectations and with X-ray diffraction, their domain patterns are very pronounced as expected for proper ferroelectrics. In contrast, PFM images recorded on $x = 0.6$ exhibit patches of high piezoactivity often located at the edges of grains, which are separated by relatively large areas showing a low and uniform PFM signal (brown areas). This is in line with the fact that $x = 0.6$ is expected to be more relaxor like as

compared to x = 0.7 and 0.8. Nevertheless, very small stripe-like 180° domains can be observed in certain grains, as indicated by red arrows. Note that the contrast was enhanced to make these domains better visible.

Furthermore, a number of PFM under in-situ magnetic field experiments were carried out on all compositions. However, no signs of local ME coupling using PFM under in-situ magnetic field could be found unlike in the related PZT-PFT [67].

5.4 **Magnetic characterisation**

All investigated compositions, x = 0.8, 0.7 and 0.6 did show non-linear hysteretic magnetic behaviour as illustrated in Figure 53.
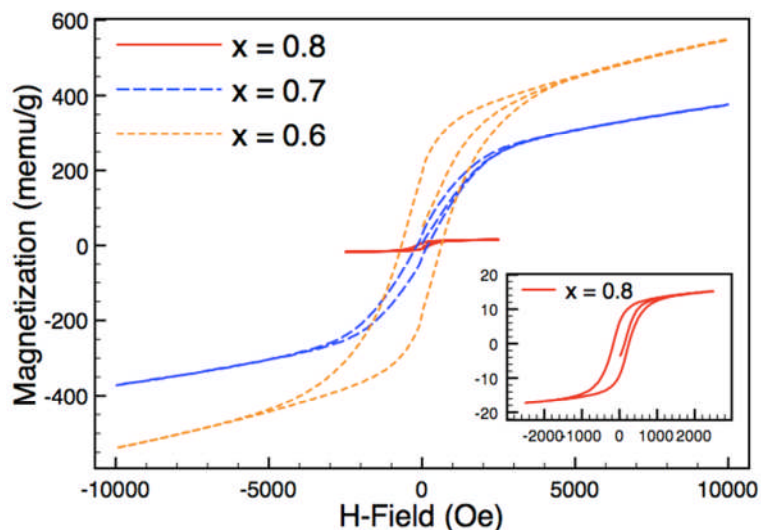
Figure 53 Magnetization vs. magnetic field (*M-H*) loops for all compositions at room temperature. All compositions show non-linear and hysteretic behaviour, although much stronger for x = 0.6 and 0.7 as for 0.8.

As expected, compositions with higher content of Fe exhibit larger spontaneous magnetization.

However, MFM and SEM-EDX investigations of x = 0.6 revealed the presence of a magnetic impurity phase in the material with low content as illustrated in Figure 54.
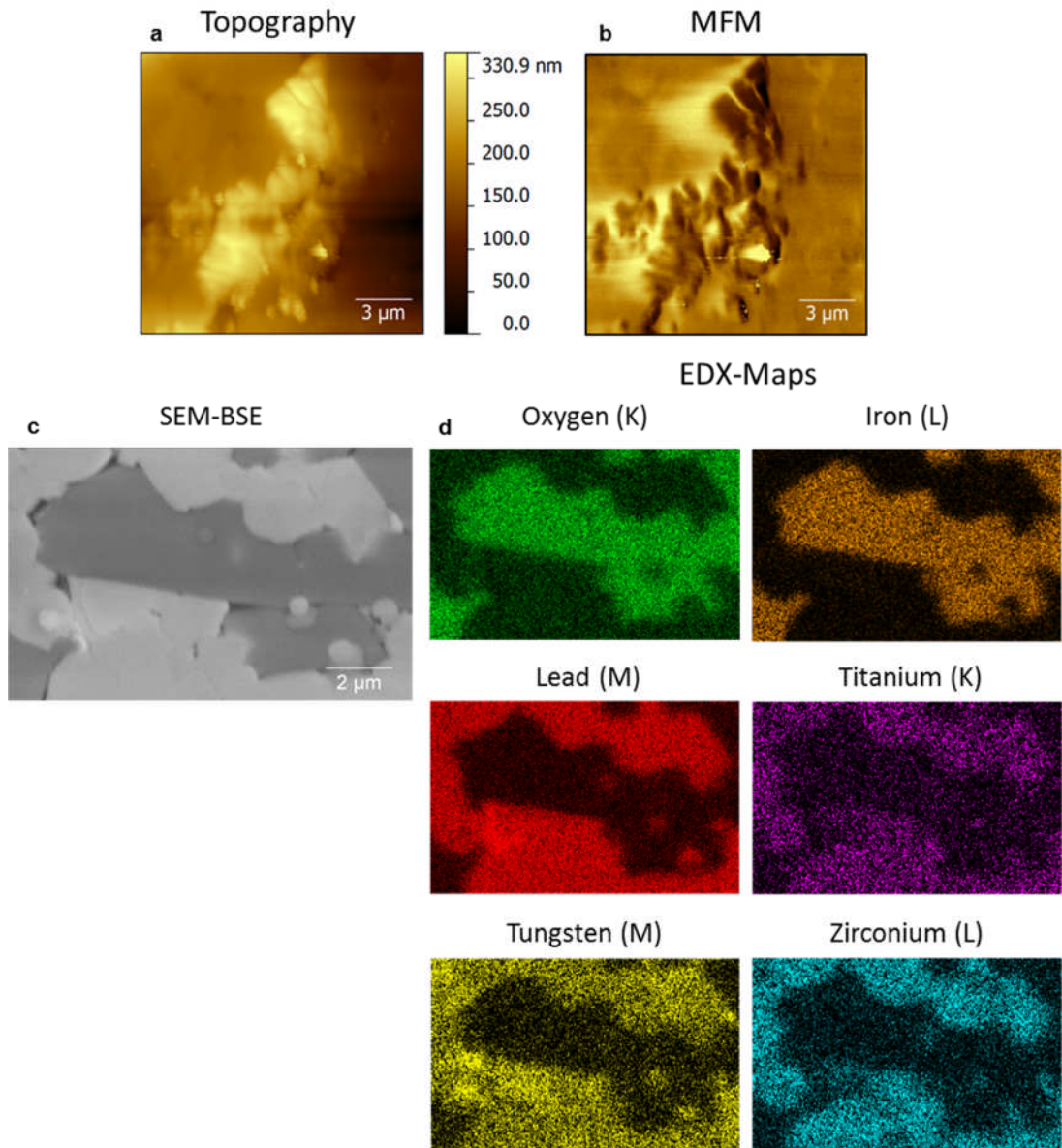
Figure 54 MFM and SEM-EDX images of a typical Fe_3O_4 impurity phase particle. **a**,**b** Topography and MFM (phase) image of an Fe_3O_4 particle exhibiting magnetic stray fields. **c**, SEM micrograph (backscattering detection). Secondary phase particle is easily identified by SEM due to atomic number contrast. **d**, EDX maps showing elemental distribution according to labels. Elemental distribution indicates that the particle has the chemical composition: Fe_3O_4

EDX maps indicate an approximate composition Fe_3O_4 (Magnetite). It is not unlikely, that small amounts of Fe_3O_4 form in the present system, since unreacted $\alpha\text{-}Fe_2O_3$ used as starting material, which is antiferromagnetic itself decomposes at temperatures around 1200°C to form Fe_3O_4. Such high temperatures were reached during sintering. It is also possible that the particles consist of ferrimagnetic $\gamma\text{-}Fe_2O_3$. The calculated atomic ratio of Fe

to O from EDX spectra is not accurate enough to be able to draw a conclusion on the exact composition of the secondary phase, since signals from other elements than Fe and O were relatively large, meaning that not only the impurity phase particle was probed. Judging from XRD, SEM-EDX maps and the relatively low magnetization of PZT-PFW samples, the maximum content of Fe_3O_4 is estimated to be below 1%. Given the fact that Pajic et al. [94] did not observe ferromagnetic behaviour for the above compositions, this might be due to the impurity phase. It is important to note, that these impurity phases are not easily detected using SEM-EDX. They could only be detected using EDX on well-polished samples. When the last polishing step involving colloidal silica had been left out, they were not detectable using EDX (compare Section 3.6).

A technique which is not sensitive to magnetic impurity phases with low content is ^{57}Fe Mössbauer spectroscopy, since signals from all Fe atoms in the sample are obtained which are predominantly not contained within the impurity phase. In fact, in this particular case, where samples have a large concentration of strongly *X*-ray absorbing elements (i.e. Pb), the contribution of Fe atoms from Fe_3O_4 is certainly below the noise level, due to relatively low signal to noise ratio. Spectra at different temperatures for all compositions are shown in Figure 55.
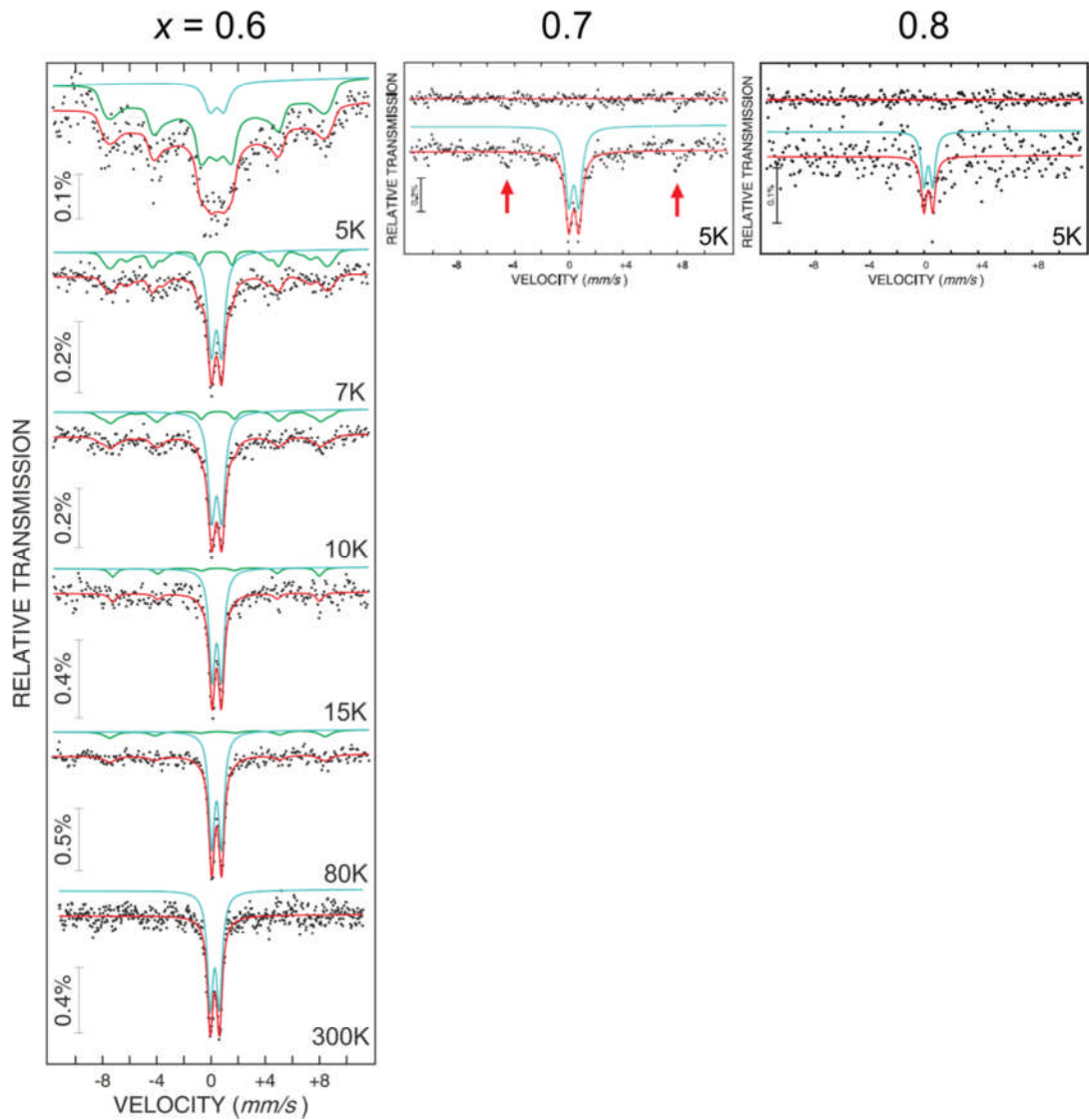
Figure 55 ^{57}Fe Mössbauer transmission spectra at various temperatures for $(PbZr_{0.52}Ti_{0.48}O_3)_x$-$(PbFe_{2/3}W_{1/3}O_3)_{1-x}$ for $x = 0.6$, 0.7 and 0.8 according to labels with: fit to data (—), sextet contribution (—) and doublet contribution (—). Only $x = 0.6$ exhibits blocked magnetic order at low temperatures. Red arrows indicate signs of sextet contributions for $x = 0.7$ which could, however, not be fitted satisfactorily.

Only for $x = 0.6$, there are sextet contributions clearly visible at low temperatures, whereas for $x = 0.7$ there is hardly any sextet contribution present even at 5 K (red arrows indicate signs of sextet contributions for $x = 0.7$ which can, however, not be fitted satisfactorily). For $x = 0.6$ there is a broad sextet and a small doublet contribution present at 5 K. The sextet corresponds to blocked (antiferro)magnetic order of Fe atoms, while the doublet either corresponds to paramagnetic Fe atoms, or to thermally relaxing magnetic regions whose magnetization vector fluctuates faster than

the Larmor period of 5×10^{-9} s for ^{57}Fe nuclei. The fact that sextet and doublet contributions coexist in a certain temperature range up to approximately 80 K, might indicate a blocking process and thus the presence of nanosized magnetic regions. Pajic et al. reported a blocking transition for the same composition but at lower temperature (approximately 8 K) [94]. AC susceptibility *vs.* temperature measurements also exhibit an anomaly at low temperatures as illustrated in Figure 56.
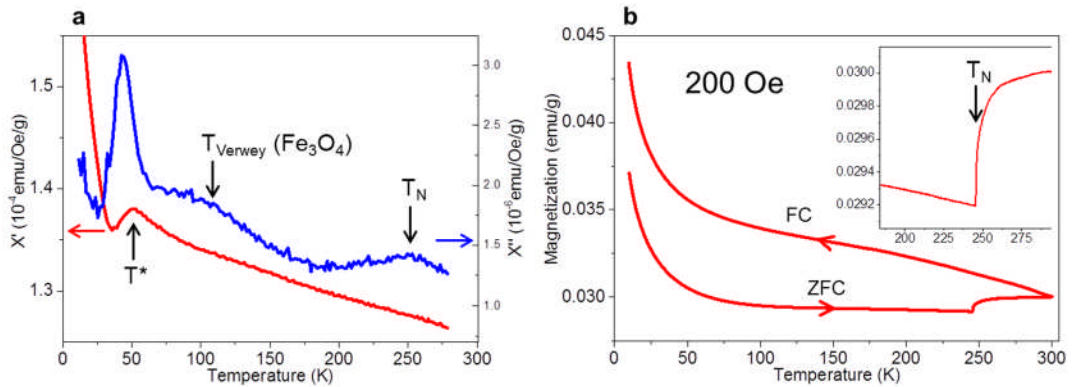
Figure 56 Temperature dependent susceptometry and magnetometry of PZT-PFW ceramics, $x = 0.6$. **a**, Real (χ') and imaginary part of AC susceptibility (χ'') vs. temperature measured at $H_{AC} = 10$ Oe, f = 20 Hz with a DC offset $H = 20$ Oe. **b**, Zero-field cooling (ZFC) and field cooling (FC) magnetization *vs.* temperature curves measured at $H = 200$ Oe. Direction of measurement is indicated by red arrows.

The features observed in AC magnetometry (Figure 56 a) are not expected to be due to Fe_3O_4 particles which do not exhibit transitions in this temperature range, except for the slight maximum in χ'' above 100 K, which might be attributed to the Verwey transition of Fe_3O_4 [149]. Although the maxima close to $T^* \approx 50$ K in the real and imaginary part of the AC susceptibility might indicate a blocking process, this seems unlikely, due to the significantly different transition temperature observed in Mössbauer spectroscopy. In Mössbauer spectroscopy, the transition from sextet to doublet (equivalent areas for both contributions) takes place approximately at 10 K (see also Section 6.7). Since superparamagnetic blocking is a dynamic process which is strongly dependent on the time constant of the used method, a much higher blocking temperature would be expected for Mössbauer spectroscopy as compared to AC magnetometry. This is,

however, not the case. Therefore, it is more likely that this transition is static and thus, is independent of the measurement time constant.

PZT-PFW has a perovskite crystal structure, where Fe atoms are linked by O atoms in a network or clusters fashion, which are interrupted by diamagnetic ions following percolation statistics similar as in the well-studied $PbFe_{1/2}Nb_{1/2}O_3$ (PFN) [40]. These clusters, should exhibit a broad distribution of Néel temperatures, depending on their size, which might explain the Mössbauer spectroscopy and AC magnetometry data between 5 and 80 K.

It is interesting to note that no anomaly around 50 K is visible in the ZFC-FC curves in Figure 56b. This would rather indicate a frequency dependent process. The observed irreversibility (difference between curves), might be attributed to a defreezing process of the magnetization of Fe_3O_4 particles. The ZFC curve contains another feature. A kink close to 250 K might indicate a Néel transition and is supported by a maximum in χ'' at the same temperature. Strangely, this kink is not present when cooling down from higher temperatures in the FC curve. This might be connected to the fact that there is also irreversibility i.e. a difference between ZFC and FC curves. A transition at approximately 250 K is not only found in magnetometry, but also in Neutron diffraction where an antiferromagnetic peak with low intensity, corresponding to a (½½½) peak disappears also at approximately 250 K as illustrated in Figure 57.
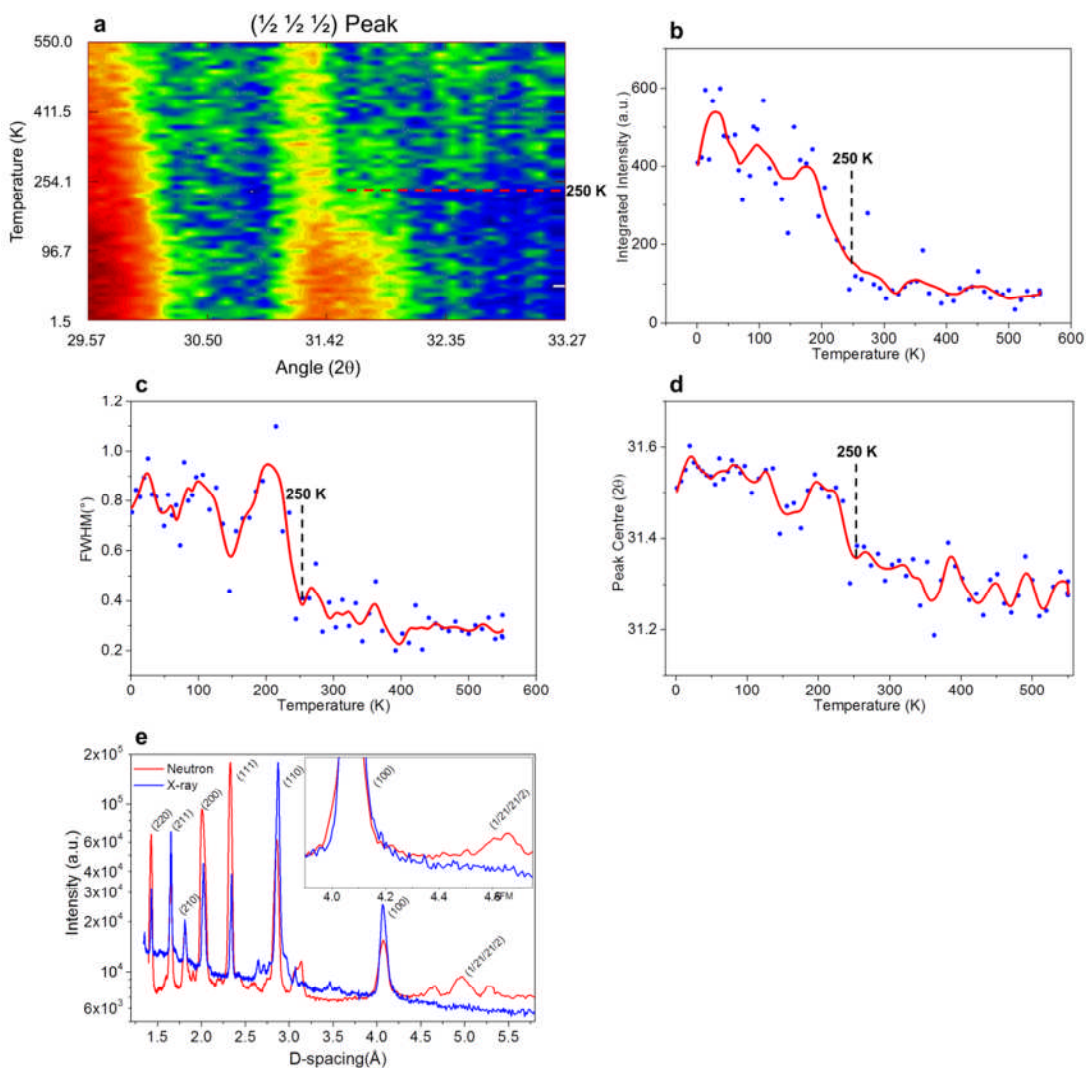
Figure 57 Temperature dependence of the AFM (½½½) peak by neutron powder diffraction. **a**, Colour map showing temperature evolution *vs.* bragg angle with intensity represented by colours from red to blue. Note that apparently there is a weak nuclear bragg peak superimposed with the AFM peak. **b**, Integrated intensity *vs.* temperature showing a decrease to almost 0 at approximately 250 K. This transition is also reflected in peak width (**c**) and position of peak centre (**d**). **e**, Comparison of neutron diffraction with XRD pattern, supports AFM peak (see inset).

In neutron diffraction, there is an additional peak present at low temperatures, with a d-spacing of approximately 4.64 Å corresponding to a doubled d-spacing as compared to the (111) peak at approximately 2.32 Å as visible in Figure 57e. Furthermore, the AFM peak is not present in XRD data. The intensity of the AFM peak drops approximately to 0 around 250 K. Note that there is a very weak nuclear peak superimposed to the AFM peak (see Figure 57a) which is responsible for the non-zero peak intensity above

250 K (see Figure 57b), and the abrupt changes in peak width and centre position as visible in Figure 57c and d. Since the AFM peak belongs to the main perovskite phase, it is not influenced by the magnetic impurity phase. Thus, it is expected that the kink observed in the ZFC curve also stems from the main phase. The Néel transition at 250 K might indicate that there are larger magnetic regions present corresponding to the AFM peak. However, these regions could only contain a small part of the total Fe, since they are not visible in Mössbauer spectra. When considering the overall amount of Fe in the material, a low T_N around 50 K could be expected. However, in order to have a $T_N \approx 250\pm10$ K these regions should have an increased local concentration of Fe corresponding to a composition close to $x = 0.15$ according to Pajic et al. [94]. Furthermore, a blocking transition around 50 K is not supported by neutron diffraction, since an additional broad AFM peak would be expected at low temperatures, corresponding to blocked magnetic nanoregions. Therefore, diluted clusters with a broad distribution of Néel temperatures are the most likely reason for the observed anomaly at around 50 K.

5.5 Conclusions

Three different compositions of PZT-PFW with $x = 0.8$, 0.7 and 0.6 were successfully prepared and characterized structurally, electrically and magnetically. $x = 0.6$ was characterized in more detail by neutron diffraction as a function of temperature. The ferroelectric Curie transition is at 460 K, there seems to be another structural phase transition at approximately 300 K as reflected in decreasing intensities of certain peaks (e.g. (100)). This might be due to a change of the symmetry.

All compositions showed FE domain pattern. However, PFM images for $x = 0.6$ indicates partial relaxor properties in contrast to $x = 0.8$ and 0.7 as expected from increased PFW content. No local ME coupling effects could be observed using PFM under in-situ magnetic field.

Although all compositions exhibited weak ferromagnetic behaviour in *M-H*-loops, this might be actually due to Fe_3O_4 secondary phases as observed by SEM-EDX and MFM. It is important to note, that these secondary phase

particles were difficult to detect. They were not revealed in XRD measurements and also not in SEM-EDX measurements carried out on samples with incomplete polish. Only after carrying out a final polishing step involving colloidal silica nanoparticles (see Section 2.2.3 and 3.6) was it possible to detect them. The last step is very important since the sample surface is slightly etched at this stage, which results in a pronounced height difference between impurity phase and the rest of the sample, if mechanical and chemical stability towards the alkaline environment are sufficiently different for the two phases, which was the case in this example (a further example will be given later, see Section 6.4.2). When this is the case, the particles can be easily identified via SEM, AFM or even light microscopy. Therefore, the importance of the last polishing step, also in terms of image quality in PFM (see Section 3.6), cannot be overstated.

Of all investigated compositions, only $x = 0.6$ seemed to show inherent magnetic properties. Two different characteristic magnetic species seem to be present. There exist network like magnetic cluster of Fe atoms sharing an O neighbour atom which follow percolation statistics. They are characterized by a gradual transition observed in Mössbauer spectroscopy and peaks in AC susceptibility around 50 K. This temperature is in good agreement to the expected T_N according to the relatively low overall Fe concentration of the sample. A blocking transition in this temperature range as found by Pajic et al. could not be confirmed [94].

The second magnetic species is characterized by a kink in the ZFC curve together with a weak AFM peak observed in temperature dependent neutron diffraction. These presumably correspond to regions of higher Fe concentration with approximately composition $x = 0.15$ corresponding to their high $T_N \approx 250\pm10$ K [94]. However, these regions seem to contain only a small amount of the total Fe, since they are not visible in Mössbauer spectra, which is in line with the low intensity of the AFM peak.

Further experiments are necessary to support the above conclusions. Measurements should be repeated on exactly the same samples e.g. for Mössbauer spectroscopy and magnetometry, to exclude any influence from slight variations in sample preparation e.g. during sintering. Furthermore,

Frequency dependent at different DC fields AC susceptibility measurements should be carried out to try to investigate especially the differences between DC magnetometry and AC susceptometry while differential scanning calorimetry (DSC) could further support magnetic transitions.

6 $(BiFe_{1-x}Co_xO_3)_{0.4}$-$(Bi_{1/2}K_{1/2}TiO_3)_{0.6}$ solid solution ceramics

6.1   Chapter overview and motivation

This chapter contains the main experimental results regarding ME coupling and deals with the system $(BiFe_{1-x}Co_xO_3)_{0.4}$-$(Bi_{1/2}K_{1/2}TiO_3)_{0.6}$. The system $(BiFeO_3)_{1-x}$-$(Bi_{1/2}K_{1/2}TiO_3)_x$ had been previously studied by Bennett et al. as outlined in Section 1.7.4. It was found that the composition with $x = 0.4$ lies approximately on a morphotropic phase boundary which results in highest values for the (converse) piezoelectric coefficient and saturation polarization compared to other compositions [87]. Doping with Co was first carried out to enhance ferroelectric long-range order. However, it was also expected that Co doped compositions would be multiferroic, due to the similarity to multiferroic $BiFe_{1-x}Co_xO_3$ (BFC) (see Section 1.7.2).

Almost all experiments presented in this chapter were carried out on the composition $(BiFe_{0.9}Co_{0.1}O_3)_{0.4}$-$(Bi_{1/2}K_{1/2}TiO_3)_{0.6}$ (except where stated otherwise) which for simplicity shall be referred to as BFC-BKT, while $(BiFeO_3)_{0.4}$-$(Bi_{1/2}K_{1/2}TiO_3)_{0.6}$ will be referred to as BF-BKT henceforth.

This chapter will start with investigations of the material's macroscopic crystal structure and electrical properties, followed by a detailed investigation of its magnetic structure and of small multiferroic clusters (MFC) found in BFC-BKT. Subsequently, experiments on local ME coupling will be presented, before concluding the chapter with investigations of magnetic nanoregions (MNR).

6.2   Structural characterisation

Structural characterisation of BFC-BKT ceramics is presented in Figure 58.
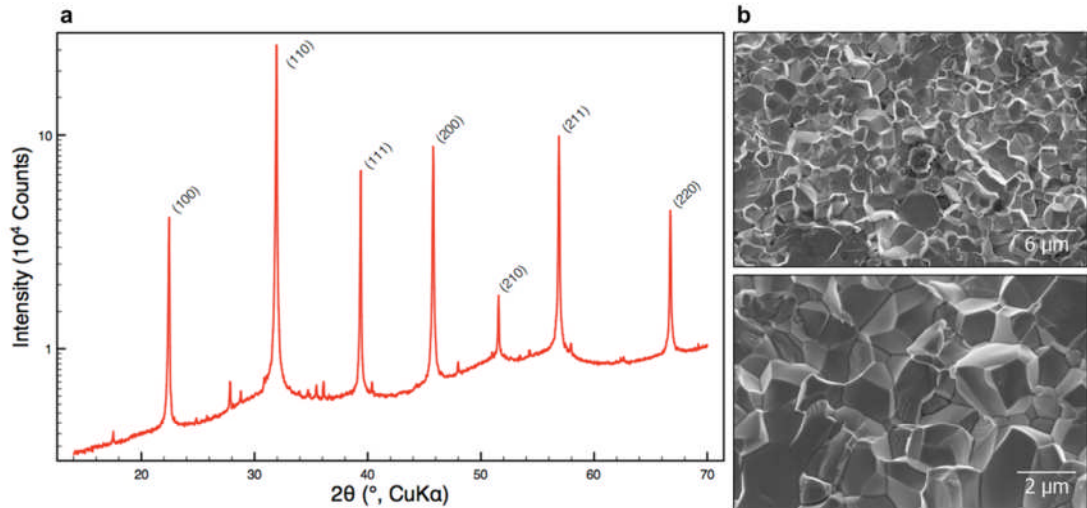
Figure 58 Structural characterisation of BFC-BKT ceramics. **a**, Powder *X*-ray (Cu Kα, logarithmic intensity scale) diffraction pattern indicates a single-phase material. Diffraction peaks due to Cu Kα2 radiation were removed electronically. **b**, SEM images of fractured pellets with magnifications of 10000 (top) and 30000 (bottom).

A powder *X*-ray diffractogram taken from a sintered and crushed pellet (Figure 58a) reveals a pseudo-cubic macroscopic crystal structure as for $(BiFeO_3)_{1-x}$-$(Bi_{1/2}K_{1/2}TiO_3)_x$ (see Section 1.7.4). Only very minor diffraction peaks not belonging to the perovskite structure are visible, which could not be attributed to a certain crystallographic phase. Thus the material consists almost exclusively of one crystallographic phase with very minor impurity phases.

SEM images of a fractured ceramic pellet in Figure 58b show the grain structure with grain sizes varying between 0.8 - 4 μm and an average grain size of 1.81 μm, which was determined by a linear intercept method. This is a normal grain size for a ferroelectric ceramic. Ceramic samples were dense with an average geometrical density is 6.519 g/cm^3 which is slightly lower (approximately 2%) than that of BF-BKT. Consistently, SEM images indicate relatively low porosity as expected for a dense ceramic.

6.3 **Electrical characterisation**

Characterisation of electrical properties is essential for a multiferroic. Results are presented in Figure 59.
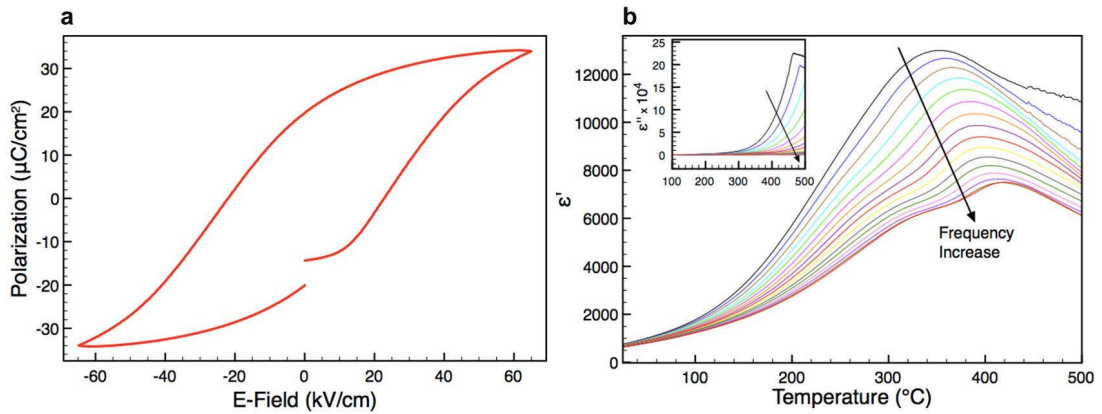
Figure 59 Electrical characterisation of BFC-BKT ceramics. **a**, Polarization *vs.* electric field loop at 1 Hz and room-temperature. **b**, Permittivity *vs.* temperature curves at logarithmically equidistant frequencies ranging from 1 kHz to 1 MHz. Frequency dispersion indicates relaxor ferroelectric properties. The inset shows an analogous plot of the imaginary part of the permittivity.

The polarization *vs.* electric field loop in Figure 59a proves ferroelectricity at room-temperature. Although the loop is not completely saturated, values for remanent and saturation polarizations are 19.9±0.05 and 33.9±0.05 μC/cm^2, respectively, with a coercive-field of 22.4±0.05 kV/cm. Permittivity *vs.* temperature curves taken at various frequencies (Figure 59b) reveal a relaxor behaviour with frequency dispersion on the left side of the relaxation peak between 350 to 400 °C. Non convergent curves on the right hand side of the peak from 400 to 500 °C, are attributed to conductivity effects due to a relatively high conductivity in this temperature range which is indicated by relatively high imaginary part of permittivity ε'' in the inset of Figure 59b.

As outlined in Section 1.4.3, it is assumed that random electric-fields in charge-disordered BFC-BKT give rise to PNR, which freeze into a dipolar cluster glass state exhibiting SPNR as introduced in Section 1.4.4 on cooling to below the low-*f* peak temperature, $T \approx 300$°C. Above an external electric field, $|E| > 20$ kV/cm (Figure 59a), the glassy disorder is broken while all dipolar moments are aligned at saturation. This picture is supported by PFM investigations as shown in Figure 60.
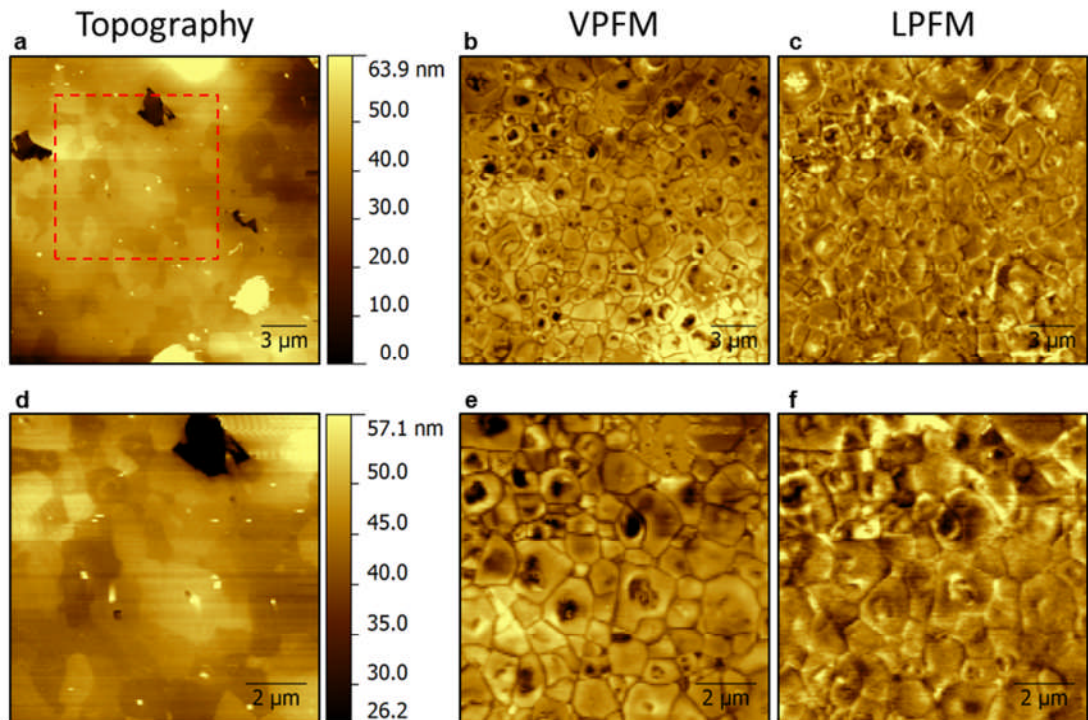
Figure 60 PFM investigation of BFC-BKT ceramics. Topography, vertical PFM (VPFM) and lateral PFM (LPFM) images are shown according to column labels. Images in the bottom row (**d**,**e**,**f**) are zoomed from top row images (**a**,**b**,**c**) according to red dashed rectangle in **a**. A non-ergodic relaxor state is confirmed due to the presence of SPNR which occur as bright and dark spots in VPFM and LPFM images. These are presumably surrounded by a dipolar matrix containing PNR.

PFM images reveal the dielectric structure where distinct boundaries are clearly visible at grain boundaries as can be seen by comparing VPFM images with the grain structure from topography images. The dark lines along grain boundaries visible in VPFM, correspond to a higher piezoresponse with polarization facing downwards while brown areas inside grains correspond to areas with low piezoresponse. Often, dark areas are found in the centre of grains which can be best seen in the zoomed image in Figure 60e. These areas correspond to SPNR. The areas exhibiting low piezoresponse presumably contain dynamic PNR which fluctuate fast at measurement conditions and thus do not result in a net polarization. Some of the SPNR also exhibit a large in-plane polarization component as visible in LPFM images (Figure 60c and f). It is striking that the region in the bottom right corner of Figure 60b has much higher positive piezoresponse than

other regions. However, it is not yet clear what might be the reason for this behaviour.

6.4 Magnetic characterisation

6.4.1 Multiferroic clusters

Beside dielectric properties, another key aspect of multiferroics are their magnetic properties which are characterized subsequently. For better understanding, microscopic results will be presented first.

MFM measurements were carried out to investigate the microscopic magnetic structure of BFC-BKT. Isolated magnetic features were found which are displayed in Figure 61. The MFM images presented in Figure 61b was recorded using an AFM by Attocube (see Section 2.5.7.
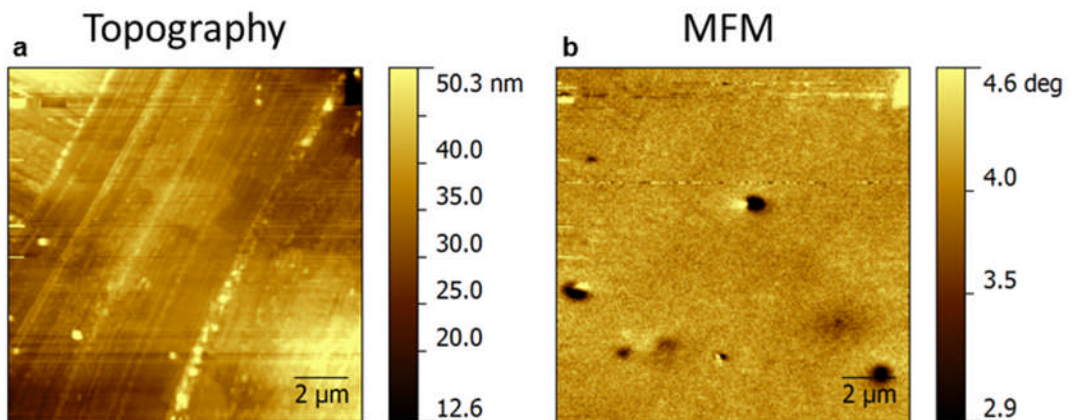
Figure 61 MFM investigation of BFC-BKT ceramics. Magnetic features are visible in the MFM phase image (**b**). No particles are associated to these features (see **a**). Stripe features in topography are due to contamination of the surface.

These magnetic clusters exhibit strong stray fields visible in MFM so it is assumed that they correspond to ferrimagnetic regions due to Fe-Co ferrimagnetism. A weak ferromagnetic behaviour would for instance not result in such strong MFM signals. As outlined in Section 2.5.3 it is essential in MFM to exclude possible artifacts e.g. due to surface charges. For this purpose, one cluster was switched using an external magnetic field which was applied ex-situ (not during measurement and away from the tip) so that the tips magnetization would remain unchanged. This is shown in Figure 62.
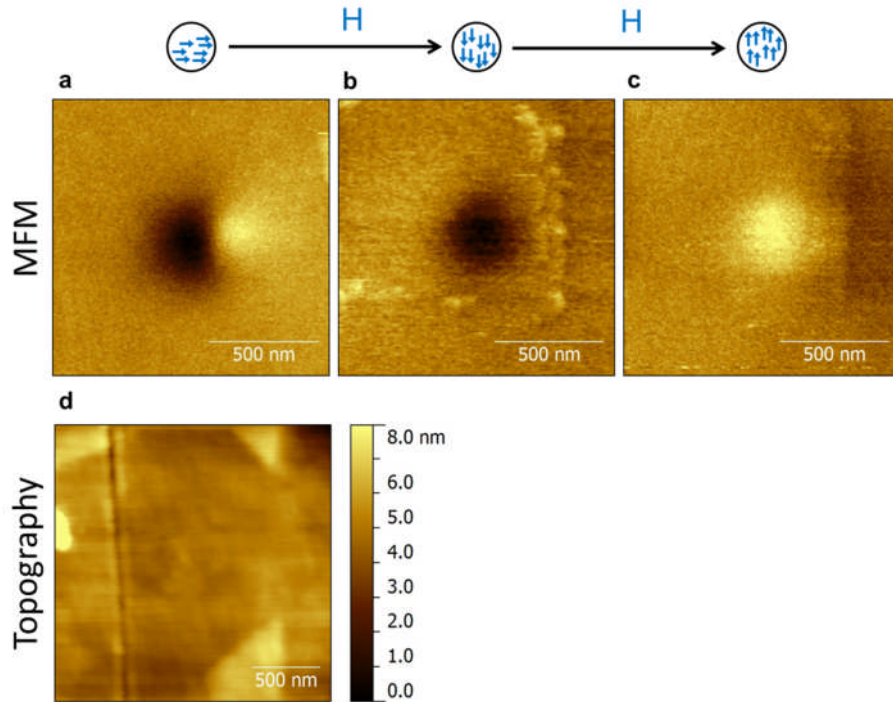
Figure 62 Switching of magnetic cluster. **a**,**b**,**c**, MFM images of the same magnetic cluster, before (**a**) and after ex-situ switching with out-of-plane magnetic fields of ±0.48 T (**b**,**c**) as indicated by blue arrows. Symbol above images, represent single magnetic domains according to the dipolar magnetic MFM response. **g**, Topography showing a flat sample surface in the relevant area.

Figure 62a shows a magnetic dipolar response as for a single domain particle, with magnetization along an in-plane orientation as illustrated above the image. As can be seen in Figure 62b and c, the MC was switched by out-of-plane magnetic fields ±0.48 T. Thus it was proven that the feature is in fact magnetic. Furthermore, there is no strong topography feature associated to the cluster as illustrated in Figure 62d.

The area of the magnetic cluster shown in Figure 62 was also investigated using PFM which revealed the presence of an SPNR with similar size and shape being congruent to the MC which is illustrated by MFM and PFM images in Figure 63.
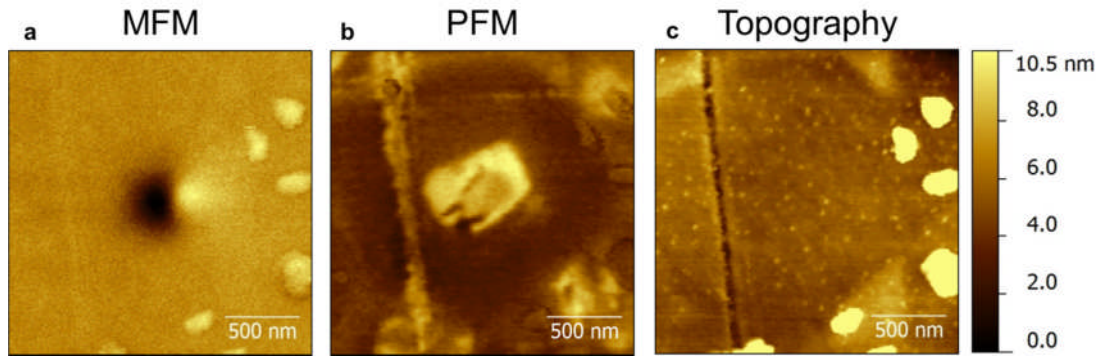
Figure 63 Multiferroic cluster in BFC-BKT ceramics. **a**, MFM images of the same MC as in Figure 62 with congruent SPNR shown in **b**. Note that bright features at the right and bottom edge of **a** are artifacts due to topography features (see **c**).

This means that the feature does not only exhibit strong magnetization but is also ferroelectric. It was found that this is the case for every magnetic cluster that was investigated and we will thus refer to them as *multiferroic clusters* (MFC) henceforth. This discovery is very important, since a single-phase material being ferroelectric and ferrimagnetic, has not yet been directly observed to the best of the author's knowledge. It is all the more interesting, since the multiferroic cluster exists at room-temperature.

But what might be the origin of the MFC? It is suspected that the ferrimagnetic order originates from a higher local concentration of Co and Fe in BFC rich chemical clusters in the BFC-BKT ceramic system. Due to the higher concentration of BFC, an SPNR presumably forms in the same region as an 'island' of long range ferroelectric order within a matrix of disordered PNR, since the BFC component is the one which tends to establish long range ferroelectric order. In contrast, the BKT component induces relaxor properties which was observed in the system $(BiFeO_3)_x$-$(Bi_{1/2}K_{1/2}TiO_3)_{1-x}$ where the BKT richer compositions exhibit pseudo-cubic structures and pronounced relaxor ferroelectric properties (see Section 1.7.4). Therefore, a higher concentration of BKT is expected in the matrix surrounding the MFC.

An idealized crystal structure as expected for the MFC is illustrated in Figure 64b, which shows ferrimagnetic order of Fe^{3+}- and Co^{3+}- ions with net magnetic moment μ and polarization P due to off-centred B-site ions.
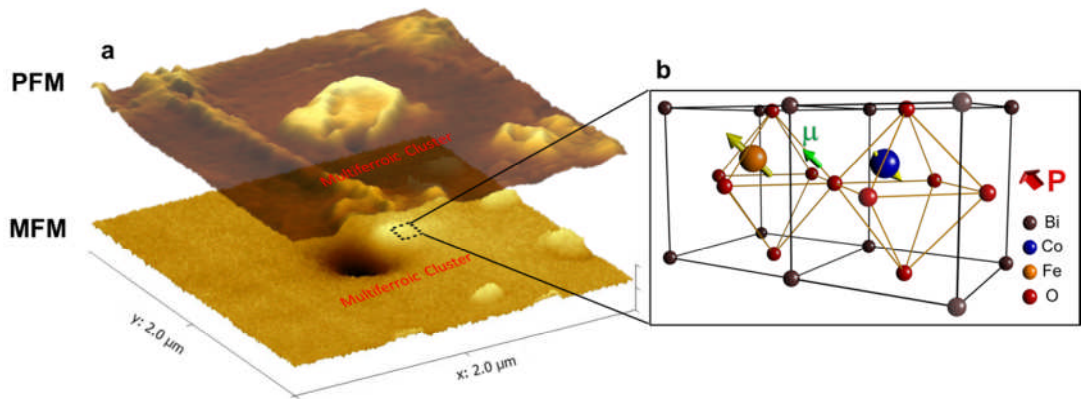
Figure 64 Proposed structure of MFC. **a**, 3D representation of the same MFC as in Figure 63. MFM image (bottom) overlaid with the PFM image of the exact same sample area. **b**, Idealized crystal structure of the 'multiferroic' cluster schematically illustrating the ferrimagnetic order of Fe^{3+} and Co^{3+}- Ions with net magnetization μ and polarization P along the (111) direction.

Note that the above crystal structure representation does not display reality truthfully but is idealized to illustrate the aforementioned facts more clearly.

6.4.2 Microanalysis of magnetic phases

Beside MFC, another magnetic phase with a low content was found using MFM in the form of micrometer-sized particles. Later, it will be shown that these are $CoFe_2O_4$ particles (Figure 66). A typical particle is shown in the top row images of Figure 65.
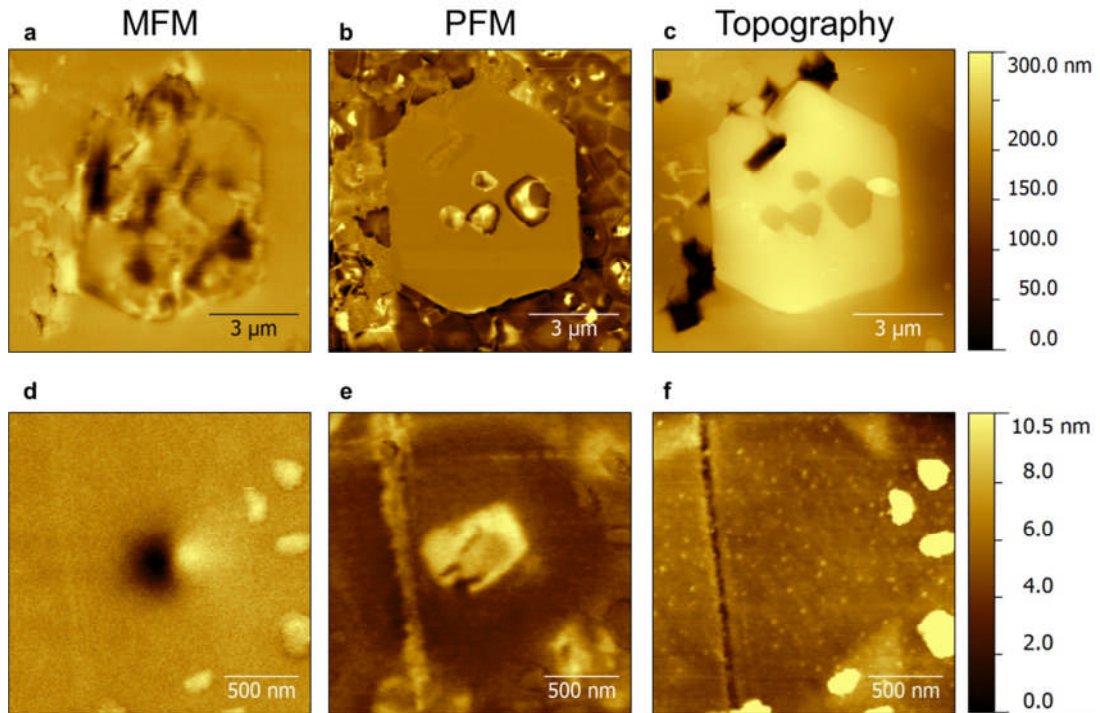
Figure 65 MFM and PFM images of a CoFe$_2$O$_4$ impurity phase particle (top) and of an MFC (bottom). **a,** MFM (phase) image of a typical CoFe2O4 particle showing magnetic structure. **b**, PFM image indicates that the particle is not FE. It can be clearly distinguished from the main perovskite phase in topography (**c**). For comparison, the same images as in Figure 63 are shown. MFC can be easily distinguished from CoFe$_2$O$_4$ particles, since they are smaller, ferroelectric and are level with the rest of the sample in contrast to CoFe$_2$O$_4$ particles.

The MFM image (Figure 65a) reveals that the particle has a magnetic structure, while it is clearly not FE since it lacks any PFM contrast (Figure 65b). In contrast, the surrounding matrix is FE but not magnetic whereas the MFC is both ferroelectric and magnetic. Furthermore, the CoFe$_2$O$_4$ particle can be clearly distinguished from the matrix by topography since it 'sticks out' of the sample by a few hundred nanometres, presumably due to larger mechanical hardness as compared to the matrix which results in a lower polishing rate during sample preparation. This was observed for all investigated CoFe$_2$O$_4$ particles. In contrast, the MFC, cannot be distinguished from the rest of the material by topography as previously mentioned and thus must have very similar mechanical properties. Therefore, the MFC presumably has a similar perovskite-type crystal structure as the main perovskite phase. Of course, due to the fact that it is FE, we also expect a perovskite structure for the MFC. Nevertheless, we will

refer to the relaxor ferroelectric material that surrounds the MFC as 'matrix', although it is expected to have a very similar crystal structure as the MFC.

The same particle as in Figure 65 was investigated using SEM-EDX as illustrated in Figure 66.
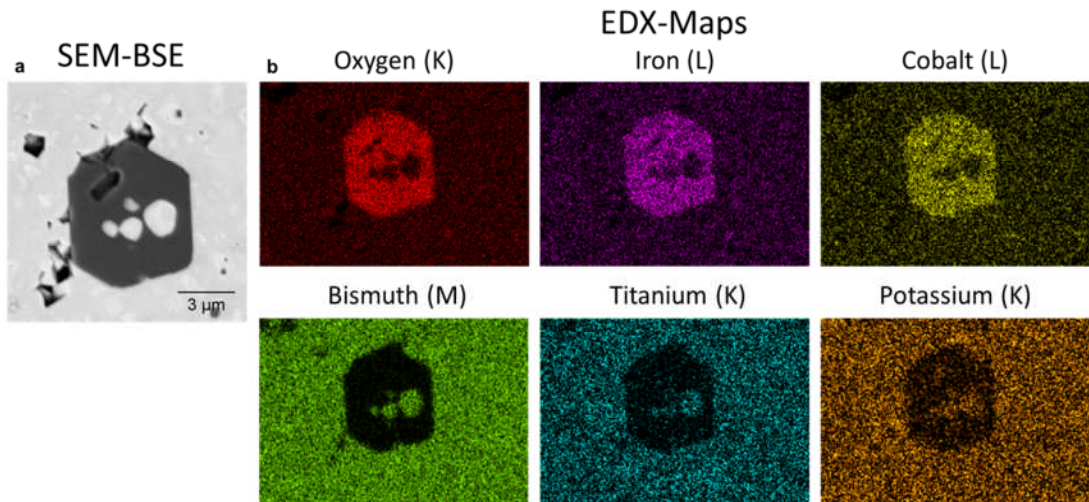
Figure 66 SEM-EDX investigation of magnetic secondary phase particle. **a**, SEM micrograph (backscattering detection). Secondary phase particle is easily identified by SEM due to atomic number contrast. **b**, EDX maps showing elemental distribution according to labels. Elemental distribution indicates that the particle has the chemical composition: $CoFe_2O_4$.

The particle can be easily distinguished from the matrix due to the atomic number contrast of the BSE detection mode (see Section 2.3.2) and due to the higher concentration of O, Fe and Co and the lack of Bi, Ti and K. This suggests a rough chemical composition of $CoFe_2O_4$. From larger EDX-maps the volume content of the $CoFe_2O_4$ particles was estimated to be below 1%. Since the MFC are expected to have a different chemical composition as the matrix, it was also tried to resolve these differences using SEM-EDX. Figure 67 shows SEM-EDX maps region containing the MFC as presented in Figure 63.
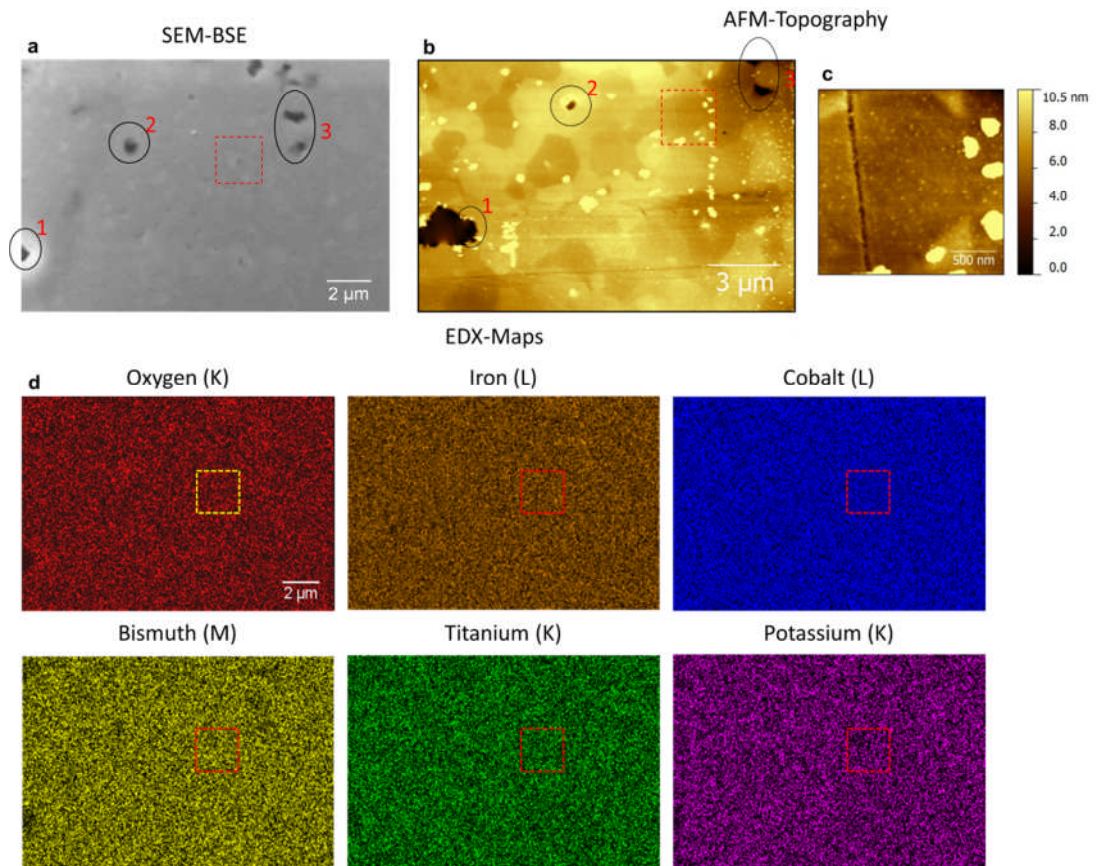
Figure 67 SEM-EDX investigation of an MFC. **a**, SEM micrograph (backscattering detection). Area which contains MFC is marked by dashed rectangle which can be identified by comparison of features in **b** and **a** (marked by black circles). For identification of MFC area, **b** and **c** can be compared. **d**, EDX maps showing elemental distribution according to labels. No chemical inhomogeneity is found for the area of the MFC.

The MFC is contained in the region which is marked by the dashed rectangles which can be identified by comparing features in AFM topography images Figure 67b and c to features in Figure 67a. The MFC is not distinguishable from the rest of the material by EDX which means that both must have a very similar chemical composition. The fact that the MFC could not be resolved by SEM-EDX is attributed to a lack of sensitivity and spatial resolution. Therefore, time-of-flight secondary ion mass spectrometry (TOF-SIMS) was employed, which combines an extremely high elemental sensitivity (in the range of ppm and below) with high lateral resolution as outlined in Section 2.3.3.

Results of SIMS mapping with Bi ion bombardment and positive secondary ions, are presented in Figure 68.
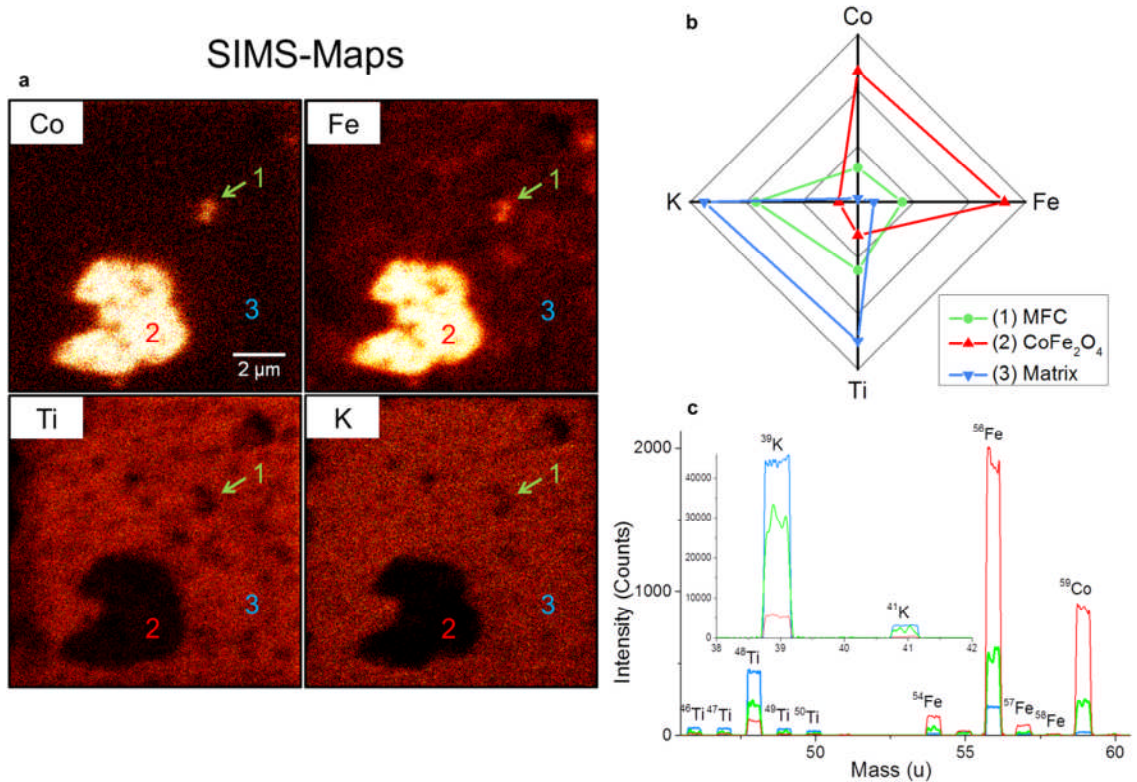
Figure 68 Secondary ion mass spectrometry (SIMS). **a**, Maps of elemental distribution according to labels showing multiferroic cluster (MFC, 1), $CoFe_2O_4$ secondary phase particle (2) and matrix (3). Note that Bi signals could not be analysed since a Bi-ion beam was used as probe. Shape and size of the MFC are in good agreement with MFM and PFM measurements. **b**, Radar chart illustrating relative elemental intensities of the three areas according to mass spectra shown in **c**. **c**, Mass spectra of the three areas showing all relevant mass peaks for the displayed elements. Elements could be assigned to mass peaks due to isotope pattern. As expected, the MFC has an increased Fe and Co content as compared to the matrix but lower K and Ti content. In comparison, the $CoFe_2O_4$ particle has a much higher Fe and Co content than the MFC.

All relevant elements could be identified without problem according to their isotope pattern (see Figure 68**c**). Maps of elemental composition confirm the existence of Co and Fe rich regions as proposed above.

The maps (Figure 68a) show an area which contains an MFC (marked by green arrow, 1) and a $CoFe_2O_4$ secondary phase particle (2). As expected, the MFC exhibits a higher concentration of Co and Fe, and lower concentration of K and Ti than the surrounding matrix as visible by bright and dark spots in the respective elemental maps. Note that dark spots occurring in all images (*e.g.* top right corner) correspond to pores. The size of approximately 1 μm and the oval shape of the MFC are in good

agreement with MFM and PFM measurements. The large feature marked by 2 is identified as a $CoFe_2O_4$ particle by the very high content of Co and Fe as compared to K and Ti and its much larger size of approximately 5 μm typical for these particles (see Figure 2). Note that Bi is not displayed in Figure 68, since a beam of Bi ions was used to analyse the sample surface which resulted in a homogeneous distribution of Bi across the whole area. Using the Bi ion beam was, however, necessary to achieve the necessary resolution. The radar chart in Figure 68b shows relative elemental intensities of Fe, Co, K and Ti for MFC, $CoFe_2O_4$ particle and matrix according to mass spectra shown in Figure 68c. To obtain these spectra, regions-of-interest representing the three aforementioned entities were selected. The intensities of mass spectra according to these regions, were normalized by the sizes of the selected regions. From Figure 68b it becomes obvious that the $CoFe_2O_4$ particle almost exclusively contains Fe and Co, whereas the matrix contains mostly K and Ti. In contrast, the MFC contains all elements in medium concentration. This is in agreement with our expectations, since it was expected that ferrimagnetism arises from higher local concentration of Fe and Co as compared to the matrix, but lower as compared to $CoFe_2O_4$.

It is important to note, that for $CoFe_2O_4$ the intensities of Fe and Co have approximately the correct ratio of 2:1 (measured 2.23:1) as expected from chemical composition. In SIMS, intensities for different elements usually cannot be directly related to elemental composition due to their different ionization probabilities causing different sensitivity factors for different elements. K as an alkali metal, has for example much higher intensities than other elements. Therefore, only relative intensities for a given element can be compared for the different areas. However, in case of Fe and Co which have very similar ionization energies (762.5 and 760.4 kJ/mol respectively [150]) and relative sensitivity factors in mass spectrometry [106], peak intensities can be related to each other. In case of the MFC, the measured ratio of Fe to Co signals is 2.5:1 which is close to the ratio as in $CoFe_2O_4$. Therefore, taking into account the lower K and Ti concentration as compared to the matrix, it is expected that the composition of the MFC is approximately $(BiFe_{0.7}Co_{0.3}O_3)_{0.6-0.8}$-$(Bi_{1/2}K_{1/2}TiO_3)_{0.4-0.2}$.

SIMS experiments furthermore exclude, that the MFC as imaged by MFM are due to deeper lying magnetic particles, since SIMS is very surface sensitive (1-2 nm penetration depth).

6.4.3 **Macroscopic magnetic characterisation**

After the two different magnetic phases had been characterized on a microscopic level, it was tried to distinguish them with macroscopic methods as well. To this end, magnetic properties as function of temperature were carefully analysed as illustrated in Figure 69.
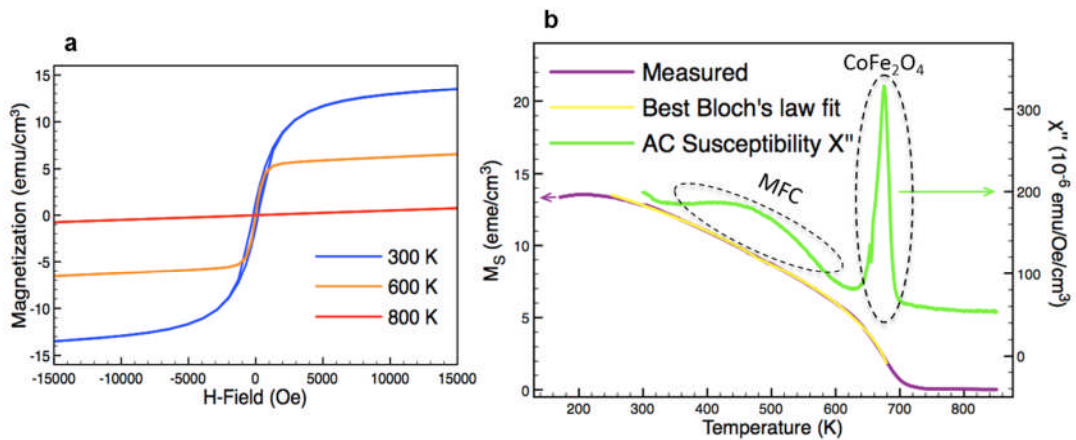
Figure 69 Magnetic characterisation of BFC-BKT ceramics. **a**, Magnetization vs. magnetic field (*M-H*) loops T = 300, 600 and 800 K. **b**, The spontaneous magnetization, M_S ≈ 2 M(25 kOe)-M(50 kOe) vs. *T* (—) is best-fitted by Equation 6-1 between 250 and 680 K (—). Imaginary part of AC susceptibility (χ'') vs.T (—, H_{AC} = 10 Oe, f = 23 Hz) reveals two peaks at 471.8 and 673.7 K which are correlated with the Curie temperatures of two different magnetic components, MFC and CoFe2O4.

The magnetization *vs.* magnetic field (*M-H*) loop at room temperature (Figure 69a) displays non-linear magnetic behaviour, with low coercivity and a saturation magnetization of approximately 12.3 emu/cm^3. The magnetization decreases at higher temperatures until the material becomes paramagnetic (800 K). For analysis of magnetic contributions, the spontaneous magnetization, M_S ≈ 2M(25 kOe)-M(50 kOe) *vs. T* (Figure 69b) was recorded. Since paramagnetic contributions to the magnetization are relatively large in studied BFC-BKT material, the M_S *vs. T* curve presented in Figure 69b, was obtained by measuring two magnetization vs. temperature (*M vs. T*) curves, one at 25 and another one at 50 kOe. Measuring at such

high fields ensures that the sample is in saturation at all temperatures which was verified by *M-H* measurements at low temperatures. By subtracting *M* measured at 50 kOe from two times *M* measured at 25 kOe, all paramagnetic contributions are subtracted and only M_S is obtained, since paramagnetic contributions are expected to be linearly proportional to magnetic field. M_S, decreases above approximately 200 K, follows the best-fitted Equation 6-1 between 250 and 680 K, and shows a Curie transition to a paramagnetic state at $T_C \approx 704\pm1$ K. The imaginary part of the AC-susceptibility (χ'') is sensitive to magnetic energy dissipation and thus phase transitions. It exhibits two distinctly different peaks (Figure 69b) and thus indicates two magnetic contributions as expected from previous experiments. The broad peak with centre at 471.8 K has a signature that differs significantly from the sharp peak at 673.7 K indicating two magnetic contributions as expected. Hence, the M_S *vs. T* curve was fitted by a function containing two Bloch's Law terms (see Figure 69b):

$$M(T) = M_1(0)\left(1 - \left(\frac{T}{T_{C,1}}\right)^{\frac{3}{2}}\right)^{\beta_1} + M_2(0)\left(1 - \left(\frac{T}{T_{C,2}}\right)^{\frac{3}{2}}\right)^{\beta_2}$$

Equation 6-1

with $M_i(0)$ = volume-magnetization of contribution *i* at 0 K, β_i = critical exponent of contribution *i*

The best-fit parameters are listed in Table 2:

Parameter	Multiferroic clusters	$CoFe_2O_4$
$M_S(0)$ (emu cm^{-3})	1.52±0.03	14.1±0.1
Critical exponent β	0.79±0.02	0.51±0.01
T_C (K)	478±2	688±1
Peak temperature of χ''(K)	472±1	674±1
Quality of fit	Reduced $\chi^2 = 0.00175$, Adj. $R^2 = 0.99981$	

Table 2 Fitting parameters of Bloch's law fit according to Equation 6-1. Curie temperatures of the fits are in relatively good agreement to the measured centres of peaks in imaginary AC susceptibility χ'' within the expected inaccuracy of the measurements.

The above function fits the M_S vs. T curve very well and Curie temperatures obtained from fitting are in good agreement with maxima of peaks in χ'' (471.8 K vs. 478.3 K and 673.7 K vs. 687.7 K) taking into account the expected inaccuracies of the measurements. These temperatures might be interpreted as average Curie temperatures of a given magnetic phase. The relatively small discrepancies in measured and fitted Curie temperatures can be readily explained by different temperature sweep rates used in DC and AC measurements (i.e. sample's temperature lagging the sensor) and/or the field dependence of T_C (M_S measured at 25 and 50 kOe while χ'' at 10 Oe).

We attribute the contribution with T_C around 680 K to the $CoFe_2O_4$ secondary phase which, as a classical magnetic material, is expected to exhibit a sharp peak in χ'' at the Curie transition. Although the Curie temperature of pure $CoFe_2O_4$, 793 K [151], is higher, this might be explained by doping with 'diluent' diamagnetic ions (dilution in terms of magnetic order) such as Ti^{4+}, as measured by SIMS (see Figure 68). The broad peak around 475 K on the other hand, is attributed to the MFC. A lower T_C for the MFC as compared to pure $BiFeO_3$ with its Néel temperature of 650 K due to doping with diamagnetic K^+ and Ti^{4+} ions is also expected in this case. Since the MFC presumably have a perovskite crystal structure which is diluted with diamagnetic ions especially at the edges (see Figure 68), they should at

least partly consist of a network of magnetic ions, following percolation statistics similar as in the well-studied $PbFe_{1/2}Nb_{1/2}O_3$ (PFN) [40]. Such clusters are expected to exhibit a broad distribution of Curie temperatures as evident from the broad peak in χ'' *vs. T* due to statistics. This rather unusual cluster nature of the MFC might also explain the relatively large critical exponent $\beta \approx 0.79$ for the MFC, leading to a quite linear M_S *vs. T* curve. The other magnetic component however, displays a classical transition in Landau theory with a critical exponent close to 0.5 which suggests that this component is due to $CoFe_2O_4$.

Although, the macroscopic M_S of the sample is dominated by the $CoFe_2O_4$ phase, the contribution of the MFC (approximately 10%) cannot be neglected, since the M_S *vs. T* curve is fitted much less accurately by just one Bloch's law term. However, it will be shown in the following paragraphs, that the MFC show strong local ME coupling, which is not influenced by the secondary phase. An in-situ PFM under magnetic field experiment, similar to the one presented in Section 6.6.2 was carried out close to a $CoFe_2O_4$ particle. Here, no ME coupling effect could be observed.

6.5 Local hysteresis measurements

Using magneto-optic Kerr effect (MOKE) under magnetic field measurements, carried out selectively on $CoFe_2O_4$ particles, it was found that they have a coercivity of $H_c = 1100 \pm 200$ Oe as shown in Figure 70.
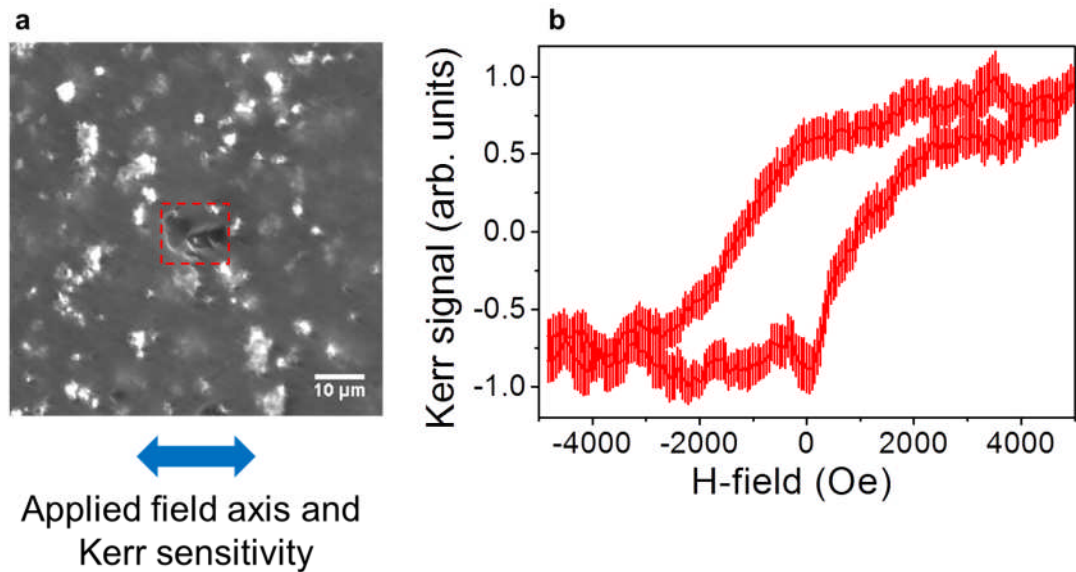
Figure 70 MOKE microscopy on magnetic secondary phase particles. **a**, Image showing a particle viewed through the Kerr microscope. **b**, MOKE signal *vs.* magnetic field according to area marked by red dashed rectangle in **a**. Data points are averages over nine adjacent points and the error bars are standard errors of the mean values. Applied field direction and Kerr (in-plane) sensitivity is indicated by blue arrow.

It is surprising that, on a macroscopic scale, BFC-BKT samples have much lower coercivities, $H_c \approx$ 100-200 Oe, since the influence of $CoFe_2O_4$ on macroscopic magnetic behaviour is expected to be very large. This difference might be explained by magnetic anisotropy, which can have an influence on the MOKE signal which is measured in-plane (as illustrated by blue arrow in Figure 70). However, this is not the case for macroscopic magnetization, which is measured over randomly oriented grains.

6.6 Local magnetoelectric coupling

6.6.1 Converse coupling via MFM in combination with tip-induced electric field poling

The MFC presented in Figure 63 was further investigated for local ME coupling with MFM and PFM as illustrated in Figure 71.
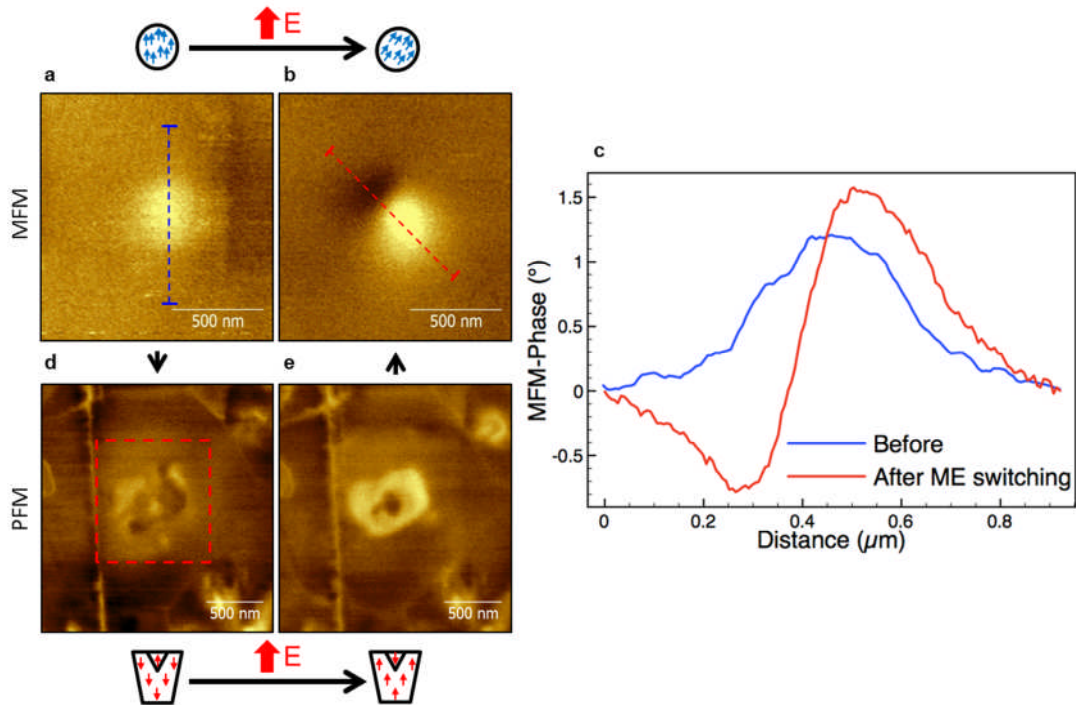
Figure 71 MFM and PFM measurements in combination with electric field poling. **a**, MFM image of the same magnetic cluster as in Figure 71c, after ex-situ switching with an out-of-plane magnetic field of +0.48 T. Symbol above images, represent single magnetic domains according to the magnetic MFM response. **d**,**e**, PFM images of congruent FE cluster recorded after ex-situ magnetic switching, before (**d**) and after (**e**) electric poling by scanning a rectangular area as indicated by red dashed rectangle while applying a DC bias to the tip. Configurations of the MFC's polarization are illustrated by symbols below PFM images. **b**, MFM image after electric field poling, showing ME switching from out-of-plane to partly in-plane orientation. **c**, MFM phase cross-sections of MFC before and after ME switching across the blue and red dashed lines in **a** and **b** respectively.

After the MFC's magnetization had been switched to an out-of-plane direction as visible in Figure 71c (see also Figure 62c), it was poled, by scanning a rectangular area around it, as indicated by the red dashed rectangle in Figure 71d, while applying a DC voltage of 20 V. For imaging, an AC voltage of 2 V was applied so as not to induce any poling due to the probing voltage. After electric poling, the polarization of the MFC was inverted (Figure 71e) and at the same time, the magnetization was switched from a complete out-of-plane (Figure 71a) to a partly in-plane (Figure 71b) orientation as indicated by symbols. This is also clearly visible when considering the MFM cross sections through the MFC (Figure 71c). It is worthwhile mentioning, that this experiment could be reproduced very accurately. The converse switching will be analysed in more detail in Section

6.6.3. However, not only converse, but also direct ME coupling was investigated locally.

6.6.2 **Direct coupling via PFM under in-situ magnetic field**

As mentioned previously, one of the goals of this project was to investigate also the direct local ME coupling using in-situ PFM under magnetic field which was also carried out on BFC-BKT ceramics. Results of these experiments are illustrated in Figure 72 which shows selected out-of-plane in-situ PFM images under magnetic field.
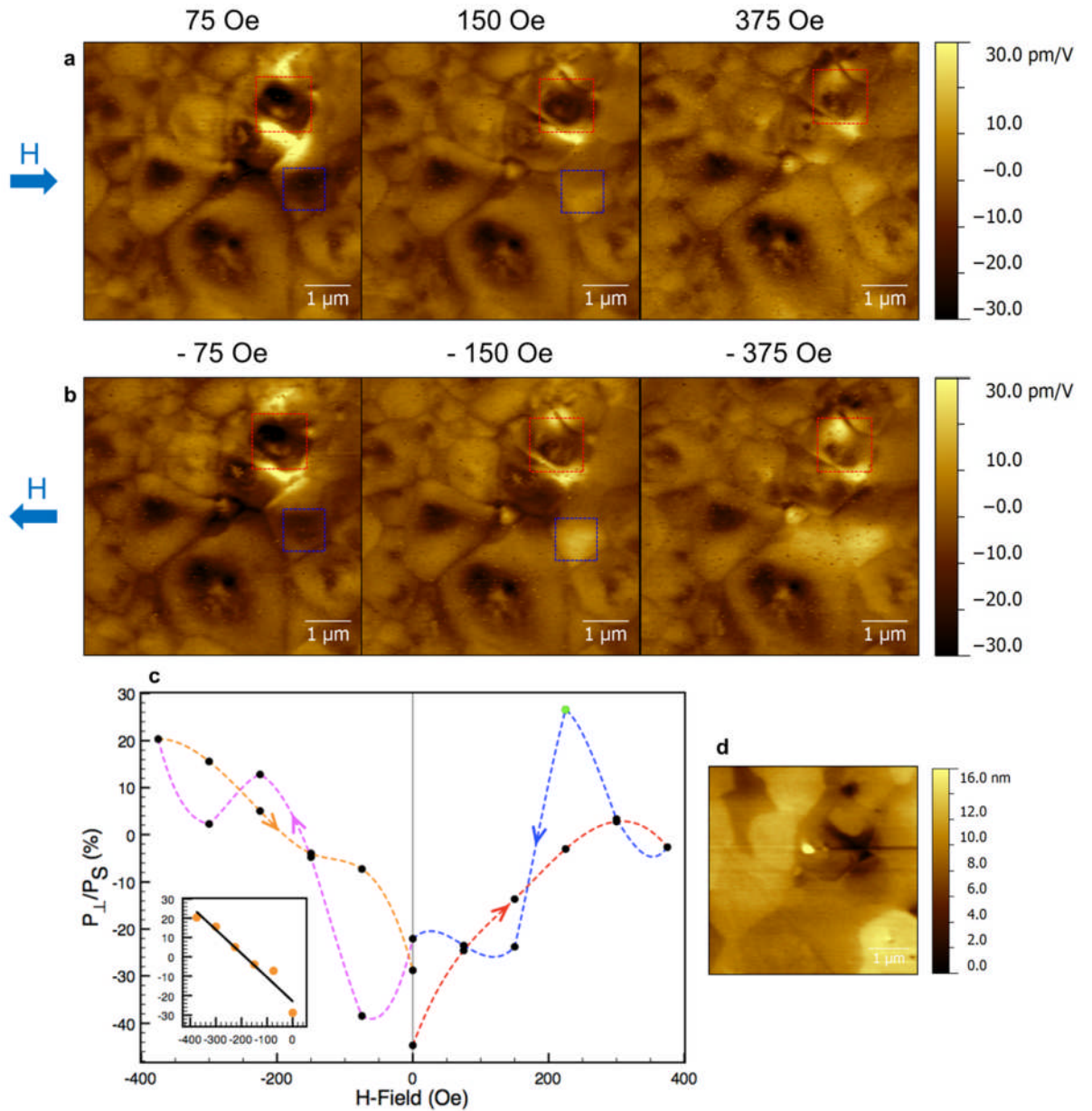
Figure 72 In-situ PFM under magnetic field experiments. **a,b** Selected out-of-plane PFM images from a magnetic-field loop series consisting of 21 images. Magnetic field strength is according to labels and direction is according to blue arrows. Change of piezoactivity is evident *e.g.* in regions marked by blue and red rectangles. **c**, Polarization *vs.* magnetic field data referring to the region marked by the red rectangle in PFM images. Dashed lines are spline-fits of data points (•) to indicate the direction of the magnetic field. A strong sporadic switching event is marked by (•). Inset shows linear fit to data points from the orange line. **d**, AFM topography corresponding to **b** row images.

In total, 21 PFM images constituting a complete magnetic field loop with 0, ±375 and 75 Oe as starting-point, magnetic field range and step-size respectively, were recorded. Images in row **a** clearly display a magnetic field-induced change of an MFC's polarization, in the top right corner of

images. The direction of magnetic field, relative to the sample surface is indicated by blue arrows beside PFM images. By taking the average PFM signal of a highly ME active region marked by red rectangles in row **b**, the change of out-of-plane polarization of this area as a function of magnetic field can be obtained which is shown in Figure 72c (for calculation of $P_\perp/P_S$ from PFM signals see below). This plot reveals a large change of polarization over a relatively small magnetic field range. The curve exhibits a V-like shape, where the polarization varies roughly linearly with magnetic field but, regardless of its direction. Thus the ME mechanism is not simply linear.

A stress-strain mediated ME coupling mechanism, might explain the shape of the curve by coupling via magnetostriction and piezoelectricity. Many magnetostrictive materials such as ferrite spinels or metal alloys exhibit such a V-shape magnetostriction curve. The resultant magnetostrictive strain in turn is coupled to polarization linearly via the piezoelectric effect and thus would explain the observed shape of the curve. Above the red dashed rectangle in Figure 72a and b there is a region which exhibits an inverted switching behaviour as the region inside the rectangle, where a bright region at low field becomes dark at ±375 Oe. Below the region of the red rectangle, the same can be observed although less pronounced. This behaviour can be understood when considering that the MFC inside the red rectangle applies a longitudinal magnetostrictive stress within this region, and a transversal stress with opposite sign onto the regions above and below.

Furthermore, strong sporadic switching events (see green dot in Figure 72c), as well as an ageing effect were observed. This behaviour was also reported by Evans *et al.*, who observed domain-switching by PFM with ex-situ magnetic fields in multiferroic $(PbZr_{0.53}Ti_{0.47}O_3)_{0.6}$–$(PbFe_{0.5}Ta_{0.5}O_3)_{0.4}$. The authors attributed this behaviour to sudden releases of elastic energy. This indicates that clamping of the MFC by the surrounding material might play a role and that switching events take place after a certain threshold-field is achieved.

6.6.3 **Quantification of local magnetoelectric coupling**

Since the ME response appears to be roughly linear within the experiment's uncertainty in a small range of magnetic fields and for the sake of quantifying the effect in a comparable way, the linear ME coupling-coefficient for a limited range of magnetic fields will be estimated, although the coupling is clearly non-linear over the whole range of magnetic fields tested in this experiment. As outlined in Section 6.6, the direct linear ME coupling-coefficient can be expressed as:

$$\alpha_{ij} = \frac{\partial P_i}{\partial H_j}$$

<div align="right">Equation 6-2</div>

with P_i being the ith component of the electrical polarization and H_j being the jth component of the external magnetic field, respectively (see Section 1.6.1). To estimate the change of polarization over a range of magnetic fields, PFM signals need to be quantified which was done using a standard calibration sample, periodically poled lithium niobate (PPLN) as described in Section 3.4.2. A calibration factor K_{PPLN} is obtained by dividing the d_{33} coefficient (approximately $d_{33,A}$ = 20 pm/V), by the average PFM signal difference between 180° domains of PPLN per Volt (PFM_{PPLN}) of the AC driving voltage.

$$K_{PPLN} = \frac{d_{33,A}}{PFM_{PPLN}}$$

<div align="right">Equation 6-3</div>

PFM_{PPLN} (0.97 V) was obtained from measurements presented in Section 3.4.2 (diamond coated tip). To ensure a more reliable calibration, the same AC frequency, voltage and AFM tip model was used for calibration measurements and for PFM under in-situ magnetic field. The macroscopic d_{33} coefficient of BFC-BKT $d_{33,B}$ = 16 pm/V (obtained from Berlincourt measurements) multiplied by the AC driving voltage V_{AC} and divided by K_{PPLN}, yields another calibration factor K_{BFC} for PFM signals that corresponds to a polarization change of 180° for BFC-BKT.

$$K_{BFC} = \frac{d_{33,B} \cdot V_{AC}}{K_{PPLN}}$$

<div align="right">Equation 6-4</div>

K_{BFC} can be used to estimate the ME coupling-coefficient as follows:

$$\alpha = \frac{2P_S \cdot m}{K_{BFC}}$$

<div align="right">Equation 6-5</div>

where P_s is 33.9 µC/cm^2 which is obtained from a macroscopic *P-E*-loop (see Figure 59a) measurement and m/K_{BFC} = 0.123 %/Oe is the slope of the linear fit to the orange data points in Figure 72c (inset) and corresponds to the change of polarization with magnetic field. Thus an effective coefficient $\alpha_{31}{}^{eff}$ = 1.0 x 10^{-5} s/m is estimated which is, to the best of our knowledge, the highest coupling coefficient reported for a single-phase multiferroic yet. It is roughly two orders of magnitude larger, than the local coupling coefficient estimated by Evans et al. [67] and five orders larger than that obtained on $(BiFeO_3)_{0.6}$–$(Na_{0.5}Bi_{0.5}TiO_3)_{0.4}$ [152]. Nevertheless, we want to stress that the calculated value is an estimate of the order of magnitude rather than an exact determination of the ME coefficient. It is, however, intuitive that the coefficient should be large, since relatively small magnetic fields (375 Oe at most) result in considerable switching of the MFC, which should be due to an extremely large ME coupling coefficient.

The strong ME coupling correlates well with the fact that MFC exhibit both ferroelectric and presumably ferrimagnetic order. Another reason for the exceptionally large ME coupling, might be the dielectrically flexible matrix, surrounding the MFC. The dynamic and flexible PNR might facilitate ME reorientation of the MFC's polarization by accommodating strain due to the reorientation process, which effectively reduces clamping of the MFC. In case of a large scale single domain multiferroic material, this might not be possible.

Subsequently, the converse ME coefficient from the experiment presented in Figure 71 will be compared to the direct one. As introduced in Section 1.6.1, the converse linear ME coupling-coefficient α_c can be expressed as following:

$$\alpha_{c,ij} = \mu_0 \frac{\partial M_i}{\partial E_j}$$

<div align="right">Equation 6-6</div>

with μ_0 = vacuum-permeability, M_i = volume-magnetization, and E_j = electric field components.

We can expect high numerical values with similar magnitude both for $\mu_0 M$ and P for the MFC from Figure 71 and Figure 72 respectively when converted to SI units, since both show large magnetization and polarization judging from the magnitude of MFM and PFM signals respectively. Unfortunately, the electric field used for poling as illustrated in Figure 71d and e is unknown due to the non-uniform field underneath the tip. However, we can expect a large ME coupling coefficient due to the large reorientation of approximately 46.8% of the MC upon application of electric field. The reorientation can be estimated from the MFM cross-section through the MFC (Figure 71c) by comparing the relative heights of signals corresponding to bright and dark areas. This reorientation is almost identical as compared to that of the polarization displayed in Figure 71c over a change of magnetic field of 375 Oe. Therefore a similar order of magnitude for the direct and converse ME coupling coefficients is expected.

6.6.4 Discussion of possible artifacts in PFM

In case of the direct ME switching, various possible artifacts for the observed magnetoelectric switching were considered:

One could imagine, that the switching of the MFC's polarization was not due to the magnetic field, but due to poling by the AC electric field used for PFM imaging. However, several PFM images of the same region were recorded prior to PFM under magnetic field loops. These images recorded prior to magnetic field application were all very similar and exhibited the same pattern. Thus, it is concluded that the dielectric structure of the MFC was stable before application of the magnetic field. The fact that the polarization of the MFC was reversible with magnetic field furthermore supports that the observed effect is actually due to ME interaction.

It can be excluded, that changes of polarization as shown in Figure 72c are due to sample drift. Areas of PFM images to obtain the respective data were chosen very carefully and a small sample drift was corrected for.

Contamination or wear of the tip can lead to change of PFM signals. However, these effects usually result in a change of absolute PFM signals and resolution of PFM images and topography, however they would not result in inversion of PFM contrast. Furthermore, for all PFM images related to the magnetic field loop in Figure 72c, the resolution of images and absolute PFM signals stayed very similar.

We do not expect surface charges to have had a significant influence on PFM signals since a sufficiently stiff cantilever in combination with relatively high contact pressure was used. For these conditions, any influence of surface charges on PFM signals should be suppressed [123].

6.6.5 Discussion of possible artifacts in MFM

One could imagine that the switching of the MC upon application of electric field (Figure 71e and f) is not actually due to the electric field, but due to back-switching over time. However, out-of-plane configurations (Figure 71d and e) were stable for at least 12 hours, whereas switching between the states shown in Figure 71e and f was recorded in less than 1 hour. Also, continuous recording of MFM images did not result in a change of any of the configurations shown in Figure 71 due to the magnetic moment of the MFM tip. We can thus conclude that MC configurations are sufficiently stable and that the observed magnetoelectric switching was due to the application of electric field.

6.7 Magnetic nanoregions

The material was furthermore investigated using ZFC-FC curves as outlined in Section 1.5.4 which is illustrated in Figure 73.
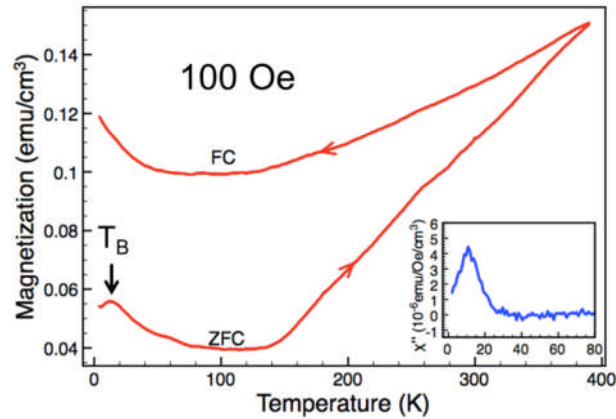
Figure 73 Zero-field cooling (ZFC) and field cooling (FC) magnetization vs. temperature curves measured at H = 100 Oe. A blocking transition is indicated by black arrow. Direction of measurement is indicated by red arrows. Inset shows imaginary part of AC susceptibility (χ'') vs. temperature measured at H_{AC} = 20 Oe, f = 20 Hz with a DC offset H = 10 Oe.

Both for the ZFC and the FC curve, an increasing magnetization above approximately 130 K and a large difference between the two curves can be observed. Both facts are attributed to a magnetic melting of $CoFe_2O_4$ particles and MFC which progressively align with the field above 130 K due to thermal activation. The fact that also the FC curve decreases upon cooling from room-temperature to 130 K, might be attributed to antiferromagnetically coupled Fe atoms. However, this tendency is less pronounced when measuring at higher fields, where the ferrimagnetic components become more dominating. A small maximum in the ZFC curve at approximately 13 K is attributed to blocking of (superpara)magnetic nanoregions (MNR) which are sufficiently small that thermal energy above the blocking-temperature T_B can flip their magnetic moment (see Section 1.5.4). These MNR are presumably due to the presence of PNR which are connected to the relaxor nature of the system and give a spatial constraint to MNR as outlined in Section 1.5.4.1. A maximum at the same temperature as the T_B in the imaginary part of the AC susceptibility (χ'', inset of Figure 73b) is further indication of this blocking process.

To support the superparamagnetic state and presence of MNR, Mössbauer spectra were recorded as presented in Figure 74.
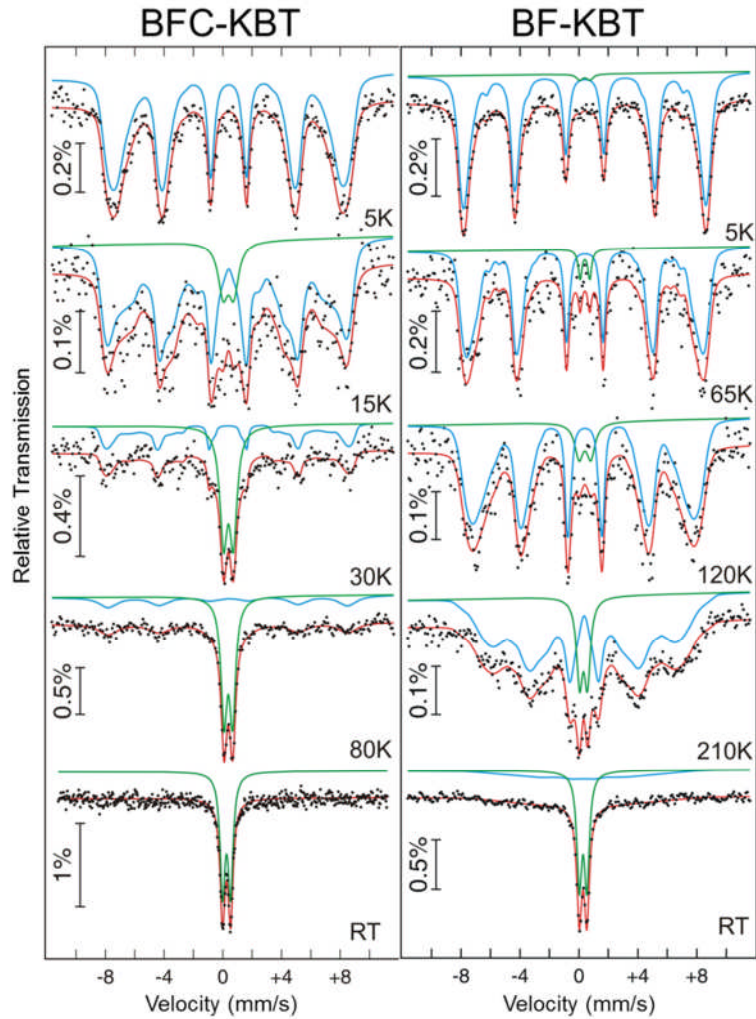
Figure 74 Comparison of ^{57}Fe Mössbauer transmission spectra at various temperatures for BFC-BKT and $(BiFeO_3)_{0.4}$-$(Bi_{1/2}K_{1/2}TiO_3)_{0.6}$ (BF-BKT) according to labels with: fit to data (—), sextet contribution (—) and doublet contribution (—).

The Mössbauer spectra for BFC-BKT show a temperature-evolution which is characteristic for superparamagnetism. At 5 K, the MNR are blocked which results in a sextet (six line signal). At this temperature, all Fe atoms are antiferromagnetically ordered (or in ferrimagnetic order with Co atoms). As temperature increases, the sextet-area gradually decreases and is replaced by a gradually growing doublet over a relatively wide range of temperatures. The doublet corresponds to thermal relaxation or 'unblocked' superparagmagnetic MNR whose magnetization fluctuates faster than the Larmor period of 5 x 10^{-9} s for ^{57}Fe nuclei. These effectively appear to be paramagnetic in Mössbauer spectroscopy and thus cause a doublet. In

comparison, for a classical Curie or Néel transition, there would be no coexisting sextet and doublet signals at one temperature or only over very a narrow temperature range. The fact that a doublet and not a singlet occurs is due to quadrupole splitting which indicates that the Fe atoms are not in a centrosymetric environment, which is expected due to the ferroelectric nature of the material which requires a non-centrosymmetruc structure. Mössbauer spectra recorded on $(BiFeO_3)_{0.4}$-$(Bi_{1/2}K_{1/2}TiO_3)_{0.6}$ (BF-BKT) also exhibit superparamagnetic behaviour. However, here the transition occurs at much higher temperatures, which also results in a higher blocking temperature T_B. The large difference between T_B for BFC-BKT and BF-BKT emphasizes the influence that Co has on the magnetic properties of the system. An explanation for the difference will be given below.

Because the blocking of MNR is a dynamic process, the blocking transition in Mössbauer spectroscopy occurs at higher temperatures than in magnetometry, due to much shorter time constants of the former method compared to the latter. A comparison between magnetometry and Mössbauer spectroscopy blocking temperature is shown in Figure 75.
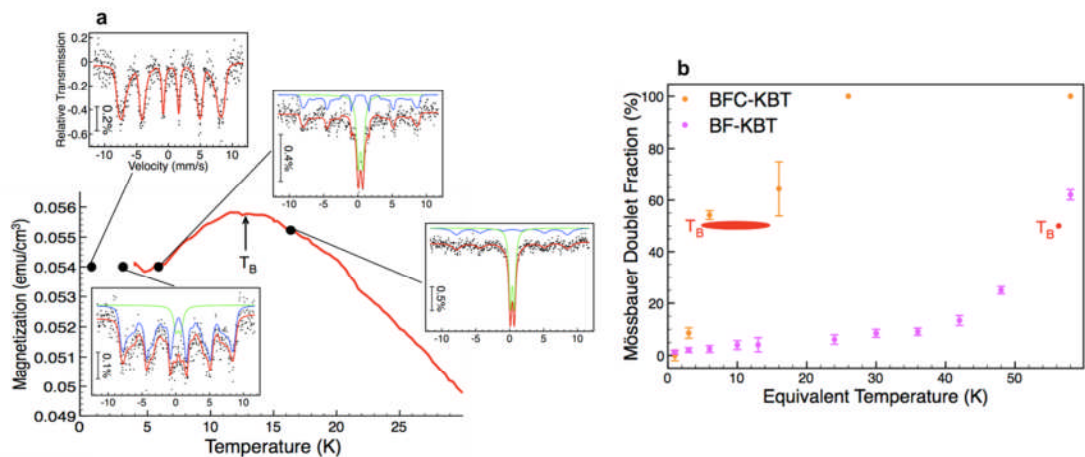
Figure 75 **a**, Magnification of maximum in ZFC curve from Figure 73 with ^{57}Fe Mössbauer spectra measured at equivalent temperatures as indicated by points on ZFC curve. Curves in Mössbauer spectra are: fit to data (—), sextet contribution (—), doublet contribution (—). **b**, Temperature evolution of the doublet fraction in Mössbauer spectra for BFC-BKT (•) and BF-BKT (•). Temperature corresponds to a converted temperature using a factor of 1/5 and not the actual temperature of measurements.

In order to better compare the blocking temperatures obtained in magnetometry and Mössbauer spectroscopy, the measurement

temperatures from the latter are converted to temperatures as for a static technique like DC magnetometry. A rough conversion factor between temperatures in Mössbauer spectroscopy and magnetometry is 5:1. We will call these converted temperatures as equivalent temperatures (ET, see Figure 75b). In case of the Mössbauer blocking-temperature $T_{B,M\ddot{o}}$ which is defined as the temperature where the areas of sextet and doublet signals are equal, only a temperature range can be estimated (see T_B in Figure 75b) due to few measurements points in the temperature range close to $T_{B,M\ddot{o}}$. This range is 4-15 K which is in agreement with $T_B = 13$ K from magnetometry within the uncertainty of the experiment and temperature conversion. Thus the majority of Fe-atoms are within these MNR, since far above T_B at ET 26 K (see Figure 75b), the sextet area is below the noise level which means that approximately more than 90% of Fe-atoms are contained within MNR. Furthermore, we expect that MNR display only weak-ferromagnetic behaviour or uncompensated spins at interfaces [153], since their contribution to magnetism, which corresponds to the small maximum in the ZFC curve is small compared to the major magnetic contribution characterized by the defreezing process, although they contain the majority of the Fe-atoms. Thus they should contain no or very little Co, since this should lead to ferrimagnetism and thus larger magnetization. This is in line with SIMS measurements. The $CoFe_2O_4$ phase does not contribute to Mössbauer spectra in this case, since only phases with a content of approximately 10% are above the noise level in this case.

The significantly different blocking temperatures observed for BFC-BKT and BF-BKT of approximately 43 K as illustrated in Figure 75, might be attributed to a change of size of MNR by several nm. We have already seen that the addition of Co causes formation of large BFC rich clusters, which might lead to an increased concentration of the BKT component in the rest of the material which contains most of the Fe-atoms and thus dominates Mössbauer spectra. However, a higher concentration of the charge disordering BKT-component in the BFC-BKT matrix as compared to pure BF-BKT, might lead to a reduced size of PNR, which would presumably also cause a reduction of MNR size and thus a decreased T_B for the Co containing material.

6.8 **Magnetic neutron diffraction**

As introduced in Section 2.5.6 neutron diffraction is probably the most powerful tool to study the magnetic structure of a material. Therefore, neutron diffraction was carried out as function of temperature on ceramic BFC-BKT samples.
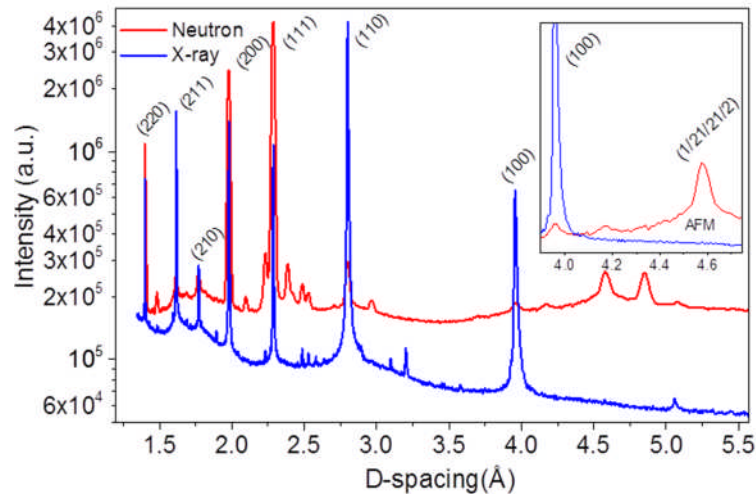
Figure 76 Neutron diffractogram (—) of BFC-BKT at temperatures below 30 K (λ = 2.52 Å, logarithmic intensity scale). Inset (linear intensity scale) shows magnification showing antiferromagnetic (½½½) peak with twice the d-spacing as compared to (111) peak. *X*-ray diffractogram (—) exhibits no peak at the same position, indicating that the peak is due to antiferromagnetic order.

Figure 76 shows neutron and *X*-ray diffractograms (see labels) of BFC-BKT where intensity is plotted *vs.* D-spacing with pseudo-cubic indexing as presented in Figure 58. Similar to related $(BiFeO_3)_x$-$(Bi_{1/2}K_{1/2}TiO_3)_{1-x}$ (x = 0.6, 0.7, 0.8) compounds [91], Neutron diffraction reveals an antiferromagnetic (AFM) (½½½) peak at 4.58 Å which is twice the d-spacing of the pseudocubic (111) nuclear peak at approximately 2.29 Å. This corresponds to 31.9° in 2θ for a wavelength of 2.52 Å of the used neutrons. The absence of this peak in the *X*-ray diffractogram confirms that it is an AFM peak (see inset).

Temperature dependent measurements did not indicate a structural phase transition in the material between 1.5 and 550 K. However, as expected the AFM peak changes as function of temperature as illustrated in Figure 77.
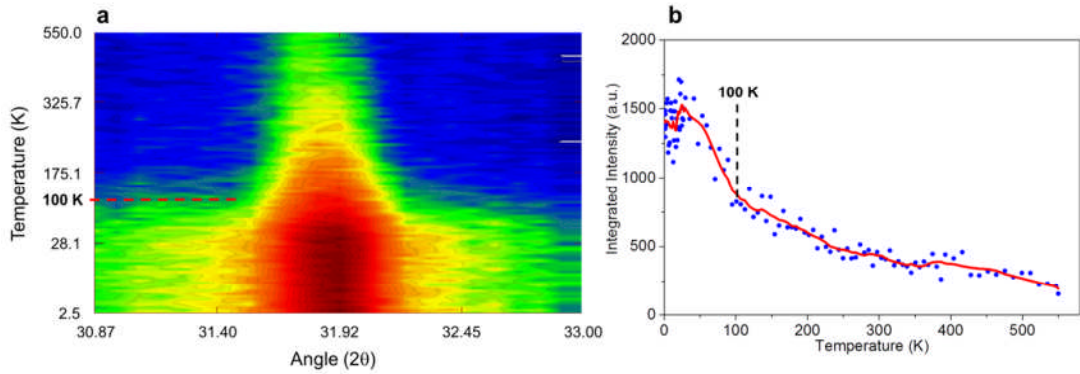
Figure 77 Temperature dependence of antiferromagnetic (½½½) Peak. **a**, Colour map showing temperature evolution *vs.* bragg angle with intensity represented by colours from red to blue. The peak is broad up to temperatures of approximately 100 K which is attributed to blocked magnetic nanoregions. Note that the temperature scale is not linear to emphasize temperature evolution at low temperatures. **b**, Integrated intensity of AFM peak *vs.* temperature showing a rapid decrease of intensity up to approximately 100 K which is followed by a slower decrease at higher temperatures.

Figure 77a shows a false colour map for the temperature dependence of the AFM peak where the temperature is plotted *vs.* the bragg angle and intensity is displayed as colours with decreasing intensity from red>yellow>green>blue. Note that the temperature scale is not linear to emphasize temperature evolution at low temperatures. While the AFM peak is broad up to approximately 100 K, it gets significantly narrower above this temperature and continues to decrease in intensity up to the highest temperature, 550 K. However, the AFM peak is still present at this temperature, although with low intensity. This is in agreement with the AC susceptibilty as illustrated in Figure 69b, which suggests that the MFC lose their magnetic order above the broad peak ranging approximately from 320 to 600 K. The temperature evolution of the AFM peak is also reflected in Figure 78b which shows the integrated intensity of the fitted AFM peak *vs.* temperature. Here, the intensity decreases rapidly until approximately 100 K, whereas above this temperature, it decreases more slowly. The temperature dependence of the AFM peak is more closely analysed in Figure 78.
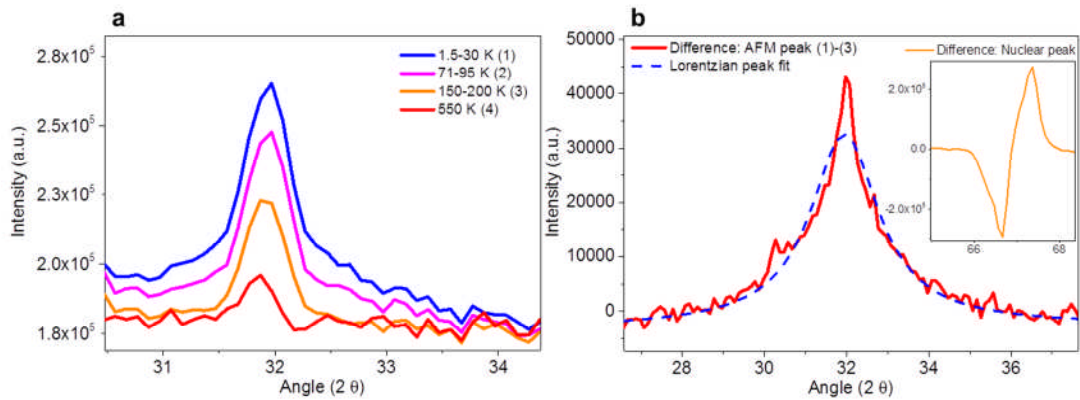
Figure 78 Temperature dependence and fitting of antiferromagnetic (½½½) peak. **a**, Antiferromagnetic peak at temperatures from 1.5-30 K (—), 71-95 K (—),150-200 K (—) and at 550 K (—). **b**, The difference of diffractograms from 1.5-30 K and 150-200 K reveals a Lorentzian contribution to AFM peak at low temperatures which is attributed to blocked MNR. Inset shows the same difference for a nuclear bragg peak (111) which has a 'zig-zag' shape due to thermal expansion of the crystal lattice.

Figure 78a shows the AFM peak averaged over certain temperature ranges as indicated by the legend. As shown above, the peak is broad between 1.5-30 K (Peak 1) with pronounced 'shoulders' to the sides of the central peak. The broad peak shape is attributed to a superposition of a Gaussian and a Lorentzian peak. The intensity of the shoulders starts to decrease above 30 K until approximately 100 K which becomes obvious when considering the peak from 71-95 K (—, Peak 2). The peak in the temperature range between 150-200 K (—, Peak 3) does not exhibit shoulders and is best fitted by a Gaussian. Its intensity stays relatively constant over this temperature range. At higher temperatures, the intensity of the Gaussian peak decreases but it is still present at 550 K (—, Peak 4) which was the maximum temperature that was reached during the experiment. It is assumed that Peak 1 has a Lorentzian and Gaussian contribution whereas Peak 3 represents purely the Gaussian contribution. Thus the difference between Peak 1 and 3 which is shown in Figure 78b should yield approximately only the Lorentzian contribution. In fact, the difference peak clearly has a broad Lorentzian shape as is typical e.g. for nanoparticles [38]. Accordingly, the peak can best be fitted by a Lorentzian (dashed line in Figure 78b). Furthermore, the form of the difference peak as illustrated in Figure 78b is further confirmation that it is in fact an AFM peak which is due to the fact that

AFM peaks decrease with temperature. In contrast, the inset shows the same difference diffractogram for a nuclear bragg peak (111) which has a 'zig-zag' shape due to the thermal expansion of the materials lattice parameters.

As mentioned above, the Lorentzian shape is indicative of a small crystallite or feature size related to the peak. Peaks corresponding to crystallite sizes much larger than 100 nm, would in theory result in a very sharp and narrow diffraction peak which usually cannot be resolved by the instrument. Instead those peaks have a Gaussian shape and are considerably broader than expected by theory. Other factors than crystallite size such as inhomogeneous strain, chemical heterogeneities or crystal lattice imperfections [154] can also cause broad diffraction peaks. However, because the broad AFM peak is only present at low temperatures, it is attributed to blocked MNR which were also found by ZFC-FC curves and Mössbauer spectroscopy in the same temperature range, when taking the time constants related to the different methods into account (see Section 6.4). As for Mössbauer spectroscopy, the time constant for neutron diffraction, which is related to the spin-spin interaction of neutron and electron, is considerably smaller than for magnetometry. At low temperatures, the MNR are blocked and cause coherent scattering of neutrons, resulting in the broad Lorentzian AFM peak. As temperature increases, MNR start to thermally relax. When the relaxation time of the MNR is shorter than the time constant of neutron diffraction, the MNR cause non-coherent scattering of neutrons, which in turn decreases the associated diffraction peak. The blocking temperature for neutron scattering which is the temperature where the peak related to blocked MNR is approximately at half of its initial intensity, is estimated to be $T_{B,N} \approx 70$ K from Figure 77b. This is based on the assumption that only the Lorentzian contribution associated to blocked MNR decreases at temperatures below 100 K and that furthermore, MNR are completely blocked at temperatures below 30 K and completely thermally relaxing at 100 K. As expected, the blocking temperature for neutron diffraction is much higher than for magnetometry ($T_B \approx 13$ K) and slightly higher than for Mössbauer spectroscopy ($T'_{B,M\ddot{o}} \approx 50$ K, non converted temperature), due to the shorter time-scale 10^{-9}-10^{-12} s [155] for

neutron diffraction as compared to the Larmor period of 5×10^{-9} s for ^{57}Fe relevant for Mössbauer spectroscopy.

The Gaussian AFM peak above 100 K is attributed to the larger MFC with sizes above approximately 500 nm, which is too large to cause peak broadening. As shown in Section 2.5.6, ferrimagnetism also results in magnetic half indexed bragg peaks. The ferromagnetic moment due to ferrimagnetic order of Fe and Co atoms, which results in a magnetic contribution on top of the nuclear (111) peak, could not be observed as in temperature dependent measurements, presumably due to the small amount of ferrimagnetic regions. These results are in agreement with previous results confirming the presence of both small dynamic MNR and larger static MFC. As expected from AC magnetometry, there exist MFC which are still magnetically ordered above 550 K.

6.8.1 Size determination of magnetic nanoregions

The mean thickness τ of the MNR can be calculated using the Scherrer equation [156]:

$$\tau = \frac{K\lambda}{\beta cos\theta}$$

Equation 6-7

With:

$$\beta = \sqrt{FWHM_M{}^2 - FWHM_S{}^2}$$

Equation 6-8

K = shape factor ≈ 0.9, λ = 2.52 Å, $FWHM_M$ and $FWHM_S$ = full width at half maximum of the magnetic peak (2.03°) and of a standard (0.19°, see Figure 35) respectively. The full width at half maximum is taken from the fitted Lorentzian presented in Figure 78b. With these values, the average size of MNR is approximately 13.6 nm which is a realistic value for a magnetic region exhibiting superparamagnetic behaviour. However, the MNR do not seem to behave like classical magnetic nanoparticles, which usually have

much higher blocking temperatures (80-200 K) for particle sizes smaller than 13.6 nm [35], [37], [38]. It is not clear yet, why this is the case.

6.9 **Conclusions**

Ceramics of the composition $(BiFe_{0.9}Co_{0.1}O_3)_{0.4}$-$(Bi_{1/2}K_{1/2}TiO_3)_{0.6}$ have been intensively studied for their multiferroic and ME properties. It was found that the material is a non-ergodic relaxor ferroelectric, exhibiting both small dynamic polar nanoregions (PNR) and larger static ferroelectric clusters (SPNR) as shown by *P-E*-measurements, permittivity *vs.* temperature and PFM investigations. The magnetic structure mirrors the dielectric one to a certain extent with superparamagnetic magnetic nanoregions (MNR) and large static but rare ferrimagnetic regions, as found by MFM. It is assumed that ferrimagnetic order is established in those regions due to higher concentration of Fe and Co as confirmed by SIMS. Due to the specific non-ergodic relaxor properties of the material, these regions always exhibit FE order at the same time, due to the lower concentration of the charge disorder inducing BKT component. Thus, the term multiferroic clusters (MFC) has been coined for these regions. The presence of MNR was confirmed on the other hand by ZFC-FC curves, Mössbauer spectroscopy and neutron diffraction. Blocking temperatures from the three techniques are in good agreement while their size is estimated to be 13.6 nm from the broad shape of the antiferromagnetic peak occurring at low temperatures in neutron diffraction. The MNR contain the majority of Fe atoms and exhibit antiferromagnetic order only with weak ferromagnetic behaviour unlike the Co containing MFC, as evidenced by Mössbauer spectroscopy and magnetometry. MNR presumably exist due to PNR, which give a spatial constraint to the magnetic correlation length and thus give rise to the MNR as introduced in Section 1.5.4.1. The above facts are emphasized in Figure 79 which schematically illustrates the material's partial dielectric and magnetic structures, as well as the combined multiferroic one.
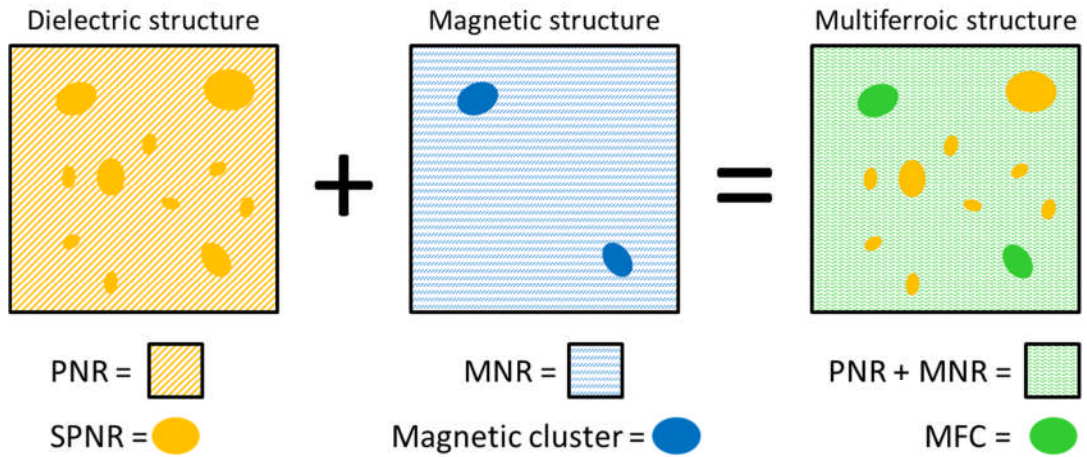
Figure 79 Schematic illustration of dielectric, magnetic and combined multiferroic microstructure of BFC-BKT. The dielectric structure is characterized by larger static polar nanoregions (SPNR), which are relatively numerous within a matrix containing dynamic polar nanoregions (PNR). The magnetic structure is similar to the dielectric one, since large static 'magnetic clusters' and dynamic magnetic nanoregions (MNR) are present. However, the rare magnetic clusters only exist in regions of higher BFC concentration where congruent SPNR occur simultaneously since a higher BFC concentration also enables long range FE order. Therefore, all magnetic clusters are actually multiferroic clusters (MFC). A combination of the two substructures yields the multiferroic structure which comprises many SPNR and only few MFC as well as congruent PNR and MNR. The latter supposedly form due to the spatial constraint imposed on them by the PNR.

It becomes clear that every ferrimagnetic region is an MFC at the same time, which is not the case for every SPNR. In essence, formation of MFC is governed by the interplay of the BFC component being responsible for ferrimagnetism and long range FE order, and the relaxor-state inducing BKT component which presumably also improves the overall dielectric properties of the solid solution.

The MFC exhibit an exceptionally large direct ME coupling, $\alpha \approx 1.0 \times 10^{-5}$ s/m (corresponds to a Voltage coefficient dE/dH ≈ 1.3 kV/(cm Oe)) effect which was found locally, using in-situ PFM under magnetic field. This is the largest ME coupling coefficient found for a single-phase multiferroic thus far, to the best of the author's knowledge (see Section 1.6.6 for comparison). Moreover, converse ME coupling was also observed presumably with similar magnitude. The *P vs. H* curve as observed in in-situ PFM under magnetic field measurements shows a linear field dependence, which is however, independent of field's direction and results approximately in a V-shape of the

curve. The shape might be explained by a linear intrinsic mechanism together with a low magnetic coercivity of the MFC. A stress-strain mediated mechanism via coupling of piezoelectricity and magnetostriction is also possible. Furthermore, PNR might play an essential role in the strong ME coupling since they represent an electrically and mechanically flexible environment, able to accommodate strain from rotation of the MFC's polarization. Such an effect would effectively reduce clamping of the MFC and thus lead to an increased ME coupling coefficient. Another possible explanation for the extremely large observed ME coupling, might be the presence of the PNR and MNR. It had been previously proposed, that the congruence of PNR and MNR might lead to an ideal stress-strain mediated 'interface' coupling resulting in large ME coupling [39], [96]. Furthermore, for 5 nm large magnetic nanoparticles, giant magnetostriction of 4% dimensional change has been reported [157]. A similar effect might apply to MNR in this system which could also explain the observed large ME coupling.

Although XRD measurements did not indicate the presence of a secondary phase, magnetic $CoFe_2O_4$ particles were found in BFC-BKT samples using SEM-EDX and MFM. Using a combination of temperature dependent DC and AC magnetometry measurements, contributions of MFC and $CoFe_2O_4$ to the overall magnetization could be distinguished. It was found that $CoFe_2O_4$ has a low content of approximately below 1%, but account for approximately 90% of the material's magnetization as confirmed by fitting of the spontaneous magnetization *vs.* temperature curve using a Bloch's law function. Nonetheless, $CoFe_2O_4$ is not critical in terms of local ME coupling and MFC. Using SIMS, it could be shown that MFC are chemically different from $CoFe_2O_4$ particles as evident by the concentration of Co, Fe, K and Ti. It can be further excluded that $CoFe_2O_4$ particles were mistaken for MFC, since the former are certainly not FE as evidenced by PFM, and display very different mechanical properties and sizes than MFC. Furthermore, no ME coupling was observed in the vicinity of $CoFe_2O_4$ using PFM under magnetic field. Thus it is concluded that $CoFe_2O_4$ particles do not interfere with the strong local coupling effects, although they are problematic for magnetic characterisation of BFC-BKT and should be eliminated in future work.

The discovery of the MFC exhibiting exceptionally large ME coupling is important, especially since it could be shown that the relaxor properties enable their formation which opens a new perspective for this class of ferroelectrics. Relaxor ferroelectrics had so far barely been considered for single-phase multiferroics. Furthermore, for the first time ferroelectricity and ferrimagnetism could be directly observed to occur in one material to the best of the author's knowledge.

If these MFC could be engineered to form an ordered array in a thin-film, they might be used as carriers of information in a memory device. One could imagine that epitaxial thin-films or single crystals might be engineered to contain an array of self-assembled MFC. Compositions closer to the one estimated for the MFC, $(BiFe_{0.7}Co_{0.3}O_3)_{0.6-0.8}$-$(Bi_{1/2}K_{1/2}TiO_3)_{0.4-0.2}$, might be ideal starting points for such experiments. Another possibility might be doping of selected regions in an epitaxial BF-BKT thin-film via ion-implantation of Co, or using molecular beam epitaxy in junction with shadow masks, to create islands of Co on top of a BF-BKT thin-film, followed by an annealing step to create the MFC. Since the ME coupling is restricted to well-separated magnetic regions, applications of electrically addressable magnetic MFC might be envisaged for future ME random access memory devices (MERAM) [4], thus making use of the converse ME effect. Such a memory is schematically illustrated with two possible designs in Figure 80.
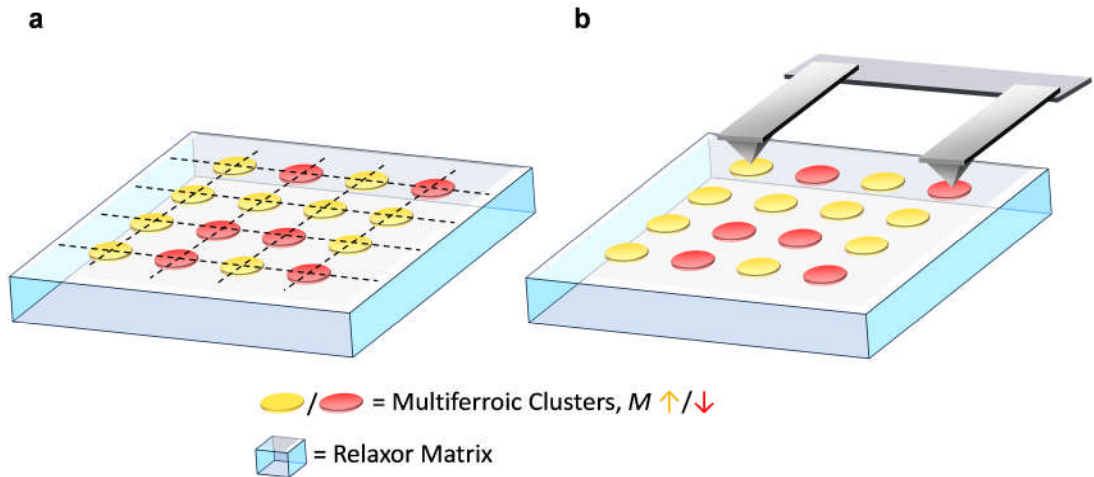
Figure 80 Schematic illustration of a possible ME memory device. An epitaxial BFC-BKT thin-film might be engineered to contain an array of multiferroic clusters within a relaxor ferroelectric matrix. Information is stored in an electrically controlled magnetic bit, adressable e.g. via a cross-bar architecture (**a**) or cantilever-type probes in a microelectromechanical systems (**MEMS**) device (**b**).

It is one of the main goals of research on ME and multiferroic materials, since it would considerably reduce energy consumption of usual magnetic memory, by enabling switching of magnetic bits without using electrical current [158].

7 Conclusions and future work

In this chapter, the most important findings of this thesis project are briefly summarized, before outlining planned future work. More detailed conclusions can be found at the end of each chapter.

7.1 Overall conclusions

Certainly, the most important findings of the project were obtained on the material $(BiFe_{0.9}Co_{0.1}O_3)_{0.4}$-$(Bi_{1/2}K_{1/2}TiO_3)_{0.6}$ (BFC-BKT). Here, main goals of the project could be achieved in studying ME coupling on a local scale in a single phase multiferroic. What's more, a new type of multiferroic region called *multiferroic clusters* (MFC) exhibiting exceptionally large ME coupling was discovered and their formation was understood in terms of the non-ergodic relaxor nature of BFC-BKT, enabling the formation of long range FE order in intrinsic ferrimagnetic BFC rich regions. Figure 81 summarizes key results characterizing multiferroic properties of BFC-BKT and the MFC.
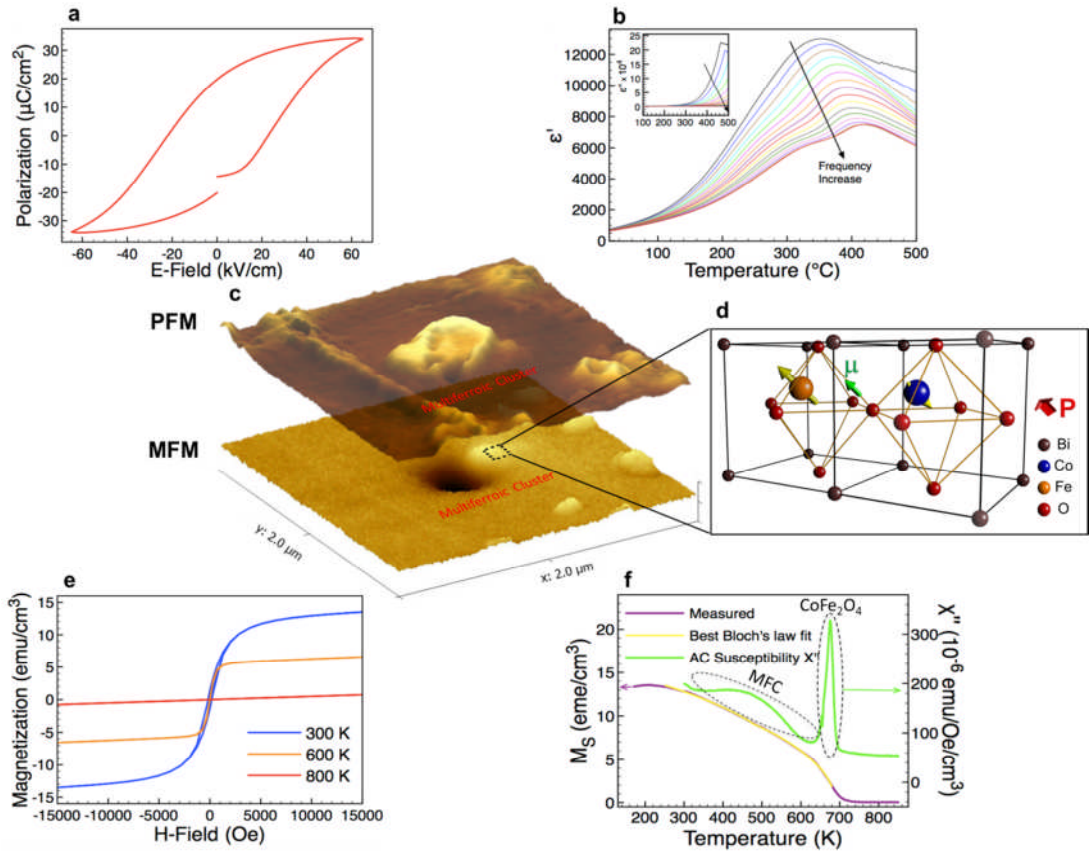
Figure 81 Main electrical and magnetic measurements characterizing BFC-BKT and the MFC. **a**, Polarization *vs.* electric field (*P-E*) loop at 1 Hz and room-temperature. **b**, Permittivity *vs.* temperature curves at logarithmically equidistant frequencies ranging from 1 kHz to 1 MHz. Measurements indicate relaxor FE properties. **c**, 3D representation of MFM image (bottom) overlaid with a PFM image of the exact same sample area showing the MFC. **d**, Idealized crystal structure of the MFC, schematically illustrating ferrimagnetic order of Fe^{3+} and Co^{3+}- Ions with net magnetization μ and polarization *P*. **e**, Magnetization vs. magnetic field (*M-H*) loops at *T* = 300, 600 and 800 K. **b**, The spontaneous magnetization, $M_S \approx 2\ M(25\ kOe)-M(50\ kOe)$ vs. *T* (—) is best-fitted by Equation 6-1 between 250 and 680 K (—). Imaginary part of AC susceptibility (χ'') vs. *T* (—, H_{AC} = 10 Oe, f = 23 Hz) reveals two peaks at 471.8 and 673.7 K which are correlated with the Curie temperatures of two different magnetic phases, MFC and $CoFe_2O_4$.

Great potential in applications is expected for these newly discovered MFC, since they exhibit exceptionally high ME coupling coefficients both for the direct and the converse effect. A potential ME memory device, which is one of the prime goals for research on multiferroics is outlined in Figure 80 and utilizes the MFC as electrically addressable magnetic bits. Possible routes to obtain such an ordered MERAM thin-film device, such as selective ion implantation of Co into an epitaxial BF-BKT or similar $BiFeO_3$ based relaxor-type thin-film, are discussed.

Another important consequence of the findings in Chapter 6 is the role of the relaxor ferroelectric state. It does not only enable formation of MFC, but presumably also plays an important role in the strong ME coupling, by supplying an electrically and mechanically flexible environment for the MFC, which effectively reduces their clamping and thus enhances ME coupling. This opens a complete new perspective for multiferroic relaxor ferroelectrics, which had so far barely been considered in research on single phase multiferroics. Furthermore, the existence of magnetic nanoregions (MNR) was confirmed by temperature dependent magnetometry, Mössbauer spectroscopy and neutron diffraction. They might also be important for the strong ME coupling and are presumably due to the presence of PNR.

The system PZT-PFW on the other hand, did not show local ME coupling effects or magnetic regions visible with MFM, congruent with our findings that ferrimagnetic MFC are necessary for the ME coupling, which are enabled by the presence of Co in the BFC-BKT system. However, similar trends are noticeable in both systems. That is, the existence of two characteristic magnetic species. While in PZT-PFW there exist networks of Fe atoms in the crystal lattice, apparently showing a broad Néel temperature distribution, in BFC-BKT these regions presumably are smaller (MNR) and thus show blocking behaviour. This can be explained by the existence of polar nanoregions (PNR) in the relaxor ferroelectric BFC-BKT, in contrast to PZT-PFW exhibiting macroscopic peak splitting in XRD, indicating more pronounced classical ferroelectric properties.

On the other hand, in both systems, regions with increased concentration of the magnetic three valent ions (Me^{3+}) exist, exhibiting significantly increased magnetic transition temperatures than expected from the average Me^{3+} content. These regions are, however, relatively rare and contain only small amounts of all Me^{3+}-ions in a sample. There seems to be a driving force, causing the formation of those Me^{3+}-ions rich regions, presumably during sintering via solid state diffusion. This mechanism might be utilized, by adjusting sintering parameters e.g. to increase the number of magnetic regions and adjust their size, in order to engineer a material suitable for applications.

The detection of magnetic impurity phases such as ferrimagnetic spinels Fe_3O_4 or $CoFe_2O_4$ is not trivial. In both systems, very small amounts of one of those phases were present, but not detectable in XRD. However, they influence the macroscopic magnetic behaviour significantly, since both perovskite materials possess weak intrinsic magnetization with the exception of the MFC. Both examples stress that simple *M-H*-loop measurements at room temperature in combination with absence of clear secondary phase peaks in XRD, are clearly not sufficient to justify weak ferromagnetic behaviour in any related single phase multiferroic. For detection of secondary phase particles, SEM-EDX elemental mapping is recommended. However, an appropriate sample surface polishing is strictly necessary. In case of BFC-BKT, AC susceptometry and DC magnetometry were employed over a wide temperature range, to distinguish between inherent and secondary phase magnetic contributions, which could be also applied to many other single phase multiferroics.

Another important aspect of the project, was piezoresponse force microscopy (PFM) to investigate local ME coupling. Factors such as signal stability, background signal and imaging artifacts were statistically investigated. Most important conclusions from these studies are that using tips coated with conductive diamond, offers several advantages and that the influence of correct sample polishing is very important in PFM. In addition, a method has been developed, to mark many micro areas on several samples for microscopy purposes at one time. It could be particularly useful in batch processing or for preselecting specific sample areas for further processing e.g. via focused ion beam (FIB).

7.2 **Future Work**

A proposal for a postdoc project based on the results of this project has been submitted to the DFG (German research association) end of February 2015. If successful, work on BFC-BKT and related materials will be continued, with a more general approach to systematically study ferrimagnetism in ferroelectrics especially in Co substituted $BiFeO_3$.

Following is a summary of the planned work that was grouped into three objectives:

I.   Investigation of the exact structure of MFC in BFC-BKT
II.   Investigation of mechanisms of strong magnetoelectric coupling in BFC-KBT
III. Systematic investigation of the systems $(BiFe_xCo_{1-x}O_3)_y$-$(K_{1/2}Bi_{1/2}TiO_3)_{1-y}$ and $BiFe_xCo_{1-x}O_3$ also as thin-film materials

Objective I. will primarily deal with further characterizing the MFC to better understand their structure and composition with methods such as transmission electron-microscopy (TEM). A thin lamella will be cut selectively out of an interface area between an MFC and the surrounding matrix via focused ion beam (FIB) to study the chemical composition and structure via EDX and selected area electron diffraction (SAED). Furthermore, X-ray magnetic circular dichroism (XMCD) in combination with photoemission electron microscopy (PEEM) experiments are planned at synchrotron sources, to study the magnetism with element specific information.

Objective II. is focussed on investigation of the underlying mechanisms involved in ME coupling of the MFC. Here, more detailed PFM under magnetic field in combination with electron backscattering diffraction (EBSD) experiments are planned, to gain information on the local crystallographic and polar orientation of MFC. Intrinsic ME coupling for example, is only allowed for certain crystal symmetries. Therefore, these experiments could give insight into the mechanisms of ME coupling.

In Objective III., additional compositions will be prepared and multiferroic properties investigated. It is planned that further ceramics will be prepared. Additionally, it is planned to prepare BFC-BKT thin-films via pulsed laser deposition (PLD) in close collaboration with the University of Leeds. Here, a hierarchical system will be employed where only necessary measurements such as magnetometry will be carried out on all samples, whereas more detailed and time consuming investigations are carried out only on the most promising compositions to reduce unnecessary efforts.

8   Bibliography

[1]   N. D'Souza, J. Atulasimha, and S. Bandyopadhyay, "Four-state nanomagnetic logic using multiferroics," *J. Phys. D Appl. Phys.* , vol. 44, no. 26, p. 265001, 2011.

[2]   E. Lage, C. Kirchhof, V. Hrkac, L. Kienle, R. Jahns, R. Knöchel, E. Quandt, and D. Meyners, "Exchange biasing of magnetoelectric composites," *Nat. Mater.* , vol. 11, no. 6, pp. 523–529, 2012.

[3]   C. Israel, N. D. Mathur, and J. F. Scott, "A one-cent room-temperature magnetoelectric sensor," *Nat. Mater.* , vol. 7, no. 2, pp. 93–94, 2008.

[4]   X. Chen, A. Hochstrat, P. Borisov, and W. Kleemann, "Magnetoelectric exchange bias systems in spintronics," *Appl. Phys. Lett.* , vol. 89, no. 20, p. 202508, 2006.

[5]   M. Bibes and A. Barthelemy, "Multiferroics: Towards a magnetoelectric memory," *Nat. Mater.* , vol. 7, no. 6, pp. 425–426, 2008.

[6]   M. Gajek, M. Bibes, S. Fusil, K. Bouzehouane, J. Fontcuberta, A. Barthelemy, and A. Fert, "Tunnel junctions with multiferroic barriers," *Nat Mater*, vol. 6, no. 4, pp. 296–302, 2007.

[7]   M. Fiebig, "Revival of the magnetoelectric effect," *J. Phys. D Appl. Phys.* , vol. 38, no. 8, p. R123, 2005.

[8]   A. Kojima, K. Teshima, Y. Shirai, and T. Miyasaka, "Organometal halide perovskites as visible-light sensitizers for photovoltaic cells," *J. Am. Chem. Soc.*, vol. 131, no. 17, pp. 6050–6051, 2009.

[9]   B. Jaffe, R. Cook, and H. Jaffe, *Piezoelectric ceramics*. London: Academic press, 1971.

[10]   D. Damjanovic, "Ferroelectric, dielectric and piezoelectric properties of ferroelectric thin films and ceramics," *Reports Prog. Phys.*, vol. 61, p. 1267, 1998.

[11]   A. J. Moulson and J. M. Herbert, *Electroceramics: Materials, Properties, Applications*. Chichester: John Wiley & Sons Ltd, 2003.

[12] S. A. Mabud, "The morphotropic phase boundary in PZT solid solutions," *J. Appl. Crystallogr.*, vol. 13, no. 3, pp. 211–216, Jun. 1980.

[13] G. Shirane, R. Pepinsky, and B. C. Frazer, "X-ray and neutron diffraction study of ferroelectric $PbTiO_3$," *Acta Crystallogr.*, vol. 9, no. 2, pp. 131–140, Feb. 1956.

[14] R. W. Whatmore and A. M. Glazer, "Structural phase transitions in lead zirconate," *J. Phys. C Solid State Phys.*, vol. 12, no. 8, p. 1505, 1979.

[15] D. I. Woodward, J. Knudsen, and I. M. Reaney, "Review of crystal and domain structures in the $PbZr_xTi_{1-x}O_3$ solid solution," *Phys. Rev. B*, vol. 72, no. 10, p. 104110, 2005.

[16] B. Noheda, D. E. Cox, G. Shirane, J. A. Gonzalo, L. E. Cross, and S.-E. Park, "A monoclinic ferroelectric phase in the $Pb(Zr_xTi_{1-x})O_3$ solid solution," *Appl. Phys. Lett.*, vol. 74, no. 14, 1999.

[17] L. Bellaiche, A. García, and D. Vanderbilt, "Finite-Temperature Properties of $Pb(Zr_xTi_{1-x})O_3$ Alloys from First Principles," *Physical Review Letters*, vol. 84, no. 23. pp. 5427–5430, 2000.

[18] S. Zhang, R. Xia, and T. R. Shrout, "Lead-free piezoelectric ceramics vs. PZT?," *J. Electroceramics*, vol. 19, no. 4, pp. 251–257, 2007.

[19] L. E. Cross, "Relaxor ferroelectrics," *Ferroelectrics*, vol. 76, no. 1. pp. 241–267, 1987.

[20] W. Kleemann, "The relaxor enigma — charge disorder and random fields in ferroelectrics," *J. Mater. Sci.*, vol. 41, no. 1, pp. 129–136, 2006.

[21] Y. Imry and S. Ma, "Random-Field Instability of the Ordered State of Continuous Symmetry," *Phys. Rev. Lett.* , vol. 35, no. 21, pp. 1399–1401, 1975.

[22] V. Westphal, W. Kleemann, and M. D. Glinchuk, "Diffuse phase transitions and random-field-induced domain states of the "relaxor" ferroelectric $PbMg_{1/3}Nb_{2/3}O_3$," *Phys. Rev. Lett.*, vol. 68, no. 6, pp. 847–850, 1992.

[23] D. Phelan, C. Stock, J. A. Rodriguez-Rivera, S. Chi, J. Leão, X. Long, Y. Xie, A. A. Bokov, Z.-G. Ye, P. Ganesh, and P. M. Gehring, "Role of random electric fields in relaxors ," *Proc. Natl. Acad. Sci. U S A.*, vol. 111, no. 5, pp. 1754–1759, 2014.

[24] E. Sun and W. Cao, "Relaxor-based ferroelectric single crystals: Growth, domain engineering, characterization and applications," *Progress in Materials Science*, vol. 65. Elsevier Ltd, pp. 124–210, 2014.

[25] V. V Shvartsman and D. C. Lupascu, "Lead-Free Relaxor Ferroelectrics," *J. Am. Ceram. Soc.*, vol. 95, no. 1, pp. 1–26, 2012.

[26] D. Viehland, S. J. Jang, L. E. Cross, and M. Wuttig, "Freezing of the polarization fluctuations in lead magnesium niobate relaxors," *J. Appl. Phys.*, vol. 68, no. 6, 1990.

[27] D. Viehland, M. Wuttig, and L. E. Cross, "The glassy behavior of relaxor ferroelectrics," *Ferroelectrics*, vol. 120, no. 1, pp. 71–77, Aug. 1991.

[28] W. Kleemann, "Glassy Phenomena in Relaxor Ferroelectrics," in *Mesoscopic Phenomena in Multifunctional Materials*, vol. 198, A. Saxena and A. Planes, Eds. Springer Berlin Heidelberg, 2014, pp. 249–269.

[29] L. Boltzmann, "Ueber einige Fragen der kinetischen Gastheorie," in *Sitzungsberichte der Kgl. Akademie der Wissenschaften in Wien.*, 1887, pp. 891–918.

[30] R. Dittmer, D. Gobeljic, W. Jo, V. V Shvartsman, D. C. Lupascu, J. L. Jones, and J. Rödel, "Ergodicity reflected in macroscopic and microscopic field-dependent behavior of BNT-based relaxors," *J. Appl. Phys.* , vol. 115, no. 8, p. -, 2014.

[31] T. Moriya, "Anisotropic superexchange interaction and weak ferromagnetism," *Phys. Rev.*, vol. 120, no. 1, pp. 91–98, 1960.

[32] J. Wang, J. B. Neaton, H. Zheng, V. Nagarajan, S. B. Ogale, B. Liu, D. Viehland, V. Vaithyanathan, D. G. Schlom, U. V Waghmare, N. A. Spaldin, K. M. Rabe, M. Wuttig, and R. Ramesh, "Epitaxial $BiFeO_3$ multiferroic thin film heterostructures.," *Science*, vol. 299, no. 5613, pp. 1719–1722, 2003.

[33] D. Lebeugle, D. Colson, A. Forget, M. Viret, A. M. Bataille, and A. Gukasov, "Electric-Field-Induced Spin Flop in $BiFeO_3$ Single Crystals at Room Temperature," *Physical Review Letters*, vol. 100, no. 22. 2008.

[34] V. Blanco-Gutiérrez, M. J. Torralvo, R. Sáez-Puche, and P. Bonville, "Magnetic properties of solvothermally synthesized $ZnFe_2O_4$ nanoparticles," *J. Phys. Conf. Ser.*, vol. 200, no. 7, p. 72013, 2010.

[35] M. Artus, L. Ben Tahar, F. Herbst, L. Smiri, F. Villain, N. Yaacoub, J.-M. Grenèche, S. Ammar, and F. Fiévet, "Size-dependent magnetic properties of $CoFe_2O_4$ nanoparticles prepared in polyol," *J. Phys. Condens. Matter*, vol. 23, no. 50, p. 506001, 2011.

[36] G. F. Goya, T. S. Berquó, F. C. Fonseca, and M. P. Morales, "Static and dynamic magnetic properties of spherical magnetite nanoparticles," *J. Appl. Phys.* , vol. 94, no. 5, pp. 3520–3528, 2003.

[37] B. Babic-Stojic, V. Jokanovic, D. Milivojevic, Z. Jaglicic, D. Makovec, N. Jovic, and M. Marinovic-Cincovic, "Magnetic and Structural Studies of $CoFe_2O_4$ Nanoparticles Suspended in an Organic Liquid," *J. Nanomater.*, vol. 2013, p. 9, 2013.

[38] C. Liu, A. J. Rondinone, and Z. J. Zhang, "Synthesis of magnetic spinel ferrite $CoFe_2O_4$ nanoparticles from ferric salt and characterization of the size-dependent superparamagnetic properties," *Pure Appl. Chem.*, vol. 72, pp. 37–45, 2000.

[39] M. Soda, M. Matsuura, Y. Wakabayashi, and K. Hirota, "Superparamagnetism induced by polar nanoregions in relaxor ferroelectric $(1-x)BiFeO_3$-$x(BaTiO_3)$," *J. Phys. Soc. Japan*, vol. 80, no. 4, pp. 43704–43705, 2011.

[40] W. Kleemann, V. V Shvartsman, P. Borisov, and A. Kania, "Coexistence of Antiferromagnetic and Spin Cluster Glass Order in the Magnetoelectric Relaxor Multiferroic $PbFe_{0.5}Nb_{0.5}O_3$," *Phys. Rev. Lett.*, vol. 105, no. 25, p. 257202, Dec. 2010.

[41] M. Correa, A. Kumar, R. S. Katiyar, and C. Rinaldi, "Observation of magnetoelectric coupling in glassy epitaxial $PbFe_{0.5}Nb_{0.5}O_3$ thin films," *Appl. Phys. Lett.*, vol. 93, no. 19, p. -, 2008.

[42] W. Peng, N. Lemée, M. Karkut, B. Dkhil, V. V Shvartsman, P. Borisov, W. Kleemann, J. Holc, M. Kosec, and R. Blinc, "Spin-lattice coupling in multiferroic $Pb(Fe_{1/2}Nb_{1/2})O_3$ thin films," *Appl. Phys. Lett.*, vol. 94, no.

1, p. -, 2009.

[43] H. Schmid, "Multi-ferroic magnetoelectrics," *Ferroelectrics*, vol. 162, no. 1. pp. 317–338, 1994.

[44] N. A. Spaldin and M. Fiebig, "Materials science. The renaissance of magnetoelectric multiferroics.," *Science*, vol. 309, no. 5733, pp. 391–392, 2005.

[45] J. P. Rivera, "A short review of the magnetoelectric effect and related experimental techniques on single phase (multi-) ferroics," *European Physical Journal B*, vol. 71, no. 3. pp. 299–313, 2009.

[46] N. Izyumskaya, Y. Alivov, and H. Morkoç, "Oxides, Oxides, and More Oxides: High-κ Oxides, Ferroelectrics, Ferromagnetics, and Multiferroics," *Crit. Rev. Solid State Mater. Sci.* , vol. 34, no. 3–4, pp. 89–179, 2009.

[47] N. A. Hill, "Why Are There so Few Magnetic Ferroelectrics?," *J. Phys. Chem. B* , vol. 104, no. 29, pp. 6694–6709, 2000.

[48] G. A. Smolenskiĭ and I. E. Chupis, "Ferroelectromagnets," *Sov. Phys. Uspekhi*, vol. 25, no. 7, p. 475, 1982.

[49] D. A. Sanchez, N. Ortega, A. Kumar, R. Roque-Malherbe, R. Polanco, J. F. Scott, and R. S. Katiyar, "Symmetries and multiferroic properties of novel room-temperature magnetoelectrics: Lead iron tantalate – lead zirconate titanate (PFT/PZT)," *AIP Adv.*, vol. 1, no. 4, p. -, 2011.

[50] D. A. Sanchez, N. Ortega, A. Kumar, G. Sreenivasulu, R. S. Katiyar, J. F. Scott, D. M. Evans, M. Arredondo-Arechavala, A. Schilling, and J. M. Gregg, "Room-temperature single phase multiferroic magnetoelectrics: Pb(Fe, M)$_x$(Zr,Ti)$_{1-x}$O$_3$ [M = Ta, Nb]," *J. Appl. Phys.*, vol. 113, no. 7, p. -, 2013.

[51] L. Keeney, T. Maity, M. Schmidt, A. Amann, N. Deepak, N. Petkov, S. Roy, M. E. Pemble, and R. W. Whatmore, "Magnetic Field-Induced Ferroelectric Switching in Multiferroic Aurivillius Phase Thin Films at Room Temperature," *J. Am. Ceram. Soc.*, vol. 96, no. 8, pp. 2339–2357, 2013.

[52] T. Goto, T. Kimura, G. Lawes, A. P. Ramirez, and Y. Tokura, "Ferroelectricity and giant magnetocapacitance in perovskite rare-earth manganites," *Phys. Rev. Lett.*, vol. 92, no. 25 I, pp. 257201–1,

2004.

[53]   E. Ascher, H. Rieder, H. Schmid, and H. Stössel, "Some properties of ferromagnetoelectric nickel-iodine boracite, $Ni_3B_7O_{13}I$," *J. Appl. Phys.*, vol. 37, no. 3, pp. 1404–1405, 1966.

[54]   R. Hornreich and S. Shtrikman, "Statistical Mechanics and Origin of the Magnetoelectric Effect in Cr_2O_3," *Phys. Rev.*, vol. 161, no. 2, pp. 506–512, Sep. 1967.

[55]   M. Gajek, H. Bea, M. Bibes, K. Bouzehouane, S. Fusil, G. Herranz, E. Jacquet, J. Contour, M. Varela, J. Fontcuberta, and A. Fert, "Spintronics with multiferroics," in *INTERMAG 2006 - IEEE International Magnetics Conference*, 2006, p. 726.

[56]   L. W. Martin, S. P. Crane, Y.-H. Chu, M. B. Holcomb, M. Gajek, M. Huijben, C.-H. Yang, N. Balke, and R. Ramesh, "Multiferroics and magnetoelectrics: thin-films and nanostructures," *J. Phys. Condens. Matter*, vol. 20, no. 43, p. 434220, 2008.

[57]   L. W. Martin and R. Ramesh, "Multiferroic and magnetoelectric heterostructures," *Acta Mater. *, vol. 60, no. 6–7, pp. 2449–2470, 2012.

[58]   W. Eerenstein, N. D. Mathur, and J. F. Scott, "Multiferroic and magnetoelectric materials," *Nature*, vol. 442, no. 7104, pp. 759–765, 2006.

[59]   J. Ryu, A. V. Carazo, K. Uchino, and H. E. Kim, "Magnetoelectric properties in piezoelectric and magnetostrictive laminate composites," *Japanese J. Appl. Physics, Part 1 Regul. Pap. Short Notes Rev. Pap.*, vol. 40, no. 8, pp. 4948–4951, 2001.

[60]   H. Zheng, J. Wang, S. E. Lofland, Z. Ma, L. Mohaddes-Ardabili, T. Zhao, L. Salamanca-Riba, S. R. Shinde, S. B. Ogale, F. Bai, D. Viehland, Y. Jia, D. G. Schlom, M. Wuttig, A. Roytburd, and R. Ramesh, "Multiferroic $BaTiO_3$-$CoFe_2O_4$ Nanostructures.," *Science*, vol. 303, no. 5658, pp. 661–663, 2004.

[61]   J. T. Heron, J. L. Bosse, Q. He, Y. Gao, M. Trassin, L. Ye, J. D. Clarkson, C. Wang, J. Liu, S. Salahuddin, D. C. Ralph, D. G. Schlom, J. Iniguez, B. D. Huey, and R. Ramesh, "Deterministic switching of ferromagnetism at room temperature using an electric field," *Nature*, vol. 516, no. 7531, pp. 370–373, Dec. 2014.

[62] N. Hur, S. Park, P. A. Sharma, J. S. Ahn, S. Guha, and S. W. Cheong, "Electric polarization reversal and memory in a multiferroic material induced by magnetic fields," *Nature*, vol. 429, no. 6990, pp. 392–395, 2004.

[63] Y. Kitagawa, Y. Hiraoka, T. Honda, T. Ishikura, H. Nakamura, and T. Kimura, "Low-field magnetoelectric effect at room temperature," *Nat. Mater.* , vol. 9, no. 10, pp. 797–802, 2010.

[64] J. F. Scott, "Room-temperature multiferroic magnetoelectrics," *NPG Asia Mater*, vol. 5, p. e72, 2013.

[65] W. Eerenstein, M. Wiora, J. L. Prieto, J. F. Scott, and N. D. Mathur, "Giant sharp and persistent converse magnetoelectric effects in multiferroic epitaxial heterostructures," *Nat. Mater.* , vol. 6, no. 5, pp. 348–351, 2007.

[66] C. A. F. Vaz, "Electric field control of magnetism in multiferroic heterostructures," *J. Phys. Condens. Matter* , vol. 24, no. 33, p. 333201, 2012.

[67] D. M. Evans, A. Schilling, A. Kumar, D. Sanchez, N. Ortega, M. Arredondo, R. S. Katiyar, J. M. Gregg, and J. F. Scott, "Magnetic switching of ferroelectric domains at room temperature in multiferroic PZTFT," *Nat. Communations*, vol. 4, p. 1534, 2013.

[68] D. M. Evans, A. Schilling, A. Kumar, D. Sanchez, N. Ortega, R. S. Katiyar, J. F. Scott, and J. M. Gregg, "Switching ferroelectric domain configurations using both electric and magnetic fields in $Pb(ZrTi)O_3$–$Pb(FeTa)O_3$ single-crystal lamellae," *Phil.Trans.R.Soc.A*, vol. 372, p. 20120450, 2014.

[69] M. R. Suchomel, C. I. Thomas, M. Allix, M. J. Rosseinsky, A. M. Fogg, and M. F. Thomas, "High pressure bulk synthesis and characterization of the predicted multiferroic $BiFe_{1/2}Cr_{1/2}O_3$," *Appl. Phys. Lett.*, vol. 90, no. 11, p. -, 2007.

[70] R. Nechache, C. Harnagea, and A. Pignolet, "Multiferroic properties—structure relationships in epitaxial Bi_2FeCrO_6 thin films: recent developments," *J. Phys. Condens. Matter*, vol. 24, no. 9, p. 96001, 2012.

[71] R. Nechache, C. Harnagea, A. Pignolet, F. Normandin, T. Veres, L.-P. Carignan, and D. Ménard, "Growth, structure, and properties of epitaxial thin films of first-principles predicted multiferroic Bi_2FeCrO_6,"

Appl. Phys. Lett., vol. 89, no. 10, p. -, 2006.

[72] R. Nechache, C. Harnagea, L.-P. Carignan, O. Gautreau, L. Pintilie, M. P. Singh, D. Ménard, P. Fournier, M. Alexe, and A. Pignolet, "Epitaxial thin films of the multiferroic double perovskite Bi_2FeCrO_6 grown on (100)-oriented $SrTiO_3$ substrates: Growth, characterization, and optimization," *J. Appl. Phys.*, vol. 105, no. 6, p. -, 2009.

[73] Z. Y. Zhao, M. F. Liu, X. Li, L. Lin, Z. B. Yan, S. Dong, and J.-M. Liu, "Experimental observation of ferrielectricity in multiferroic $DyMn_2O_5$," *Sci. Rep.*, vol. 4, Feb. 2014.

[74] Y.-H. Chu, L. W. Martin, M. B. Holcomb, and R. Ramesh, "Controlling magnetism with multiferroics," *Mater. Today*, vol. 10, no. 10, pp. 16–23, 2007.

[75] G. Catalan and J. F. Scott, "Physics and Applications of Bismuth Ferrite," *Advan. Mater.*, vol. 21, no. 24, pp. 2463–2485, 2009.

[76] I. Sosnowska, M. Azuma, R. Przeniosło, D. Wardecki, W. Chen, K. Oka, and Y. Shimakawa, "Crystal and Magnetic Structure in Co-Substituted $BiFeO_3$," *Inorg. Chem.*, vol. 52, no. 22, pp. 13269–13277, 2013.

[77] G. L. Ye, J. M. Xu, J. A. Alonso, and Z. X. Wang, "Preparation of $BiFe_{1-x}Co_xO_3$ Ceramics via a Simple Solid Method and Enhanced Multiferroic Properties," in *Materials Engineering for Advanced Technologies (ICMEAT 2012)*, 2013.

[78] M. Kubota, K. Oka, H. Yabuta, K. Miura, and M. Azuma, "Structure and Magnetic Properties of $BiFe_{1-x}Co_xO_3$ and $Bi_{0.9}Sm_{0.1}Fe_{1-x}Co_xO_3$," *Inorg. Chem.*, vol. 52, no. 18, pp. 10698–10704, 2013.

[79] I. Coondoo, N. Panwar, A. Tomar, I. Bdikin, A. L. Kholkin, V. S. Puli, and R. S. Katiyar, "Improved magnetic and piezoresponse behavior of cobalt substituted $BiFeO_3$ thin film," *Thin Solid Films*, vol. 520, no. 21, pp. 6493–6498, 2012.

[80] K. Oka, M. Azuma, W. Chen, H. Yusa, A. A. Belik, E. Takayama-Muromachi, M. Mizumaki, N. Ishimatsu, N. Hiraoka, M. Tsujimoto, M. G. Tucker, J. P. Attfield, and Y. Shimakawa, "Pressure-Induced Spin-State Transition in $BiCoO_3$," *J. Am. Chem. Soc.*, vol. 132, no. 27, pp. 9438–9443, 2010.

[81] T. Sudayama, Y. Wakisaka, T. Mizokawa, H. Wadati, G. A. Sawatzky, D. G. Hawthorn, T. Z. Regier, K. Oka, M. Azuma, and Y. Shimakawa, "Co-O-O-Co superexchange pathways enhanced by small charge-transfer energy in multiferroic $BiCoO_3$," *Phys. Rev. B*, vol. 83, no. 23, p. 235105, 2011.

[82] N. T. Tho, T. Kanashima, and M. Okuyama, "Leakage Current Reduction and Ferroelectric Property of $BiFe_{(1-x)}Co_xO_3$ Thin Films Prepared by Chemical Solution Deposition Using Iterative Rapid Thermal Annealing at Approximately 520 °C," *Jpn. J. Appl. Phys.*, vol. 49, no. 9R, p. 95803, 2010.

[83] O. N. Razumovskaya, T. B. Kuleshova, and L. M. Rudkovskaya, "Formation Reactions of $BiFeO_3$, $(K_{0.5}Bi_{0.5})TiO_3$ and $(Na_{0.5}Bi_{0.5})TiO_3$," *Inorg. Mater.*, vol. 19, no. 1, pp. 96–99, 1983.

[84] Y. Hiruma, R. Aoyagi, H. Nagata, and T. Takenaka, "Ferroelectric and Piezoelectric Properties of $(Bi_{0.5}K_{0.5})TiO_3$ Ceramics," *Jpn. J. Appl. Phys.*, vol. 44, no. 7R, p. 5040, 2005.

[85] W. Zuo, R. Zuo, and W. Zhao, "Phase transition behavior and electrical properties of lead-free $(Bi_{0.5}K_{0.5})TiO_3$–$LiNbO_3$ relaxor ferroelectric ceramics," *Ceram. Int.*, vol. 39, no. 1, pp. 725–730, 2013.

[86] H. Matsuo, Y. Noguchi, M. Miyayama, M. Suzuki, A. Watanabe, S. Sasabe, T. Ozaki, S. Mori, S. Torii, and T. Kamiyama, "Structural and piezoelectric properties of high-density $(Bi_{0.5}K_{0.5})TiO_3$ –$BiFeO_3$ ceramics," *J. Appl. Phys.*, vol. 108, no. 10, 2010.

[87] J. T. Bennett, "Development of bismuth ferrite derived piezoelectric ceramics for high temperature applications," University of Leeds, 2014.

[88] T. Ozaki, H. Matsuo, Y. Noguchi, M. Miyayama, and S. Mori, "Microstructures Related to Ferroelectric Properties in $(Bi_{0.5}K_{0.5})TiO_3$ –$BiFeO_3$," *Jpn. J. Appl. Phys.*, vol. 49, no. 9S, p. 09MC05, 2010.

[89] M. I. Morozov, M.-A. Einarsrud, and T. Grande, "Polarization and strain response in $(Bi_{0.5}K_{0.5})TiO_3$ –$BiFeO_3$ ceramics," *Appl. Phys. Lett.*, vol. 101, no. 25, p. -, 2012.

[90] J. M. Kim, Y. S. Sung, J. H. Cho, T. K. Song, M. H. Kim, H. H. Chong, T. G. Park, D. Do, and S. S. Kim, "Piezoelectric and Dielectric Properties of Lead-Free (1- x)$(Bi_{0.5}K_{0.5})TiO_3$ –$xBiFeO_3$ Ceramics," *Ferroelectrics*, vol. 404, no. 1, pp. 88–92, 2010.

[91] J. Bennett, A. J. Bell, T. J. Stevenson, R. I. Smith, I. Sterianou, I. M. Reaney, and T. P. Comyn, "Multiferroic properties of $BiFeO_3$-$(K_{0.5}Bi_{0.5})TiO_3$ ceramics," *Mater. Lett.*, vol. 94, no. 0, pp. 172–175, 2013.

[92] A. Kumar, R. S. Katiyar, and J. F. Scott, "Fabrication and characterization of the multiferroic birelaxor lead-iron-tungstate/lead-zirconate-titanate," *J. Appl. Phys.*, vol. 108, no. 6, 2010.

[93] K. S. Kempa, Savinov M, Maryško M, Frait Z, Vaněk P, Tomczyk M, Vilarinho PM., "Bulk dielectric and magnetic properties of PFW-PZT ceramics: absence of magnetically switched-off polarization.," *J Phys Condens Matter.*, vol. 22, p. 445902 (5pp), 2010.

[94] D. Pajić, M. Jagodič, Z. Jagličić, J. Holc, M. Kosec, and Z. Trontelj, "Competing antiferromagnetism and local magnetic order in the bulk ceramic PZT–PFW multiferroic system: searching for the most promising ratio between PZT and PFW," *J. Phys. D Appl. Phys.* , vol. 46, no. 45, p. 455001, 2013.

[95] S. A. Ivanov, S. G. Eriksson, R. Tellgren, and H. Rundlöf, "Neutron powder diffraction study of the magnetoelectric relaxor $PbFe_{2/3}W_{1/3}O_3$," *Mater. Res. Bull.*, vol. 39, no. 14–15, pp. 2317–2328, 2004.

[96] A. Kumar, G. L. Sharma, R. S. Katiyar, R. Pirc, R. Blinc, and J. F. Scott, "Magnetic control of large room-temperature polarization," *J. Phys. Condens. Matter* , vol. 21, no. 38, p. 382204, 2009.

[97] R. Weis and T. Gaylord, "Lithium Niobate: Summary of Physical Properties and Crystal Structure R.," *Appl. Phys. A Mater. Sci. Process.*, vol. 37, no. 4, pp. 191–203, 1985.

[98] T. P. Comyn, T. Stevenson, and A. J. Bell, "Piezoelectric properties of $BiFeO_3$-$PbTiO_3$ ceramics," in *Applications of Ferroelectrics, 2004. ISAF-04. 2004 14th IEEE International Symposium on*, 2004, pp. 122–125.

[99] A. J. Bell, A. X. Levander, S. L. Turner, and T. P. Comyn, "Internal stress and phase coexistence in bismuth ferrite-lead titanate ceramics," in *IEEE International Symposium on Applications of Ferroelectrics*, 2007, pp. 406–409.

[100] A. J. Royles, A. J. Bell, A. P. Jephcoat, A. K. Kleppe, S. J. Milne, and T. P. Comyn, "Electric-field-induced phase switching in the lead free piezoelectric potassium sodium bismuth titanate," *Appl. Phys. Lett.*,

vol. 97, no. 13, 2010.

[101] T. Stevenson, T. P. Comyn, A. Daoud-Aladine, and A. J. Bell, "Change in periodicity of the incommensurate magnetic order towards commensurate order in bismuth ferrite lead titanate," *J. Magn. Magn. Mater.*, vol. 322, no. 22, 2010.

[102] G. Binnig, C. F. Quate, and C. Gerber, "Atomic Force Microscope," *Phys. Rev. Lett.* , vol. 56, no. 9, pp. 930–933, 1986.

[103] Yashvant, "AFMsetup." [Online]. Available: http://commons.wikimedia.org/wiki/File:AFMsetup.jpg#/media/File:AFMsetup.jpg. [Accessed: 02-Jun-2015].

[104] Steff, "Schema MEB (en)." [Online]. Available: http://commons.wikimedia.org/wiki/File:Schema_MEB_(en).svg#/media/File:Sc. [Accessed: 02-Jun-2015].

[105] J. P. Hofmann, M. Rohnke, and B. M. Weckhuysen, "Recent advances in secondary ion mass spectrometry of solid acid catalysts: large zeolite crystals under bombardment," *Phys. Chem. Chem. Phys.*, vol. 16, no. 12, pp. 5465–5474, 2014.

[106] J. Pisonero, B. Fernandez, and D. Gunther, "Critical revision of GD-MS, LA-ICP-MS and SIMS as inorganic mass spectrometric techniques for direct solid analysis," *J. Anal. At. Spectrom.*, vol. 24, no. 9, pp. 1145–1160, 2009.

[107] Loi_de_bragg, "Braggs Law." [Online]. Available: http://commons.wikimedia.org/wiki/File:Braggs_Law.svg#/media/File:Braggs_Law.svg. [Accessed: 03-Jun-2015].

[108] Meisam, "Sawyer–Tower." [Online]. Available: http://commons.wikimedia.org/wiki/File:Sawyer%E2%80%93Tower.png#/media/File:Sawyer%E2%80%93Tower.png. [Accessed: 04-Jun-2015].

[109] J. F. Scott, "Ferroelectrics go bananas," *J. Phys. Condens. Matter*, vol. 20, no. 2, p. 21001, 2008.

[110] P. Güthner and K. Dransfeld, "Local poling of ferroelectric polymers by scanning force microscopy," *Appl. Phys. Lett.*, vol. 61, no. 9, pp. 1137–1139, 1992.

[111] A. Gruverman, O. Auciello, and H. Tokumoto, "Imaging and Control of Domain Structures in Ferroelectric Thin Films Via Scanning Force Microscopy," *Annu. Rev. Mater. Sci.*, vol. 28, pp. 101–123, 1998.

[112] E. Soergel, "Piezoresponse force microscopy (PFM)," *J. Phys. D Appl. Phys.* , vol. 44, no. 46, p. 464003, 2011.

[113] A. Gruverman, O. Kolosov, J. Hatano, K. Takahashi, and H. Tokumoto, "Domain structure and polarization reversal in ferroelectrics studied by atomic force microscopy," *J. Vac. Sci. & Technol. B*, vol. 13, no. 3, pp. 1095–1099, 1995.

[114] A. Gruverman, B. J. Rodriguez, C. Dehoff, J. D. Waldrep, A. I. Kingon, R. J. Nemanich, and J. S. Cross, "Direct studies of domain switching dynamics in thin film ferroelectric capacitors," *Appl. Phys. Lett.* , vol. 87, no. 8, p. -, 2005.

[115] B. J. Rodriguez, S. Choudhury, Y. H. Chu, A. Bhattacharyya, S. Jesse, K. Seal, A. P. Baddorf, R. Ramesh, L.-Q. Chen, and S. V Kalinin, "Unraveling Deterministic Mesoscopic Polarization Switching Mechanisms: Spatially Resolved Studies of a Tilt Grain Boundary in Bismuth Ferrite," *Adv. Funct. Mater.* , vol. 19, no. 13, pp. 2053–2063, 2009.

[116] S. V Kalinin, S. Jesse, B. J. Rodriguez, J. Shin, A. P. Baddorf, H. N. Lee, A. Borisevich, and S. J. Pennycook, "Spatial resolution, information limit, and contrast transfer in piezoresponse force microscopy," *Nanotechnology*, vol. 17, no. 14, p. 3400, 2006.

[117] B. J. Rodriguez, C. Callahan, S. V Kalinin, and R. Proksch, "Dual-frequency resonance-tracking atomic force microscopy," *Nanotechnology*, vol. 18, no. 47, p. 475504, 2007.

[118] S. Jesse, S. Guo, A. Kumar, B. J. Rodriguez, R. Proksch, and S. V Kalinin, "Resolution theory, and static and frequency-dependent cross-talk in piezoresponse force microscopy," *Nanotechnology*, vol. 21, no. 40, p. 405703, 2010.

[119] A. L. Kholkin, I. K. Bdikin, D. A. Kiselev, V. V Shvartsman, and S.-H. Kim, "Nanoscale characterization of polycrystalline ferroelectric materials for piezoelectric applications," *J. Electroceramics*, vol. 19, no. 1, pp. 83–96, 2007.

[120] P. Lehnen, J. Dec, and W. Kleemann, "Ferroelectric domain structures of $PbTiO_3$ studied by scanning force microscopy," *J. Phys. D. Appl.*

Phys., vol. 33, no. 15, p. 1932, 2000.

[121] "Piezoresponse force microscopy." [Online]. Available: https://www.asylumresearch.com/Applications/PFMAppNote/PFMImages/vertical_deflection0139.jpg. [Accessed: 08-Jun-2015].

[122] S. Jesse and S. V Kalinin, "Band excitation in scanning probe microscopy: sines of change," *Journal of Physics D: Applied Physics*, vol. 44, no. 46. p. 464006, 2011.

[123] F. Johann, Á. Hoffmann, and E. Soergel, "Impact of electrostatic forces in contact-mode scanning force microscopy," *Phys. Rev. B*, vol. 81, no. 9, p. 94109, 2010.

[124] T. Jungk, Á. Hoffmann, and E. Soergel, "Consequences of the background in piezoresponse force microscopy on the imaging of ferroelectric domain structures," *J. Microsc.*, vol. 227, no. 1, pp. 72–78, 2007.

[125] T. Yamada, N. Niizeki, and H. Toyoda, "Piezoelectric and Elastic Properties of Lithium Niobate Single Crystals," *Jpn. J. Appl. Phys.*, vol. 6, no. 2, p. 151, 1967.

[126] D. Nečas and P. Klapetek, "Gwyddion: an open-source software for SPM data analysis," *Cent. Eur. J. Phys.* , vol. 10, no. 1, pp. 181–188, 2012.

[127] R0oland, "VSM en." [Online]. Available: http://commons.wikimedia.org/wiki/File:VSM_en.svg#/media/File:VSM _en.svg. [Accessed: 08-Jun-2015].

[128] S. Bedanta and W. Kleemann, "Supermagnetism," *J. Phys. D. Appl. Phys.*, vol. 42, no. 1, p. 013001, 2009.

[129] Y. Martin and H. K. Wickramasinghe, "Magnetic imaging by '"force microscopy"' with 1000 Å resolution," *Appl. Phys. Lett.*, vol. 50, no. 20, 1987.

[130] "Magnetic force microscopy." [Online]. Available: http://blog.brukerafmprobes.com/wp-content/uploads/2011/06/p29-Magnetic-Force-Microscopy-MFM-main.jpg. [Accessed: 08-Jun-2015].

[131] J. M. D. Coey, "10.4.2 Magneto-optic and electron-optic methods," in

Magnetism and magnetic materials, Cambridge: Cambridge University Press, 2009, pp. 356–360.

[132] J. McCord and A. Hubert, "Normalized Differential Kerr Microscopy An Advanced Method for Magnetic Imaging," *Phys. status solidi*, vol. 171, no. 2, pp. 555–562, 1999.

[133] Hokur, "Mossbauer -Magnetting Splitting." [Online]. Available: http://commons.wikimedia.org/wiki/File:Mossbauer_-Magnetting_Splitting.jpg#/media/File:Mossbauer_-Magnetting_Splitting.jpg. [Accessed: 08-Jun-2015].

[134] T. C. Gibb, *Principles of Mössbauer Spectroscopy*. London: Chapman and Hall, 1976.

[135] "Mössbauer Spectroscopy Group, Royal Society of Chemistry (RSC) website." [Online]. Available: http://www.rsc.org/Membership/Networking/InterestGroups/Mossbauer Spect/intro.asp. [Accessed: 09-Jun-2015].

[136] Y. A. Izyumov, V. E. Naish, and R. P. Ozerov, *Neutron diffraction of magnetic materials*. New York: Consultants Bureau, 1991.

[137] R. (Iowa S. U. McQueeney, "Magnetic neutron diffraction." [Online]. Available: http://canfield.physics.iastate.edu/course/EM_16.pdf. [Accessed: 09-Jun-2015].

[138] ILL, "D1B - High resolution neutron two-axis powder diffractometer." [Online]. Available: http://www.ill.eu/instruments-support/instruments-groups/instruments/d1b/description/instrument-layout/. [Accessed: 30-Apr-2015].

[139] "Resolution function of D1B diffractometer." [Online]. Available: http://www.ill.eu/instruments-support/instruments-groups/instruments/d1b/more/characteristics/. [Accessed: 07-May-2015].

[140] T. Jungk, Á. Hoffmann, and E. Soergel, "Influence of the inhomogeneous field at the tip on quantitative piezoresponse force microscopy," *Appl. Phys. A Mater. Sci. Process.*, vol. 86, no. 3, pp. 353–355, 2007.

[141] A. Gruverman, "PFM Tutorial Lecture: Principles And Applications of Piezoresponse Force Microscopy," *2013 Joint UFFC, EFTF and PFM*

Symposium. Prague, 2013.

[142] L. Keeney, P. F. Zhang, C. Groh, M. E. Pemble, and R. W. Whatmore, "Piezoresponse force microscopy investigations of Aurivillius phase thin films," *J. Appl. Phys.* , vol. 108, no. 4, p. 42004, 2010.

[143] R. Proksch and S. Kalinin, "Piezoresponse Force Microscopy with Asylum Research AFMs," 2015. [Online]. Available: https://www.asylumresearch.com/Applications/PFMAppNote/PFMApp Note.shtml.

[144] K. E. Drexler, *Nanosystems: Molecular Machinery, Manufacturing, and Computation.* New York: John Wiley & Sons, 1992.

[145] J. B. Goodenough and K.-S. Park, "The Li-Ion Rechargeable Battery: A Perspective," *J. Am. Chem. Soc.* , vol. 135, no. 4, pp. 1167–1176, 2013.

[146] A. K. Geim and K. S. Novoselov, "The rise of graphene," *Nat Mater*, vol. 6, no. 3, pp. 183–191, 2007.

[147] W. B. Amos and J. G. White, "How the Confocal Laser Scanning Microscope entered Biological Research," *Biol. Cell,* vol. 95, no. 6, pp. 335–342, 2003.

[148] C. E. Sanborn and S. A. Myers, "Precision Tem Sample Preparation Using Focused Ion Beam Marking Strategies," *MRS Online Proc. Libr.*, vol. 254, 1991.

[149] P. Poddar, T. Fried, G. Markovich, A. Sharoni, D. Katz, T. Wizansky, and O. Millo, "Manifestation of the Verwey transition in the tunneling spectra of magnetite nanocrystals," *EPL (Europhysics Lett.*, vol. 64, no. 1, p. 98, 2003.

[150] *CRC Handbook of Chemistry and Physics.* CRC Press, 2004.

[151] L. Bouet, P. Tailhades, and A. Rousset, "Relations between magneto-optical properties and reactivity in cobalt-manganese ferrite thin films and powders," *J. Magn. Magn. Mater.* , vol. 153, no. 3, pp. 389–396, 1996.

[152] E. V. Ramana, A. Mahajan, M. P. F. Graça, A. Srinivas, and M. A. Valente, "Ferroelectric and magnetic properties of magnetoelectric

$(Na_{0.5}Bi_{0.5})TiO_3$-$BiFeO_3$ synthesized by acetic acid assisted sol–gel method," *J. Eur. Ceram. Soc.*, vol. 34, no. 16, pp. 4201–4211, 2014.

[153] L. Néel, "Superantiferromagnetism in small particles," *Acad. Sci.*, vol. 252, 1961.

[154] A. K. Singh, *Advanced X-ray Techniques in Research And Industries*. Amsterdam: IOS Press, 2005.

[155] B. D. Gaulin, "Magnetic Neutron Scattering," 2011.

[156] A. L. Patterson, "The scherrer formula for X-ray particle size determination," *Phys. Rev.*, vol. 56, no. 10, pp. 978–982, 1939.

[157] G. Balaji, R. A. Narayanan, A. Weber, F. Mohammad, and C. S. S. R. Kumar, "Giant magnetostriction in magnetite nanoparticles," *Mater. Sci. Eng. B*, vol. 177, no. 1, pp. 14–18, 2012.

[158] J. Narayan and A. Tiwari, "Novel methods of forming self-assembled nanostructured materials: Ni nanodots in Alumina and Titania matrices.," *J. Nanosci. Nanotech.*, vol. 4, p. 726, 2004.

9 Publications

1. **L. F. Henrichs**, J. Bennett, A. J. Bell, "Choice of tip, signal stability and practical aspects of Piezoresponse-Force-Microscopy", *Rev. Sci. Instrum.,* vol. 86, p. 083707, 2015; http://dx.doi.org/10.1063/1.4929572

2. P. Mandal, A. Manjón-Sanz, A. J. Corkett, T. P. Comyn, K. Dawson, T. Stevenson, J. Bennett, **L. F. Henrichs**, A. J. Bell, E. T. Nishibori, M. Takata, M. Zanella, M. R. Dolgos, U. Adem, X. Wan, M. J. Pitcher, S. Romani, T. T. Tran, P. S. Halasyamani, J. B. Claridge and M. J. Rosseinsky, "Morphotropic Phase Boundary in the Pb-Free $(1-x)BiTi_{3/8}Fe_{2/8}Mg_{3/8}O_3-xCaTiO_3$ System: Tetragonal Polarization and Enhanced Electromechanical Properties.", *Adv. Mater.*, vol. 27, pp. 2883–2889, 2015; http://dx.doi.org/10.1002/adma.201405452

3. **L. F. Henrichs**, L. Chen, A. J. Bell, "Simple technique for high-throughput marking of distinguishable micro-areas for microscopy", *J. Microsc.*, 2015, http://dx.doi.org/10.1111/jmi.12337

Under review:

4. **L. F. Henrichs**, O. Cespedes, J. Bennett, J. Landers, S. Salamon, C. Heuser, T. Helbig, O. Gutfleisch, D. C. Lupascu, H. Wende, W. Kleemann, and A. J. Bell, "Multiferroic clusters: a new perspective for relaxor-type room-temperature multiferroics", *Adv. Funct. Mater.*, 2015